UiO : University of Oslo

Eleonora Piersanti

Parameter-robust formulation and preconditioning of poroelasticity equations for brain modelling

Thesis submitted for the degree of Philosophiae Doctor

Department of Mathematics
Faculty of Mathematics and Natural Sciences

University of Oslo
Simula Research Laboratory

2023

Series of dissertations submitted to the
Faculty of Mathematics and Natural Sciences, University of Oslo
No. 2594

ISSN 1501-7710

Print production: Graphics Center, University of Oslo.

To my sisters

Acknowledgments

When I first moved to Oslo to start my PhD, I had many hopes and thoughts on how things should have evolved. Many things did not go as I had hoped, and many greatly exceeded my expectations. Looking back at all these years, I feel deep gratitude towards the great people I had the luck to meet.

First, I thank my supervisors, Marie E. Rognes and Kent-Andre Mardal. Marie, I am grateful for everything you taught me, for your guidance, rigour, knowledge, patience, kindness, and support. Kent, thanks for showing me how to be serious without taking yourself too seriously and for your knowledge, patience and support.

I am grateful to the Norwegian Ministry of Research and Education for funding the SUURPh programme and my PhD. The SUURPh programme gave me incredible opportunities that I was not always capable of exploiting, even if I always tried my best. I want to thank everyone involved in the programme, Andy Edwards, Rachel Thomas, Elin Backe Christophersen and Kimberly McCabe, for their unwavering help and support during these years. I want to thank the other PhD students in the SUURPh programme Viviane Timmermann, Alessio Buccino, Aslak Bergersen, Karl Erik Holter, Solveig Næss, Jonas van den Brink, Karoline Horgmo Jæger, Liubov Nikitushkina, and Tristan Stöber. It was wonderful being part of this group. I am also thankful to Karl Erik and Solveig for their friendship and for finding the time to proofread the introduction of this thesis.

I want to express my gratitude to my coauthors Jeonghun J. Lee, Travis B. Thompson, and Vegard Vinje, for their support and essential contribution to this thesis.

I want to thank Magne A. Nordaas, Miroslav Kuchta, and Jørgen S. Dokken for, among other things, helping me several times with technical issues.

I am grateful to Simula and the colleagues I met there, particularly Ilse (Ilsbeth) G. M. van Herck, with whom I shared many weekends working towards finishing our PhDs. I also thank Gabriel Balaban for his support over the years.

Finally, I am grateful to my parents, Alessandro and Luigina, and my sisters, Annalisa and Alessandra. Thank you for everything you have done for me and for supporting me, even if this means being far from each other.

Eleonora Piersanti
Oslo, January 2023

List of Papers

Paper I

J. J. Lee, E. Piersanti, K.-A. Mardal, M. E. Rognes. “A mixed finite element method for nearly incompressible multiple-network poroelasticity”. In: *SIAM Journal on Scientific Computing.* Vol. 41, no. 2 (2019), DOI: 10.1137/18M1182395.

Paper II

E. Piersanti, M. E. Rognes, K.-A. Mardal. “Parameter robust preconditioning for multi-compartmental Darcy equations”. In: *Numerical Mathematics and Advanced Applications ENUMATH 2019* Vol. 139, (August 2020).

Paper III

E. Piersanti, J. J. Lee, T. Thompson, K.-A. Mardal. “Parameter robust preconditioning by congruence for multiple-network poroelasticity”. In: *SIAM Journal on Scientific Computing.* Vol. 43, no. 4 (2021), DOI: 10.1137/20M1326751.

Paper IV

E. Piersanti, M. E. Rognes, V. Vinje. “Are brain displacements and pressures within the parenchyma induced by surface pressure differences? A computational modelling study”. Submitted to bioRχiv DOI: 10.1101/2022.09.07.506967, to be submitted to a peer-reviewed journal.

Contents

List of Figures

List of Tables

Chapter 1

Introduction

Mathematical modelling of brain parenchyma mechanics and fluid dynamics is a powerful tool to better understand clearance mechanisms, and investigate mechanistic hypotheses that cannot be verified with *in vivo* experiments. Single and multiple network poroelasticity theory (MPET) can be used to model the behaviour of different types of porous media: ceramic, soils and rocks, and biological tissues such as bones and brain parenchyma(Fig. 1.1). In addition, MPET has been used in the past decade to understand better how the different fluid compartments exchange mass in the brain and, more generally, the brain's clearance process. Nonetheless, the MPET equations applied to brain modelling present several numerical and modelling challenges. Therefore, in the articles collected in this thesis, an analysis of the system of equations from a numerical and computational viewpoint using both theoretical proofs and practical numerical experiments is presented. In addition, brain parenchyma pulsatility is modelled via linear elasticity and single network poroelasticity equations in a realistic human brain domain.

1.1 Objectives

This thesis aims to provide the reader with analytical and practical tools that can facilitate the application of the MPET equations to brain modelling and show how brain modelling can be utilised to verify hypotheses that could not be realized *in vivo*. Moreover, we aim to:

- Derive a robust formulation for the MPET equations. The range of material parameters in the MPET equations calls for a robust formulation with respect to parameter variation (Paper I).
- Efficiently solve the MPET equations. Robust and efficient solvers are necessary to apply the equations to realistic and involved applications (Papers II-III).
- Investigate the effect of pulsatile pressure gradient on the parenchyma with linear elasticity and poroelasticity equations (Paper IV).

1.2 Main findings

The main findings can be summarized as follows

- In Paper I, the total pressure formulation for the MPET equation is introduced. Numerical experiments in support of the novel formulation

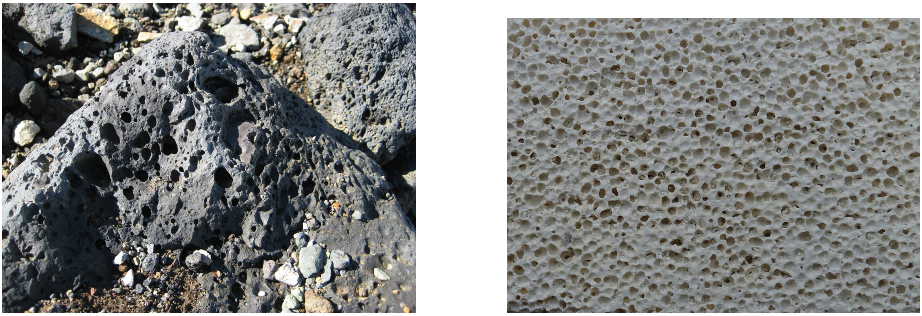

(a) Lavatic rock

(b) Pumice rock

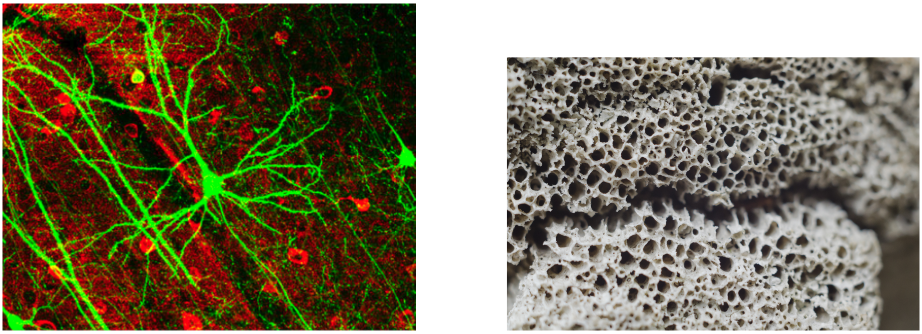

(c) Neurons in mouse cerebral cortex

(d) Bone

Figure 1.1: Some examples of porous materials that can be modelled using poroelasticity theory ((a)-(b) Stock images with Pixabay license,(c) from [Lee+06] via Wikimedia Commons, (d) photo by Jakub Fryś via Wikimedia Commons).

robustness are presented. The parameter robustness of the formulation is demonstrated.

- In Papers II and III, we present strategies to precondition the robust formulation of the multiple–compartmental Darcy (MPT) and MPET equations. We utilise the concept of diagonalization by congruence, showing how to practically construct a parameter-robust block-diagonal preconditioner.
- In Paper IV, we show that the pulsatile pressure gradient applied on the parenchyma surface does not travel inside the parenchyma despite producing a pulsatile displacement field.

1.3 Central nervous system anatomy

The central nervous system consists of the brain and the spinal cord. The human brain consists of the cerebrum, brainstem, and cerebellum. The brain and the

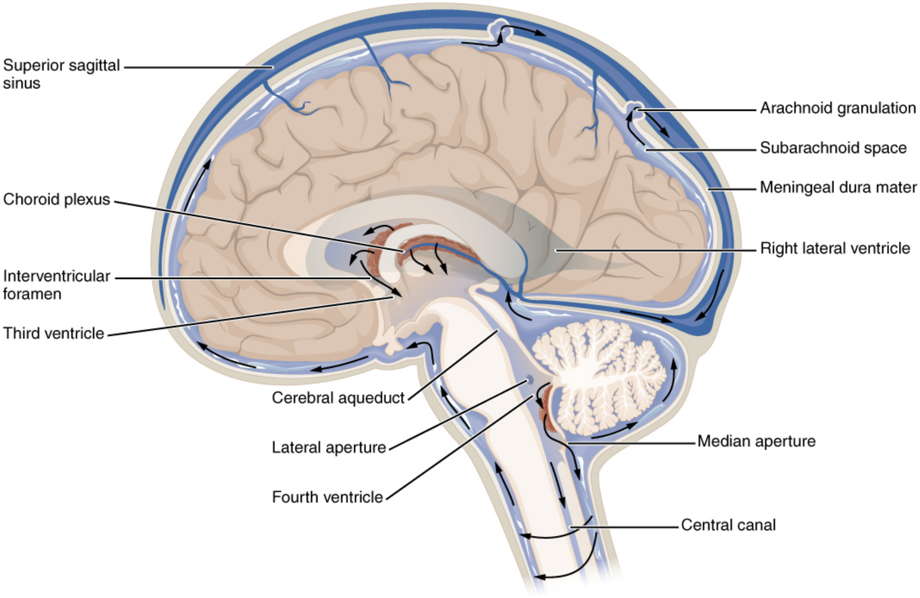

Figure 1.2: The cerebrospinal fluid circulates in the subarachnoid space around the brain and spinal cord and the brain's ventricles (The Textbook OpenStax Anatomy and Physiology Published May 18, 2016, via Wikimedia Commons).

spinal cord are covered by three membranes called meninges: the dura mater, the arachnoid mater, and the pia mater. Between the arachnoid mater and the pia mater are the subarachnoid space (SAS) and subarachnoid cisterns, which contain the cerebrospinal fluid (CSF).

The brain parenchyma is a very soft tissue consisting of white and grey matter. In particular, the brain's outer layer is constituted by grey matter, mostly made of unmyelinated axons and cell bodies. The brain core is composed of white matter composed mainly of myelinated axons of nerve fibres. The brain parenchyma floats in the CSF and is enclosed in the skull, which can be considered a rigid container.

Within the brain parenchyma, we find the ventricles. The ventricles are a system of communicating cavities constituted by two lateral ventricles, the third ventricle, the cerebral aqueduct, and the fourth ventricle. In the ventricles, we find the choroid plexus that secretes the CSF that circulates from the lateral ventricles through the paired interventricular foramina (of Monro) to the third ventricle and then via the aqueduct to the fourth ventricle(Fig. 1.2). The CSF serves a protective function towards the brain: the brain tissue is in neutral buoyancy condition, and it is protected from mechanical injuries as the CSF acts as a shock absorber [Moo06]. In addition, the CSF regulates the brain homeostasis processes, wastes clearance, and intracranial pressure regulation.

The brain parenchyma is also permeated by a network of blood vessels that ensure that the high demand for oxygen and glucose in the brain is satisfied. In particular, the cerebral vasculature comprises the arterial, capillary and venous systems [Cip09]. At the bottom of the brain, we find the circle of Willis, where the internal carotid arteries anteriorly and vertebral arteries posteriorly are joint. Over the pial surface, we find a network of leptomeningeal arteries from which arterioles branch out and dive into the cortex[AC21]. In the parenchyma, we find a vast network of capillaries with a higher density in the grey matter than in the white matter [Kle+86] The venous system contains the dural sinuses and cerebral superficial and deep veins. The superficial veins drain the cortical surfaces, and the deep veins drain the deep white and grey matter.[KA08]

1.4 Intracranial pressure and brain pulsatility

The blood is pumped by the heart at a frequency of ca. 1Hz, and every change in cerebral blood flow is transmitted to the other brain fluids and the tissues. In particular, according to the Monro-Kellie hypothesis [Mok01], an increase in blood volume in the brain corresponds to a rise in intracranial pressure (ICP) and a movement of CSF [Bal14].

The intracranial pressure can be decomposed into a mean stationary component and a pulsatile component. According to Marmarou [MSL75], a hypothetical and reasonable approximation of the relationship between the intracranial volume and pressure is represented by an exponential curve. Marmarou's hypothesis suggests that at a higher mean ICP, a small volume change of the brain, for example, caused by blood inflow, corresponds to a significant increase in the pulsatile ICP. In other words, according to this theory, the brain is more compliant at lower mean ICP, and the ICP pulsations are smaller, where compliance is defined as the ratio between volume change and pressure change. Therefore, the increase in mean ICP makes the system stiffer and more sensitive to small volume perturbations.

Nevertheless, increased mean ICP is not the only factor affecting the ICP profile and brain compliance. For example, patients with intracranial normal pressure hydrocephalus (iNPH) have higher ICP pulsations while having normal values of mean ICP [EK11]. The obstruction of venous and CSF pathways can also affect the compliance of the brain and the profile of ICP pulsations. In Eide et al. [ER16], patients with symptomatic pineal cysts present increased pulsatile pressure while having normal mean ICP.

ICP has been extensively investigated in the last decades, and several techniques have been developed to measure it [EE20; WEM11]. Moreover, the invasive measurements of ICP are only available for patients and not for healthy subjects for obvious ethical reasons. For example, Eide and colleagues showed in their works, i.e. [ES10b; ES16], how ICP pulsatility can be used as an indicator of the successful outcome of shunt surgery for iNPH patients.

Another quantity of interest that has been investigated and debated in the last decades is the transmantle pressure gradient between the ventricles and the SAS. According to numerical simulations from Linninger et al. [Lin+07], a small transmantle pressure gradient is present both in healthy subjects ($\sim$ 10Pa) and iNPH patients ($\sim$ 30 Pa). In a cohort of 10 iNPH patients with ventriculomegaly, Eide et al. [ES10a] did not find evidence of a pulsatile transmantle ICP gradient. Nevertheless, Eide measured an uneven spatial distribution of ICP pulsatility in hydrocephalus patients [Eid08]. In a more recent work by Vinje et al. [Vin+19], a pulsatile ICP gradient was found between ventricles and SAS from the analysis of measurements in iNPH patients. This pulsatile gradient was decomposed into two sinusoidal functions with periods (T) corresponding to cardiac ($T = 1$s) and respiratory ($T = 4$s) cycles.

Despite the scientific community's interest in ICP measurements and monitoring, the interpretation and understanding of ICP signals are still under development due to their complexity [CC20]. In this context, mathematical modelling represents a valuable resource.

In Paper IV, a pulsatile transmantle pressure gradient is applied between the ventricles and SAS, and the brain parenchyma is modelled with linear elasticity and poroelasticity equations.

1.5 Applications of multiple–network poroelasticity theory equations

The linear poroelasticity equations have been used to model a great variety of phenomena in different fields. In 1941, Biot [Bio41] presented the single-network poroelasticity theory together with two simple tests: the standard soil test and its version for clay soil. The standard soil test considers a two-dimensional column of soil laterally confined, so the lateral expansion is constrained under a constant vertical load.

Though it is possible to model some important geological phenomena using a single–network poroelastic model, it is often necessary to increase the complexity of the model; for example, in the case of fissured or fractured soils, where the porosity is not homogeneous and different permeabilities and compressibilities are present. Therefore, in these cases, a multiple–network model better captures reality. In [BZK60a], a two–network model is investigated to study the infiltration phenomenon in fissured rocks. Fissured rocks are constituted of blocks of permeable rocks separated by a system of fissures. This configuration presents some modelling challenges. The blocks of permeable rock have different sizes that highly depend on the development of the fissure system. In addition, the pores' width is considerably smaller compared to the fissures' width, but at the same time, pores occupy a much larger volume than fissures.

In [BER93] different combinations of multiple–porosity/multiple–permeability equations are introduced. A single–permeability/single–porosity model (Biot's equations) is used to model a non-fractured reservoir with uniform permeability and porosity. For more complicated configurations of the reservoir, it is possible to use various combinations of the multiple–network poroelasticity equations among which, for example, a triple–porosity/dual–permeability or a triple–porosity/triple–permeability model for severely fractured reservoirs.

Ultimately, we can extend this reasoning about reservoir to the multiporosity/-multipermeability model described in (1.8.1).

Another field where poroelasticity and multiple–network poroelasticity equations find application is biology, particularly in tissue modelling. In biological tissues, we usually have a solid phase consisting of macromolecules such as collagen, fibrin, elastin, and cells and a fluid phase such as water, interstitial fluid or blood. Hence, the poroelastic theory can be used to study the behaviour of biological tissues as a homogenized material. In particular, it is possible to get significant insights into the key quantities and parameters that characterize fundamental aspects of the tissue.

Poroelasticity has been used to model, for example, bone tissue [Cow99], arterial endothelium[Buk+15], and the intervertebral disc[Mal+15]. Poroelasticity equations can be extended to model specific phenomena such as tissue hydration and swelling [TJZ09], tissue growth [Roo+03]–[CC12]. Over the last twenty years, the poroelasticity and multiple–network poroelastic theory have been used to model brain parenchyma and its interaction with different fluids in the brain.

1.6 Single and multiple–network poroelasticity equations in the brain

Several interconnected processes over different time and space scales happen in the brain every moment, making the brain an extremely challenging organ to model. As reported in Goriely et al. 2015 review [Gor+15], reliable and successful brain modelling requires a tremendous multidisciplinary effort to provide a comprehensive understanding of brain physiology and pathophysiology. Poroelasticity is one of the many possible models used to gain insight into brain mechanisms and pathologies.

Single-network poroelasticity equations have been widely applied to brain modelling to understand different pathologies that affect the central nervous system. In her PhD thesis[Stø14], Støverud modelled the spinal cord as a porous medium in the context of syringomyelia. Syringomyelia is a neurological condition characterized by fluid-filled cavities (syrinxes) within the spinal cord tissue that may grow over time. In her work, Støverud utilizes Biot's equations in conjunction with Navier–Stokes equations to investigate the role of pressure gradient, velocity gradient, geometry, and material parameters on the formation of syrinxes and CSF velocity and pressure profile. Smillie et al. model hydrocephalus on a simplified spherical brain geometry [SSM05] with a one–network poroelastic model. Wirth et al. [WS09] modelled the infusion test in a simplified spherical brain geometry, including the arterial blood and CSF compartments. In Eisentrager's PhD thesis [Eis12], the constant rate infusion test is modelled with a single-network poroelastic model, and results are compared against clinical data.

A four-network model can be used in the brain, where the fluid networks represent interstitial fluid, capillary, venous, and arterial blood. The four–network MPET model has been widely used to investigate fluid transport between the different fluid networks and brain parenchyma, in addition to modelling various pathologies and exploring mechanistic hypotheses. In [TV10]–[TV11], the four–network model is utilized to model normal pressure hydrocephalus with a simplified spherical brain geometry. In [Var+16], the model is applied to a two-dimensional mesh derived from an MRI slice. In [Guo+18], the model is applied to a realistic, patient-specific parenchyma mesh, and blood pressure measurements are used to impose the boundary conditions on the arterial compartment. Finally, Guo and colleagues [Guo+19] proposed partial validation of the MPET equation in the brain by comparison of the blood perfusion results from the computational model with medical measurements and images.

Nevertheless, a four–network MPET model allows for a better description of the brain physiology but presents several challenges, among which are the increased computational cost compared to a single–network model and the identification of the many model parameters.

1.7 Theory of poroelasticity equations for an isotropic solid

The linear poroelastic equations, or Biot's equations, were first introduced by Biot in 1941 in his paper titled 'General Theory of Three-Dimensional Consolidation'[Bio41]. In this section, we will present some of the passages to derive the Biot's equations.

The assumptions under this model are isotropy of the material, small deformations, and linearity of the stress-strain relationship. Given the solid displacement field u, the strain tensor is defined as

$$\varepsilon = \frac{1}{2}(\nabla u + \nabla u^T),$$

and $\operatorname{tr}(\epsilon) = \operatorname{div} u$ we can write the constitutive relation between the solid's stress tensor components σ_{ij} and the solid's strain tensor components ϵ_{ij} as

$$\varepsilon_{ij} = \frac{1}{2\mu}\sigma_{ij} - \frac{\nu}{E}\delta_{ij}\sigma_{kk} + \frac{1}{3H}p$$

where μ, ν, and E are elastic parameters. In particular, μ is a Lamé constant, ν is the Poisson coefficient, and E is Young's modulus. It is important to notice that only two of these parameters are independent. For example, Young's modulus is related to ν, and μ as

$$E = 2\mu(1 + \nu).$$

The water content θ can be expressed as a function of the solid stresses and fluid pressure as

$$\theta = \frac{1}{3H}(\sigma_{11} + \sigma_{22} + \sigma_{33}) + \frac{1}{R}p,$$

where the constant $\frac{1}{H}$ represents the compressibility of the soil and $\frac{1}{R}$ measures the change in water content for a given change in the fluid pressure.

Alternatively, it is possible to express the solid stresses as a function of the solid's strains and fluid pressure as

$$\sigma_{ij} = \lambda\delta_{ij}\varepsilon_{kk} + 2\mu\varepsilon_{ij} - \alpha\delta_{ij}p,$$

where

$$\alpha = \frac{2(1+\nu)G}{3(1-2\nu)H},$$

where G is the shear modulus and α the Biot coefficient. Likewise, we can express the variation in fluid content θ as follows

$$\theta = \alpha \operatorname{div} u + \frac{p}{Q}, \tag{1.7.1}$$

with

$$\frac{1}{Q} = \frac{1}{R} - \frac{\alpha}{H}$$

Once we have established the constitutive equations that describe the relationship between the solid stress and strain, fluid pressure and fluid content, it is possible to write the equilibrium equation

$$-\operatorname{div}\sigma = f.$$

To complete the set of equations, we will introduce Darcy's law where the fluid's flux V is related to the fluid's pressure gradient as follows

$$V = -K\,\nabla p, \tag{1.7.2}$$

where $K = \frac{\kappa_f}{\nu_f}$, κ_f and ν_f are the permeability and fluid viscosity, respectively. Assuming the fluid is incompressible, the variation of fluid content in time can be expressed as

$$\dot{\theta} = -\operatorname{div} V \tag{1.7.3}$$

Now, combining equations (1.7.1)-(1.7.2)-(1.7.3) we obtain

$$K\Delta p = \alpha \operatorname{div}\dot{u} + \frac{1}{Q}\dot{p}. \tag{1.7.4}$$

Therefore the system of equations constituting Biot's equations are

$$\begin{aligned} -\operatorname{div}(2\mu\varepsilon(u) + \lambda \operatorname{div} u\mathbb{I}) + \alpha\,\nabla p &= f, && \text{(1.7.5a)}\\ s\dot{p} + \alpha \operatorname{div}\dot{u} - K\Delta p &= g, && \text{(1.7.5b)} \end{aligned}$$

with $s = \frac{1}{Q}$ as the storage coefficient.

1.8 Extension of consolidation theory for a solid permeated by multiple networks

In the previous section, we have derived the equations for a linear elastic medium permeated by a single fluid network. The multiple–network equations are an extension of Biot's system.

In [BZK60b], the model is extended to a case for a medium with pores and fissures. Therefore, two porosities values are considered. In [BER93], Biot's system is extended to a two and three–network system. We can generalize the equations further and consider a solid permeated by J networks. The quasi-static MPET equations read for a given number of networks $J \in \mathbb{N}$, find the displacement u and the network pressures p_j for $j = 1, \dots, J$ such that

$$- \operatorname{div}(2\mu\varepsilon(u) + \lambda \operatorname{div} u\mathbb{I}) + \textstyle\sum_j \alpha_j \nabla p_j = f, \tag{1.8.1a}$$

$$s_j \dot{p}_j + \alpha_j \operatorname{div} \dot{u} - \operatorname{div} K_j \nabla p_j + \textstyle\sum_i \xi_{j\leftarrow i}(p_j - p_i) = g_j, \tag{1.8.1b}$$

where $u = u(x,t)$ and $p_j = p_j(x,t)$ for $x \in \Omega \subset \mathbb{R}^d$ $(d = 1,2,3)$ and for $t \in (0,T]$.

The isotropic assumption for the solid matrix still stands. In addition, the transfer between different networks is regulated by the pressure difference between different networks modulated by the transfer coefficients $\xi_{j\leftarrow i}$. As with the Biot's equations, for each network j, we define the Biot-Willis coefficient $\alpha_j \in (0,1]$ such that $\sum_j \alpha_j \leq 1$, the storage coefficient $s_j > 0$, and the hydraulic conductivity tensor K_j. Moreover, ∇ denotes the column-wise gradient, ε is the symmetric gradient, div denotes the (row-wise) divergence, the superposed dot denotes the time derivative(s), and $\mathbb{I}$ denotes the identity matrix. On the right-hand side, f represents body forces and g_j sources (or sinks) in network j for $j = 1, \dots, J$.

1.9 A note on multiple–compartmental Darcy equations

This thesis also analyses the multiple–compartmental Darcy equations from a numerical viewpoint. In this introduction and the papers included in this thesis, we will also refer to these equations as MPT equations.

The MPT equations describe a rigid solid permeated by several fluid networks, where the interaction between the elastic deformation and the fluid is neglected. Due to the linearity of the MPET equations, the multi-compartmental Darcy equations represent an excellent auxiliary tool to study the fluid-only part of the equations and obtain insights into the complete MPET system. The multiple–compartmental Darcy equations read as follows: for a given number of networks $J \in \mathbb{N}$, find the network pressures p_j for $j = 1, \dots, J$ such that

$$- \operatorname{div} K_j \nabla p_j + \sum_{i=1}^{J} \xi_{j\leftarrow i}(p_j - p_i) = g_j \quad \text{in } \Omega, \tag{1.9.1}$$

where $p_j = p_j(x)$ for $x \in \Omega \subset \mathbb{R}^d$ $(d = 1, 2, 3)$, and Ω is the physical domain. The scalar parameter $K_j > 0$ represents the permeability of each network j. The parameter $\xi_{j \leftarrow i} \geq 0$ is the exchange coefficient into network j from network i.

The MPT equations have been used to model different biological tissues. In [Mic+13] and [Lee+15] cardiac perfusion is modelled using the MPT equations. Three networks are considered: the arterial, capillary and venous. In [BLR18], MPT equations are used to model perfusion in the liver and in [Józ+19], a brain circulation model is derived from the multiple–compartmental Darcy equations.

1.10 Robust formulation for poroelasticity equations

The numerical stability of the MPET equations and the accuracy of the simulated results strongly depend on the accuracy of the material parameters.

The MPET system (1.8.1) is constituted of one vector equation (momentum equation) and J scalar equations (continuity equations), one for each fluid network. The size of the linear system that needs to be solved and the number of the material parameters that need to be estimated/measured increases with the number of networks J.

In the MPET equations, we can distinguish between the elastic parameters and the fluid network's parameters. Estimating these parameters can be very complicated, especially in biological applications where measurements are not always possible or available. The value of a parameter can vary even by orders of magnitude from different studies, even for the same application(Table 1.1).

One way to choose the correct (or most correct) parameters can be, for example, a systematic numerical study. To experiment with very different parameter values, we need parameter–robust numerical formulations and efficient and fast solvers. The numerical approximation/discretization of parameter-dependent equations presents several challenges, especially when the parameters approach their limit values.

In this regard, we consider the phenomenon of locking. Locking is a numerical phenomenon that occurs when the finite element discretization is inadequate, and the computed displacements are considerably smaller than they should be. From a numerical analysis viewpoint, the ratio between the continuity and coercivity constant tends to infinity. By Céa's lemma, we can expect errors larger than the approximation error. In particular, the convergence of the solution is sub-optimal. An overview of the locking problem can be found in [Bra07] (Ch. VI), and a more detailed analysis can be found in [Arn81; BS92; SBS95].

Let us consider the issue of locking [PW09] in the single-network poroelasticity equations. For a numerical scheme approximating the linear poroelasticity equations, locking occurs when the Poisson's ratio ν approaches the value 0.5, or equivalently when $\lambda \to \infty$, and the accuracy of the solution deteriorates.

To illustrate the poor performance of a standard mixed finite element discretization of the Biot equations (1.7.5) in the nearly incompressible case, we consider a variant of the smooth test case presented by [Yi17, Section 7.1] and by [LMW17].

Parameter	Unit	Value	Reference
Hydraulic conductivities (K_j)	mm^2 (kPa s)$^{-1}$		
Brain gray matter		2.0×10^{-3}	[Stø+16]
Brain white matter		2.0×10^{-2}	[Stø+16]
Cardiac arteries		1.0	[Mic+13]
Cardiac capillaries		2.0	[Mic+13]
Cardiac veins		10.0	[Mic+13]
Brain vasculature		3.75×10^{1}	[Var+16]
Brain fluid exchange		1.57×10^{-2}	[Var+16]
Exchange coefficients ($\xi_{j\to i}$)	(kPa s)$^{-1}$		
Brain capillary-vasculature		1.5×10^{-16}	[Var+16]
Brain capillary-tissue fluid		2.0×10^{-16}	[Var+16]
Brain tissue fluid-veins		2.0×10^{-10}	[Var+16]
Cardiac capillary-arteries		2.0×10^{-2}	[Mic+13]
Cardiac capillary-veins		5.0×10^{-2}	[Mic+13]

Table 1.1: Sample values for hydraulic conductivities and exchange coefficients found in the literature.

Let $\Omega = [0,1]^2 \subset \mathbb{R}^2$, take $T = 0.5$, and consider the Biot equations (1.7.5) with $c = 1.0$, $K = 1.0$, $\alpha = 1.0$. Moreover, we let $E = 1.0$ and $\nu = 0.49999$ for

$$\mu = \frac{E}{2(1+\nu)} \approx \frac{1}{3}, \quad \lambda = \frac{\nu E}{(1-2\nu)(1+\nu)} \approx 16\,666.$$

To discretize (1.7.5), we consider a Crank-Nicolson discretization in time and a standard mixed finite element discretization in space in this example. More precisely, we approximate the displacement u using continuous piecewise quadratic vector fields (and denote the approximation by u_h) and the fluid pressures p using continuous piecewise linear (lowest order Taylor-Hood[TH73] elements) defined relative to a uniform mesh of Ω of mesh size h. As exact solutions, we let

$$u((x_0,x_1),t) = t\begin{pmatrix} (\sin(2\pi x_1)(-1+\cos(2\pi x_0)) + \frac{1}{\mu+\lambda}\sin(\pi x_0)\sin(\pi x_1)) \\ (\sin(2\pi x_0)(1-\cos(2\pi x_1)) + \frac{1}{\mu+\lambda}\sin(\pi x_0)\sin(\pi x_1)) \end{pmatrix},$$

and

$$p((x_0,x_1,t)) = -t\sin(\pi x_0)\sin(\pi x_1).$$

The resulting approximation errors for $u(T)$ in the $L^2(\Omega)$ and $H^1(\Omega)$ norms are listed in Table 1.2 for a series of meshes generated by nested uniform refinements, together with the corresponding rates of convergence. We observe that the convergence rates are one order sub-optimal for this choice of spatial discretization.

h	$\|u(T) - u_h(T)\|$	Rate	$\|u(T) - u_h(T)\|_{H^1}$	Rate
H	0.169		2.07	
$H/2$	0.040	2.09	0.980	1.08
$H/4$	0.010	2.04	0.480	1.03
$H/8$	0.002	2.03	0.235	1.03
$H/16$	0.0006	2.09	0.110	1.10
$H/32$	0.0001	2.28	0.045	1.30
Optimal		3		2

Table 1.2: Standard (two-field) Biot formulation. Approximation errors in the L^2 ($\|\cdot\|$)- and H^1 ($\|\cdot\|_{H^1}$)-norms and associated convergence rates for a standard mixed finite element discretization for a smooth manufactured solution test case for a nearly incompressible material. H corresponds to a uniform mesh constructed by dividing the unit square into 4×4 squares and dividing each square by a diagonal.

Let us consider the total pressure formulation as in [Lee+19; LMW17] for the Biot consolidation model. We introduce a new scalar variable p_0 such as $p_0 = -\lambda \operatorname{div} u + \alpha p$ and the equations read as follows:

$$-\operatorname{div}(2\mu\epsilon(u)) + \alpha \nabla p_0 = f, \tag{1.10.1a}$$

$$-\operatorname{div} u - \lambda^{-1}(p_0 - \alpha p) = 0 \tag{1.10.1b}$$

$$s\dot{p} - K\Delta p + \lambda^{-1}\alpha(\dot{p}_0 - \alpha\dot{p}) = g. \tag{1.10.1c}$$

We can repeat the numerical experiment with the total pressure formulation (1.10.1) and we can observe that the convergence rate is restored Tab.1.3

In the literature, we can find other types of robust formulations for the single-network poroelasticity equations in addition to the three-field total pressure formulation. For example, a three-field formulation with solid displacement, fluid pressure, and fluid flux (Darcy velocity) as variables is presented in [HK17; Hon+20]. In [Kum+20], the solvability and stability of a four-field formulation, with solid displacement, fluid pressure, fluid flux, and total pressure as variables, are analysed. A stabilised three-field flux formulation is presented in [Rod+17]. Two different stable discretizations of the three-field flux formulation of Biot's equations are presented in [Gas+18]. The fluid flux is a quantity of interest, especially in biomedical applications, and a three-field flux formulation has the advantage to return a more accurate estimation of the Darcy velocity. In [Józ+21] the authors present a systematic study comparing different finite element discretizations to analytical solutions in order to estimate cerebral perfusion.

Similarly to the single-network poroelasticity equations, we can introduce the total pressure formulation of the quasi-static MPET equations as follows:

h	$\|u(T) - u_h(T)\|$	Rate	$\|u(T) - u_h(T)\|_{H^1}$	Rate
H	3.2×10^{-2}		7.3×10^{-1}	
$H/2$	3.7×10^{-3}	3.12	2.0×10^{-1}	1.88
$H/4$	$4.4 \times 10{-}4$	3.08	5.1×10^{-2}	1.96
$H/8$	5.3×10^{-5}	3.03	1.3×10^{-2}	1.99
$H/16$	6.7×10^{-6}	3.01	3.2×10^{-3}	2.00
$H/32$	8.3×10^{-7}	3.0	8.0×10^{-4}	2.00
Optimal		3		2

Table 1.3: Total pressure formulation for Biot's equations. Approximation errors in the L^2 ($\|\cdot\|$)- and H^1 ($\|\cdot\|_{H^1}$)-norms and associated convergence rates for a standard mixed finite element discretization for a smooth manufactured solution test case for a nearly incompressible material.

for $t \in (0, T]$, find the displacement vector field u and the pressure scalar fields p_i for $i = 0, \ldots, A$ such that

$$\operatorname{div} u - \lambda^{-1}\alpha \cdot p = 0, \tag{1.10.2a}$$

$$-\operatorname{div}(2\mu\varepsilon(u) + p_0 I) = f, \tag{1.10.2b}$$

$$c_j \dot{p}_j + \alpha_j \lambda^{-1}\alpha \cdot \dot{p} - \operatorname{div}(K_j \nabla p_j) + S_j = g_j \quad j = 1, \ldots, A. \tag{1.10.2c}$$

In Paper I of this thesis, we analyse the total pressure formulation Eq.(1.10.2) for the MPET equation for a nearly incompressible material.

1.11 Iterative solvers and preconditioners

For realistic application, it is necessary to discretize the equations and solve the linear system derived from the chosen discretization method. An overview of iterative methods for linear systems can be found in [Gre97].

Let us consider a general matrix equation that yields from the finite element discretization of a set of partial differential equations (PDEs)

$$Ax = b.$$

The matrix A is a sparse matrix (one of the many good properties of the finite element method) of order N and Z non–zero entries. To solve the system we can use different approaches. We could use a direct method, such as the Gaussian elimination algorithm, with a computational cost of $\mathcal{O}(ZN \log N)$ or an iterative method with a cost of $\mathcal{O}(N)$ per iteration. Nonetheless, for complicated problems, with many degrees of freedom, the use of a direct solver becomes impractical and we have to resort to iterative solvers.

Krylov subspace methods are a family of iterative methods where the iterates are in a k-th order subspace V_k defined as

$$V_k = V_k(A, b) = \text{span}(b, Ab, A^2b, A^{k-1}b).$$

If A is a symmetric positive definite (SPD) matrix, then the solution x minimizes the quadratic function

$$E(x) = \frac{1}{2}x^TAx - x^Tb,$$

and the error $\|x - x_k\|$ for the iterate x_k satisfies the orthogonality property

$$(A(x - x_k), y) = 0, \quad \forall y \in V_k$$

With the SPD assumption for A, we could use the conjugate gradient (CG) method. Starting from an initial guess x_0, the CG method computes the next iterative solution following the residual $r_k = (b - Ax_k)$ conjugate direction. Because of the construction of the Krylov space, the method only needs the previous iterate to compute the new iterate. For the Conjugate Gradient (CG) method, we can define the upper bound for the error [LT04] as

$$\|x - x_k\|_A \leq \left(\frac{\sqrt{\kappa(A)} - 1}{\sqrt{\kappa(A)} + 1}\right)^k \|x - x_0\|_A,$$

where $\|x\|_A = x^TAx$, and the condition number κ for a SPD matrix is defined as

$$\kappa(A) = \frac{\max(|\lambda_i|)}{\min(|\lambda_i|)}, \text{for } i = 1, \ldots, N$$

If the matrix A is symmetric indefinite then we cannot use the minimization of the quadratic function (1.11), and instead the iterate x_k will satisfy the following

$$x_k := \underset{y \in V_k}{\text{argmin}} \|(Ay - b)\|,$$

from which we can derive the method of minimal residual (MinRes)[PS75]. Also for this algorithm, the upper bound of the convergence ratio of the residual (for an SPD matrix) [LT04] depends on the condition number of the matrix A such as

$$\|A(x - x_k)\| \leq 2\left(\frac{\kappa(A) - 1}{\kappa(A) + 1}\right)^{k/2} \|Ax - x_0\|.$$

In the case of indefinite nonsymmetric matrices we can use other methods, for example the generalized minimal residual method (GMRES).

1.12 Parameter–robust preconditioning for MPET equations

In this thesis, we address the construction of robust preconditioners for the MPET (1.10.2) and MPT (1.9.1) equations. In particular, we consider the subclass of preconditioners called block diagonal preconditioners.

We have shown in the previous section, with some practical estimates, that the convergence of an iterative method depends on the condition number of the operator A. We can improve the condition number, and therefore the convergence of the iterative method, with preconditioning. We hereby summarize some of the key aspects of preconditioning as in [MW11].

Let X be a separable, real Hilbert space with inner product $\langle \cdot, \cdot \rangle_X$, norm $\|\cdot\|_X$ and dual space X^*. Let $\mathcal{A} : X \to X$ be an invertible, symmetric isomorphism on X such that $\mathcal{A} \in \mathcal{L}(X, X^*)$ where $\mathcal{L}(X, X^*)$ is the set of bounded linear operators mapping X to its dual. Given $f \in X^*$ consider the problem of finding $x \in X$ such that

$$\mathcal{A}x = f. \tag{1.12.1}$$

The preconditioned problem reads as follows

$$\mathcal{B}\mathcal{A}x = \mathcal{B}f, \tag{1.12.2}$$

where $\mathcal{B} \in \mathcal{L}(X^*, X)$ is a symmetric isomorphism defining the preconditioner. The convergence rate of a Krylov space method for this problem can be bounded in terms of the condition number $\kappa(\mathcal{B}\mathcal{A})$ where

$$\kappa(\mathcal{B}\mathcal{A}) = \|\mathcal{B}\mathcal{A}\|_{\mathcal{L}(X,X)} \|(\mathcal{B}\mathcal{A})^{-1}\|_{\mathcal{L}(X,X)}.$$

Here, the operator norm $\|\mathcal{A}\|_{\mathcal{L}(X,X^*)}$ is defined by

$$\|\mathcal{A}\|_{\mathcal{L}(X,X^*)} = \sup_{x \in X} \frac{\|\mathcal{A}x\|_{X^*}}{\|x\|_X}. \tag{1.12.3}$$

For a parameter, or more generally, a set of parameters ε we can consider the parameter-dependent operator $\mathcal{A}_\varepsilon$ and its preconditioner $\mathcal{B}_\varepsilon$. Assume that we can choose appropriate spaces X_ε and X_ε^* such that the norms

$$\|\mathcal{A}_\varepsilon\|_{\mathcal{L}(X_\varepsilon, X_\varepsilon^*)} \text{ and } \|\mathcal{A}_\varepsilon^{-1}\|_{\mathcal{L}(X_\varepsilon^*, X_\varepsilon)}$$

are bounded independently of ε. Similarly, we assume that we can find a preconditioner $\mathcal{B}_\varepsilon$ such that the norms $\|\mathcal{B}_\varepsilon\|_{\mathcal{L}(X_\varepsilon, X_\varepsilon^*)}$ and $\|\mathcal{B}_\varepsilon^{-1}\|_{\mathcal{L}(X_\varepsilon^*, X_\varepsilon)}$ are bounded independently of ε. Given these assumptions, the condition number $\kappa(\mathcal{B}_\varepsilon\mathcal{A}_\varepsilon)$ will be bounded independently of ε. We refer to such preconditioners as robust with respect to ε or parameter-robust preconditioners. In biomechanics, parameters span multiple orders of magnitude, meaning that even a mild dependence of $\kappa(\mathcal{B}_\epsilon\mathcal{A}_\epsilon)$ on ϵ will have a large effect on the time complexity of the chosen numerical method to solve the equations.

The MPET system can be viewed as a saddle point and falls in the saddle point theory framework [Bre74]. Saddle point problems are notoriously challenging to precondition, and the various numerical parameters involved in the MPET equations make the construction of a robust preconditioner very complex.

In work by Haga et al. [HOL11], several block preconditioners for standard the two-field (displacement, fluid pressure) formulation of Biot's equations are compared. In particular, the study focuses on the cases of highly discontinuous permeability and significant jumps in elastic properties.

In [ABB12], various approaches to constructing preconditioners for the three-field flux formulation of Biot's equations are presented and compared.

In more recent work by Hong and colleagues [Hon+19], a robust preconditioner for the flux formulation based on [HK17] is presented for single and multiple-network poroelasticity. In this work, the authors introduce novel parameter-dependent norms and demonstrate stability with respect to all the parameters. Again, for the MPET equations, Hong and colleagues [Hon+20] propose a new class of fully decoupled iterative Uzawa-type methods. This method fully decouples the displacement, fluid velocity, and pressures. Therefore, it allows for solving considerably smaller subsystems at each iteration compared to fixed-stress iterative schemes. In [Adl+19], robust preconditioners are presented for a stabilized discretization of the three-field flux formulation of Biot's equations. Both block diagonal and block triangular preconditioners are considered, and the numerical analysis is supported by numerical examples.

In the work by Chen and colleagues [Che+20], block-diagonal preconditioners are presented both for the two-field formulation (displacement and pressure) and the three-field flux formulation. The analysis is corroborated by numerical tests on a two-dimensional square domain.

In this thesis (Paper I) we considered the total pressure formulation for the MPET equations, expanding the work of Lee and colleagues [LMW15], and we implemented a change of variables via congruence in order to make the system easier to precondition.

1.13 Change of variables using diagonalization by congruence

The MPET and MPT systems of equations undergo a change of variable through a transformation by congruence to make them more suitable for block–diagonal preconditioning. The MPT and MPET equations have non–diagonal terms due to the exchange terms $\xi_{i \leftarrow j}$ that establish coupling between different fluid networks. Depending on the value of the parameters, the extra–diagonal terms can be dominant.

In this thesis, we show how a change of variables that diagonalizes the system facilitates the construction of a block–diagonal preconditioner. The procedure that we have used and the relative theory are explained more in detail in [HJ12] and described in the Appendix of Paper III. Here we report some of the steps for the MPT equations. The system (1.9.1) can be expressed in operator form as

$$\mathcal{A}_{\mathrm{MPT}} p = g \quad \text{with} \quad \mathcal{A}_{\mathrm{MPT}} = -K\Delta + E, \tag{1.13.1}$$

where

$$K = \begin{pmatrix} K_1 & 0 & \cdots & 0 \\ 0 & K_2 & \cdots & 0 \\ \vdots & \vdots & \ddots & \vdots \\ 0 & 0 & \cdots & K_J \end{pmatrix}, \quad E = \begin{pmatrix} \xi_1 & -\xi_{1\leftarrow 2} & \cdots & -\xi_{1\leftarrow J} \\ -\xi_{1\leftarrow 2} & \xi_2 & \cdots & -\xi_{2\leftarrow J} \\ \vdots & \vdots & \ddots & \vdots \\ -\xi_{1\leftarrow J} & -\xi_{2\leftarrow J} & \cdots & \xi_J \end{pmatrix}. \tag{1.13.2}$$

We note that K is real, positive definite and diagonal (and thus invertible), and that E is real, symmetric and (weakly row) diagonally dominant by definition. Therefore, K and E are diagonalizable by congruence if and only if $C = K^{-1}E$ is diagonalizable. C is similar to a real symmetric matrix and therefore diagonalizable.

Let $P \in \mathbb{R}^{J\times J}$ be an invertible linear transformation defining a change of variables and let $\tilde{p}$ be the new set of variables such that

$$p = P\tilde{p}. \tag{1.13.3}$$

We aim to find a transformation P that simultaneously diagonalizes K and E by congruence. The matrix P is constructed from the eigenvectors of C. We refer the reader to Paper III in this thesis, where we show how to compute the matrix mentioned above P and handle exceptions. Substituting (1.13.3) in (1.13.1) and multiplying by P^T we can obtain a new formulation for the MPT equations that read as follows: find the transformed pressures $\tilde{p} = (\tilde{p}_1, \dots, \tilde{p}_J)$ such that

$$\tilde{\mathcal{A}}_{\mathrm{MPT}}\tilde{p} = (-\tilde{K}\Delta + \tilde{E})\tilde{p} = P^T g, \tag{1.13.4}$$

where $\tilde{K} = P^T K P$ and $\tilde{E} = P^T E P$ are diagonal with

$$\tilde{K} = \mathrm{diag}(\tilde{K}_1, \dots, \tilde{K}_J), \quad \tilde{E} = \mathrm{diag}(\tilde{\xi}_1, \dots, \tilde{\xi}_J). \tag{1.13.5}$$

It is straightforward to build a block–diagonal preconditioner that is spectrally equivalent to $\tilde{A}_{MPT}$.

1.14 Summary of Papers

Paper I: A mixed finite element method for nearly incompressible multiple–network poroelasticity

This paper presents and analyses a new mixed finite element formulation of a general family of quasi-static multiple-network poroelasticity (MPET) equations. In particular, we focus on the nearly incompressible case for which standard mixed finite element discretizations of the MPET equations perform poorly.

Instead, we propose a new mixed finite element formulation based on introducing an additional total pressure variable. By presenting energy estimates for the continuous solutions and a priori error estimates for a family of compatible semi-discretizations, we show that this formulation is robust in the limits of incompressibility, vanishing storage coefficients, and vanishing transfer between networks.

Numerical experiments corroborate these theoretical results. Our primary interest in the MPET equations stems from the use of these equations in modelling interactions between biological fluids and tissues in physiological settings. So, we additionally present physiologically realistic numerical results for blood and tissue fluid flow interactions in the human brain.

Paper II: **Parameter robust preconditioning for multi-compartmental Darcy equations** In this paper, we propose a new finite element solution approach to the multi-compartmental Darcy (MPT) equations describing flow and interactions in a porous medium with multiple fluid compartments. We introduce a new numerical formulation and a block-diagonal preconditioner based on variable transformation by congruence. In Section 2, we show the lack of parameter robustness for the standard formulation theoretically and via a numerical example. In Section 3, we describe the change of variable transformation that yields a robust formulation. In Section 4, the theoretical results are corroborated by numerical examples for a two–network and a three–network MPT system.

Paper III: **Parameter robust preconditioning by congruence for multiple–network poroelasticity**

The efficient numerical solution of the MPET equations is challenging, in part due to the complexity of the system and in part due to the presence of interacting parameter regimes. This paper presents a new strategy for efficiently and robustly solving the MPET equations numerically. In particular, we introduce a new approach to formulating finite element methods and associated preconditioners for the MPET equations.

The approach is based on designing transformations of variables that simultaneously diagonalize (by congruence) the equations' key operators and subsequently construct parameter-robust block-diagonal preconditioners for the transformed system.

After introducing the equations and the preconditioning framework, we show how to obtain the transformation matrix. We start considering a simplified version of the MPET equations, the MPT (or multiple–compartmental Darcy) equations and show the process to find the transformation matrix for a three–network system.

For the MPET equations, we demonstrate that the new formulation obtained via variable transformation is suitable for constructing a parameter-robust preconditioner. The theoretical results in Sections 4.2–4.3 are supported by numerical examples for a 2–dimensional domain. In addition, results for a modified version of the classical footing problem for a cubic mesh are presented.

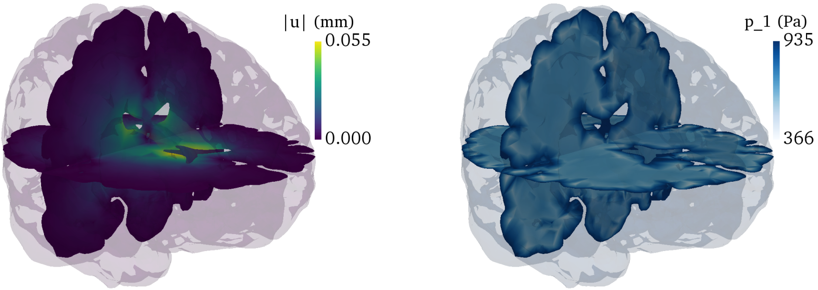

(a) Displacement magnitude $|u(\bar{t})|$ (b) Extracellular pressure $p_1(\bar{t})$

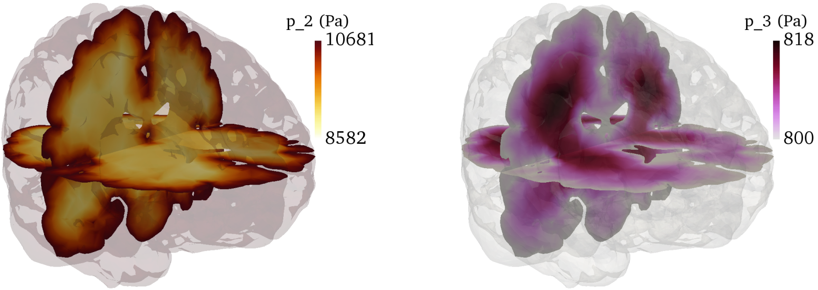

(c) Arterial pressure $p_2(\bar{t})$ (d) Venous pressure $p_3(\bar{t})$

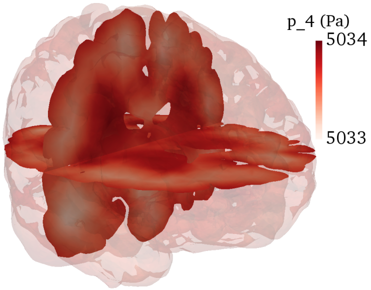

(e) Capillary pressure $p_4(\bar{t})$

Figure 1.3: Results of a four–network MPET simulation on a realistic brain mesh at $\bar{t} = 2.25$ s (Paper I). From left to right and top to bottom: (a) displacement magnitude $|u|$, (b) extracellular pressure p_1, (c) arterial blood pressure p_2, (d) venous blood pressure p_3 and (e) capillary blood pressure p_4.

Paper IV: Are brain displacements and pressures within the parenchyma induced by surface pressure differences? A computational modelling study

ICP and brain pulsatility have been studied widely in the past and are fundamental quantities both from a diagnostic and a monitoring viewpoint. Nevertheless, many aspects of ICP are unclear. In this study, we aim to contribute to the understanding of the mechanisms that generate pulsatility in the brain.

In this study, we apply a pulsatile pressure gradient derived from ICP measurements in 10 iNPH patients between the ventricular and pial surfaces. In particular, we model the brain parenchyma as either a linearly elastic or a single-network poroelastic medium. With these models, we can compute the effect of the pulsatile pressure gradient on parenchyma displacement, volume change, fluid pressure, and fluid flux. The resulting displacement field is pulsatile and in qualitatively and quantitatively agreement with the literature, both with elastic and poroelastic models. However, the pulsatile forces on the boundaries are insufficient for pressure pulse propagation through brain parenchyma. Our results suggest that pressure differences originating over the brain surface via, e.g. pial artery pulsatility are insufficient to drive interstitial fluid (ISF) flow within the brain parenchyma.

1.15 Limitations and future work

Limitations and future work for this thesis are presented in the single papers. Here we offer a summary.

This thesis presents a parameter-robust formulation for the multiple-network poroelasticity equations and parameter-robust preconditioners for the MPET and MPT equations. Nevertheless, these tools have not been applied to realistic case scenarios. The results presented in Papers I, II, and III are based on simple domains. They lay a foundation for future computations with more complicated, ideally patient-specific, geometries and a wide range of parameter values and applications.

In Paper IV, we investigated the effect of a pulsatile pressure gradient in a realistic brain parenchyma domain. The study was limited to linear elasticity, single-network poroelasticity models, and a limited set of parameters. A natural extension of this work consists in considering a multiple-network poroelasticity model and a broader set of parameters with the aid of the numerical tools developed in the other papers. In addition, the applied pressure gradient was derived from measurements in iNPH patients, and the results cannot be generalized to healthy subjects. ICP and pulsatility are crucial in understanding brain physiology, and further investigation of pressure pulse propagation within the brain parenchyma is needed.

Bibliography

[ABB12] Axelsson, O., Blaheta, R., and Byczanski, P. “Stable discretization of poroelasticity problems and efficient preconditioners for arising saddle point type matrices”. In: *Computing and Visualization in Science* vol. 15, no. 4 (2012), pp. 191–207.

[AC21] Agarwal, N. and Carare, R. O. “Cerebral vessels: an overview of anatomy, physiology, and role in the drainage of fluids and solutes”. In: *Frontiers in Neurology* (2021), p. 1748.

[Adl+19] Adler, J. H. et al. “Robust preconditioners for a new stabilized discretization of the poroelastic equations”. In: (May 2019).

[Arn81] Arnold, D. N. “Discretization by finite elements of a model parameter dependent problem”. In: *Numerische Mathematik* vol. 37, no. 3 (1981), pp. 405–421.

[Bal14] Balédent, O. “Imaging of the cerebrospinal fluid circulation”. In: *Adult Hydrocephalus*. Ed. by Rigamonti, D. Cambridge University Press, 2014.

[BER93] Bai, M., Elsworth, D., and Roegiers, J.-C. “Multiporosity/multipermeability approach to the simulation of naturally fractured reservoirs”. In: *Water Resources Research* vol. 29, no. 6 (1993), pp. 1621–1633.

[Bio41] Biot, M. A. “General theory of three-dimensional consolidation”. In: *Journal of Applied Physics* vol. 12, no. 2 (1941), pp. 155–164.

[BLR18] Brašnová, J., Lukeš, V., and Rohan, E. “Identification of multicompartment darcy flow model material parameters”. In: (2018).

[Bra07] Braess, D. *Finite Elements: Theory, Fast Solvers, and Applications in Solid Mechanics*. Third. Cambridge University Press, 2007.

[Bre74] Brezzi, F. “On the existence, uniqueness and approximation of saddle-point problems arising from Lagrangian multipliers”. In: *Publications mathématiques et informatique de Rennes*, no. S4 (1974), pp. 1–26.

[BS92] Babuška, I. and Suri, M. “Locking effects in the finite element approximation of elasticity problems”. In: *Numerische Mathematik* vol. 62, no. 1 (1992), pp. 439–463.

[Buk+15] Bukac, M. et al. “Effects of poroelasticity on fluid-structure interaction in arteries: A computational sensitivity study”. In: *Modeling the heart and the circulatory system*. Springer, 2015, pp. 197–220.

[BZK60a] Barenblatt, G. I., Zheltov, I. P., and Kochina, I. “Basic concepts in the theory of seepage of homogeneous liquids in fissured rocks [strata]”. In: *Journal of applied mathematics and mechanics* vol. 24, no. 5 (1960), pp. 1286–1303.

[BZK60b] Barenblatt, G. I., Zheltov, I. P., and Kochina, I. “Basic concepts in the theory of seepage of homogeneous liquids in fissured rocks [strata]”. In: *Journal of applied mathematics and mechanics* vol. 24, no. 5 (1960), pp. 1286–1303.

[CC12] Cowin, S. C. and Cardoso, L. “Mixture theory-based poroelasticity as a model of interstitial tissue growth”. In: *Mechanics of materials* vol. 44 (2012), pp. 47–57.

[CC20] Czosnyka, M. and Czosnyka, Z. “Origin of intracranial pressure pulse waveform”. In: *Acta Neurochirurgica* vol. 162, no. 8 (2020), pp. 1815–1817.

[Che+20] Chen, S. et al. “Robust block preconditioners for poroelasticity”. In: (Jan. 2020).

[Cip09] Cipolla, M. J. “The cerebral circulation”. In: *Integrated systems physiology: From molecule to function* vol. 1, no. 1 (2009), pp. 1–59.

[Cow99] Cowin, S. C. “Bone poroelasticity”. In: *Journal of biomechanics* vol. 32, no. 3 (1999), pp. 217–238.

[EE20] Evensen, K. B. and Eide, P. K. “Measuring intracranial pressure by invasive, less invasive or non-invasive means: limitations and avenues for improvement”. In: *Fluids and Barriers of the CNS* vol. 17, no. 1 (2020), pp. 1–33.

[Eid08] Eide, P. K. “Demonstration of uneven distribution of intracranial pulsatility in hydrocephalus patients”. In: *Journal of neurosurgery* vol. 109, no. 5 (2008), pp. 912–917.

[Eis12] Eisenträger, A. “Finite element simulation of a poroelastic model of the CSF system in the human brain during an infusion test”. PhD thesis. Oxford University, UK, 2012.

[EK11] Eide, P. K. and Kerty, E. “Static and pulsatile intracranial pressure in idiopathic intracranial hypertension”. In: *Clinical neurology and neurosurgery* vol. 113, no. 2 (2011), pp. 123–128.

[ER16] Eide, P. K. and Ringstad, G. “Increased pulsatile intracranial pressure in patients with symptomatic pineal cysts and magnetic resonance imaging biomarkers indicative of central venous hypertension”. In: *Journal of the Neurological Sciences* vol. 367 (2016), pp. 247–255.

[ES10a] Eide, P. K. and Sæhle, T. “Is ventriculomegaly in idiopathic normal pressure hydrocephalus associated with a transmantle gradient in pulsatile intracranial pressure?” In: *Acta neurochirurgica* vol. 152, no. 6 (2010), pp. 989–995.

[ES10b] Eide, P. K. and Sorteberg, W. “Diagnostic intracranial pressure monitoring and surgical management in idiopathic normal pressure hydrocephalus: a 6-year review of 214 patients”. In: *Neurosurgery* vol. 66, no. 1 (2010), pp. 80–91.

[ES16] Eide, P. K. and Sorteberg, W. “Outcome of surgery for idiopathic normal pressure hydrocephalus: role of preoperative static and pulsatile intracranial pressure”. In: *World neurosurgery* vol. 86 (2016), pp. 186–193.

[Gas+18] Gaspar, F. J. et al. “New stabilized discretizations for poroelasticity equations”. In: *International Conference on Numerical Methods and Applications*. Springer. 2018, pp. 3–14.

[Gor+15] Goriely, A. et al. “Mechanics of the brain: perspectives, challenges, and opportunities”. In: *Biomechanics and modeling in mechanobiology* vol. 14, no. 5 (2015), pp. 931–965.

[Gre97] Greenbaum, A. *Iterative methods for solving linear systems*. SIAM, 1997.

[Guo+18] Guo, L. et al. “Subject-specific multi-poroelastic model for exploring the risk factors associated with the early stages of Alzheimer’s disease”. In: *Interface Focus* vol. 8, no. 1 (2018), p. 20170019.

[Guo+19] Guo, L. et al. “On the validation of a multiple-network poroelastic model using arterial spin labeling MRI data”. In: *Frontiers in computational neuroscience* vol. 13 (2019), p. 60.

[HJ12] Horn, R. A. and Johnson, C. R. *Matrix analysis*. Cambridge university press, 2012.

[HK17] Hong, Q. and Kraus, J. “Parameter-robust stability of classical three-field formulation of Biot’s consolidation model”. In: (June 2017).

[HOL11] Haga, J. B., Osnes, H., and Langtangen, H. P. “Efficient block preconditioners for the coupled equations of pressure and deformation in highly discontinuous media”. In: *International Journal for Numerical and Analytical Methods in Geomechanics* vol. 35, no. 13 (2011), pp. 1466–1482.

[Hon+19] Hong, Q. et al. “Conservative discretizations and parameter-robust preconditioners for Biot and multiple-network flux-based poroelasticity models”. In: *Numerical Linear Algebra with Applications* vol. 26, no. 4 (2019), e2242.

[Hon+20] Hong, Q. et al. “Parameter-robust Uzawa-type iterative methods for double saddle point problems arising in Biot’s consolidation and multiple-network poroelasticity models”. In: *Math. Models. Methods. Appl. Sci.* vol. 30, no. 13 (2020), pp. 2523–2555.

[Józ+19] Józsa, T. et al. “A cerebral circulation model for in silico clinical trials of ischaemic stroke”. In: (2019). CompBioMed Conference 2019, pp. 25–27.

[Józ+21] Józsa, T. I. et al. “On the sensitivity analysis of porous finite element models for cerebral perfusion estimation”. In: *Annals of Biomedical Engineering* vol. 49, no. 12 (2021), pp. 3647–3665.

[KA08] Kılıç, T. and Akakın, A. “Anatomy of cerebral veins and sinuses”. In: *Handbook on cerebral venous thrombosis* vol. 23 (2008), pp. 4–15.

[Kle+86] Klein, B. et al. “Interdependency of local capillary density, blood flow, and metabolism in rat brains”. In: *American Journal of Physiology-Heart and Circulatory Physiology* vol. 251, no. 6 (1986), H1333–H1340.

[Kum+20] Kumar, S. et al. “Conservative discontinuous finite volume and mixed schemes for a new four-field formulation in poroelasticity”. In: *ESAIM: Mathematical Modelling and Numerical Analysis* vol. 54 (1 Jan. 2020), pp. 273–299.

[Lee+06] Lee, W.-C. A. et al. “Dynamic remodeling of dendritic arbors in GABAergic interneurons of adult visual cortex”. In: *PLoS biology* vol. 4, no. 2 (2006), e29.

[Lee+15] Lee, J. et al. “Multiscale modelling of cardiac perfusion”. In: *Modeling the heart and the circulatory system*. Springer, 2015, pp. 51–96.

[Lee+19] Lee, J. J. et al. “A mixed finite element method for nearly incompressible multiple-network poroelasticity”. In: *SIAM Journal on Scientific Computing* vol. 41, no. 2 (2019), A722–A747.

[Lin+07] Linninger, A. A. et al. “Cerebrospinal fluid flow in the normal and hydrocephalic human brain”. In: *IEEE Transactions on Biomedical Engineering* vol. 54, no. 2 (2007), pp. 291–302.

[LMW15] Lee, J. J., Mardal, K.-A., and Winther, R. “Parameter-robust discretization and preconditioning of Biot’s consolidation model”. In: (July 2015).

[LMW17] Lee, J. J., Mardal, K.-A., and Winther, R. “Parameter-robust discretization and preconditioning of Biot’s consolidation model”. In: *SIAM Journal on Scientific Computing* vol. 39, no. 1 (2017), A1–A24.

[LT04] Liesen, J. and Tich, P. “Convergence analysis of Krylov subspace methods”. In: *GAMM-Mitteilungen* vol. 27, no. 2 (2004), pp. 153–173.

[Mal+15] Malandrino, A. et al. “Poroelastic modeling of the intervertebral disc: A path toward integrated studies of tissue biophysics and organ degeneration”. In: *MRS Bulletin* vol. 40, no. 4 (2015), pp. 324–332.

[Mic+13] Michler, C. et al. “A computationally efficient framework for the simulation of cardiac perfusion using a multi-compartment Darcy porous-media flow model”. In: *Int. J. Numer. Method Biomed. Eng.* vol. 29, no. 2 (2013), pp. 217–232.

[Mok01] Mokri, B. “The Monro–Kellie hypothesis: applications in CSF volume depletion”. In: *Neurology* vol. 56, no. 12 (2001), pp. 1746–1748.

[Moo06] Moody, D. M. “The blood-brain barrier and blood-cerebral spinal fluid barrier”. In: *Seminars in cardiothoracic and vascular anesthesia*. Vol. 10. 2. SAGE Publications Sage CA: Thousand Oaks, CA. 2006, pp. 128–131.

[MSL75] Marmarou, A., Shulman, K., and Lamorgese, J. “Compartmental analysis of compliance and outflow resistance of the cerebrospinal fluid system”. In: *Journal of neurosurgery* vol. 43, no. 5 (1975), pp. 523–534.

[MW11] Mardal, K.-A. and Winther, R. “Preconditioning discretizations of systems of partial differential equations”. In: *Numerical Linear Algebra with Applications* vol. 18, no. 1 (2011), pp. 1–40.

[PS75] Paige, C. C. and Saunders, M. A. “Solution of sparse indefinite systems of linear equations”. In: *SIAM journal on numerical analysis* vol. 12, no. 4 (1975), pp. 617–629.

[PW09] Phillips, P. J. and Wheeler, M. F. “Overcoming the problem of locking in linear elasticity and poroelasticity: an heuristic approach”. In: *Computational Geosciences* vol. 13, no. 1 (2009), pp. 5–12.

[Rod+17] Rodrigo, C. et al. “New stabilized discretizations for poroelasticity and the Stokes’ equations”. In: (June 2017).

[Roo+03] Roose, T. et al. “Solid stress generated by spheroid growth estimated using a linear poroelasticity model”. In: *Microvascular research* vol. 66, no. 3 (2003), pp. 204–212.

[SBS95] Suri, M., Babuška, I., and Schwab, C. “Locking effects in the finite element approximation of plate models”. In: *Mathematics of computation* vol. 64, no. 210 (1995), pp. 461–482.

[SSM05] Smillie, A., Sobey, I., and Molnar, Z. “A hydroelastic model of hydrocephalus”. In: *Journal of Fluid Mechanics* vol. 539 (2005), pp. 417–443.

[Stø+16] Støverud, K. H. et al. “Poro-elastic modeling of Syringomyelia–a systematic study of the effects of pia mater, central canal, median fissure, white and gray matter on pressure wave propagation and fluid movement within the cervical spinal cord”. In: *Computer Methods in Biomechanics and Biomedical Engineering* vol. 19, no. 6 (2016), pp. 686–698.

[Stø14] Støverud, K.-H. “Relation between the Chiari I malformation and syringomyelia from a mechanical perspective”. In: (2014).

[TH73] Taylor, C. and Hood, P. “A numerical solution of the Navier-Stokes equations using the finite element technique”. In: *Comput. Fluids* vol. 1, no. 1 (1973), pp. 73–100.

[TJZ09] Tao, C., Jiang, J. J., and Zhang, Y. “A fluid-saturated poroelastic model of the vocal folds with hydrated tissue”. In: *Journal of biomechanics* vol. 42, no. 6 (2009), pp. 774–780.

[TV10] Tully, B. and Ventikos, Y. “Modelling Normal Pressure Hydrocephalus as a ‘Two-Hit’Disease Using Multiple-Network Poroelastic Theory”. In: *Summer Bioengineering Conference*. Vol. 44038. American Society of Mechanical Engineers. 2010, pp. 877–878.

[TV11] Tully, B. and Ventikos, Y. “Cerebral water transport using multiple-network poroelastic theory: application to normal pressure hydrocephalus”. In: *Journal of Fluid Mechanics* vol. 667 (2011), p. 188.

[Var+16] Vardakis, J. C. et al. “Investigating cerebral oedema using poroelasticity”. In: *Med. Eng. Phys.* vol. 38, no. 1 (2016), pp. 48–57.

[Vin+19] Vinje, V. et al. “Respiratory influence on cerebrospinal fluid flow–a computational study based on long-term intracranial pressure measurements”. In: *Scientific reports* vol. 9, no. 1 (2019), pp. 1–13.

[WEM11] Wagshul, M. E., Eide, P. K., and Madsen, J. R. “The pulsating brain: a review of experimental and clinical studies of intracranial pulsatility”. In: *Fluids and Barriers of the CNS* vol. 8, no. 1 (2011), p. 5.

[WS09] Wirth, B. and Sobey, I. “Analytic solution during an infusion test of the linear unsteady poroelastic equations in a spherically symmetric model of the brain”. In: *Mathematical medicine and biology: a journal of the IMA* vol. 26, no. 1 (2009), pp. 25–61.

[Yi17] Yi, S.-Y. “A study of two modes of locking in poroelasticity”. In: *SIAM Journal on Numerical Analysis* vol. 55, no. 4 (2017), pp. 1915–1936.

Papers

Paper I

A mixed finite element method for nearly incompressible multiple-network poroelasticity

J. J. Lee, E. Piersanti, K.-A. Mardal, M. E. Rognes

Published in *SIAM Journal on Scientific Computing*, March 2019, volume 41, issue 2, DOI: 10.1137/18M1182395.

Abstract

In this paper, we present and analyze a new mixed finite element formulation of a general family of quasi-static multiple-network poroelasticity (MPET) equations. The MPET equations describe flow and deformation in an elastic porous medium that is permeated by multiple fluid networks of differing characteristics. As such, the MPET equations represent a generalization of Biot's equations, and numerical discretizations of the MPET equations face similar challenges. Here, we focus on the nearly incompressible case for which standard mixed finite element discretizations of the MPET equations perform poorly. Instead, we propose a new mixed finite element formulation based on introducing an additional total pressure variable. By presenting energy estimates for the continuous solutions and *a priori* error estimates for a family of compatible semi-discretizations, we show that this formulation is robust in the limits of incompressibility, vanishing storage coefficients, and vanishing transfer between networks. These theoretical results are corroborated by numerical experiments. Our primary interest in the MPET equations stems from the use of these equations in modelling interactions between biological fluids and tissues in physiological settings. So, we additionally present physiologically realistic numerical results for blood and tissue fluid flow interactions in the human brain.

I.1 Introduction

In this paper, we consider a family of quasi-static multiple-network poroelasticity (MPET[1]) equations reading as follows: for a given number of networks $A \in \mathbb{N}$,

---

[1] The abbreviation MPET stems from the term multiple-network poroelastic theory as used by e.g. [TV11]. Here, we instead refer to the multiple-network poroelasticity equations but keep the abbreviation for the sake of convenience.

find the displacement u and the network pressures p_j for $j = 1, \ldots, A$ such that

$$- \operatorname{div} C\varepsilon(u) + \textstyle\sum_j \alpha_j \nabla p_j = f, \tag{I.1.1a}$$

$$c_j \dot{p}_j + \alpha_j \operatorname{div} \dot{u} - \operatorname{div} K_j \nabla p_j + S_j = g_j, \qquad 1 \leq j \leq A, \tag{I.1.1b}$$

where $u = u(x, t)$ and $p_j = p_j(x, t)$, $1 \leq j \leq A$ for $x \in \Omega \subset \mathbb{R}^d$ $(d = 1, 2, 3)$ and for $t \in [0, T]$.

In our context, (I.1.1) originates from balance of mass and momentum in a porous, linearly elastic medium permeated by A segregated viscous fluid networks. The operators and parameters are as follows: C is the elastic stiffness tensor, each network j is associated with a Biot-Willis coefficient $\alpha_j \in (0, 1]$, storage coefficient $c_j \geq 0$, and hydraulic conductivity tensor $K_j = \kappa_j/\mu_j > 0$ (where κ_j and μ_j represent the network permeability and the network fluid viscosity, respectively). In (I.1.1a), ∇ denotes the gradient, ε is the symmetric (row-wise) gradient, div denotes the row-wise divergence. In (I.1.1b), ∇ and div are the standard gradient and divergence operators, and the superposed dot denotes the time derivative. Further, f represents a body force and g_j represents sources in network j for $j = 1, \ldots, A$, while S_j represents transfer terms out of network j.

In this paper, we consider the case of an isotropic stiffness tensor for which

$$C\varepsilon(u) = 2\mu\varepsilon(u) + \lambda \operatorname{div} uI \tag{I.1.2}$$

where μ, λ are the standard non-negative Lamé parameters and I denotes the identity tensor. Moreover, we will consider the case where the transfer terms S_j, quantifying the transfer out of network j into the other fluid networks, are proportional to pressure differences between the networks. More precisely, we assume that S_j takes the form:

$$S_j = S_j(p_1, \ldots, p_A) = \textstyle\sum_{i=1}^{A} \xi_{j \leftarrow i}(p_j - p_i), \tag{I.1.3}$$

where $\xi_{j \leftarrow i}$ are non-negative transfer coefficients for $i, j = 1, \ldots, A$. We will also assume that these transfer coefficients are symmetric in the sense that $\xi_{j \leftarrow i} = \xi_{i \leftarrow j}$, and note that $\xi_{j \leftarrow j}$ is arbitrary.

The MPET equations have an abundance of both geophysical and biological applications. In the case $A = 1$, (I.1.1) reduces to the well-known quasi-static Biot equations. While the Biot equations have been studied extensively, see e.g. [Agu+08; Lee17; MTL96; OR16; PW07; Sho00; Yi17]; to the best of our knowledge, the general multiple-network poroelasticity equations have received much less attention, especially from the numerical perspective. The case $A = 2$ is known as the Barenblatt-Biot model, and we note that Showalter and Momken [SM02] present an existence analysis for this model, while Nordbotten and co-authors [Nor+10] present an *a posteriori* error analysis for an approximation of a static Barenblatt-Biot system.

Our interest in the multiple-network poroelasticity equations primarily stems from the use of these equations in modelling interactions between biological fluids and tissue in physiological settings. As one example, Tully and Ventikos [TV11] considers (I.1.1) with four different networks ($A = 4$) to model fluid flows, network pressures and elastic displacement in brain tissue. The fluid networks represent the arteries, the arterioles/capillaries, the veins and the interstitial fluid-filled extracellular space, each network with e.g. a different permeability κ_j and different transfer coefficients $\xi_{j \leftarrow i}$.

A particularly important motivation for the current work is the recently proposed theory of the glymphatic system which describes a new mechanism for waste clearance in the human brain [Abb+18; Ili+12; Jes+15]. This mechanism is proposed to take the form of a convective flow of water-like fluid through (a) spaces surrounding the cerebral vasculature (paravascular spaces) and (b) through the extracellular spaces, driven by a hydrostatic pressure gradient between the arterial and venous compartments. Compared to diffusion only, such a convective flow would lead to enhanced transport of solutes through the brain parenchyma and, in particular, contribute to clearance of metabolic waste products such as amyloid beta. The accumulation of amyloid beta frequently seen in patients with Alzheimer's disease is as such seen as a malfunction of the glymphatic system. In this context, the original system of [TV11] represents a macroscopic model of interaction between the different fluid networks in the brain.

Discretization of Biot's equations is known to be challenging, in particular because of so-called poroelastic locking. Poroelastic locking has two main characteristics: 1) underestimation of the solid deformation if the material is close to being incompressible and 2) nonphysical pressure oscillations, in particular in the areas close to jumps in the permeabilities or to the boundary. Several recent (and not so recent) studies, see e.g. [Ber+15; BRK17; Hu+17; PW07; Rod+17; Yi17], focus on a three-field formulation of Biot's model, involving the elastic displacement, fluid pressure and fluid velocity. Four-field formulations where also the elasticity equation is in mixed form, designed to provide robust numerical methods for nearly incompressible materials, have also been studied [KS05; Lee16; Yi14].

In biological tissues, any jumps in the permeability parameters are typically small in contrast to geophysical applications. The challenge in the biomedical applications is rather that the tissues in our body mostly consist of water and as such should be close to be incompressible (for short time-scales and normal physiological pressures). Therefore, it may be crucial for accurate modeling of the interaction of the different network pressures in (I.1.1) to allow for an elastic material that is almost incompressible and/or with (nearly) vanishing storage coefficients, i.e. for $1 \ll \lambda < +\infty$ and $0 < c_j \ll 1$ in (I.1.1). Standard two-field mixed finite element discretizations of the Biot model, approximating the displacement and the fluid pressure only using Stokes-stable elements, are well-known to perform poorly in the incompressible limit, see e.g. [Lee17] and references therein. Moreover, we can easily demonstrate a suboptimal convergence rate for the corresponding standard mixed finite element discretization of the MPET equations, see Example I.1.1 below. On the other hand, two-field approximations are computationally inexpensive compared to three-field approximations in the sense that only one unknown, the network pressure, is involved in each network.

Example I.1.1. To illustrate poor performance of a standard mixed finite element discretization of the MPET equations (I.1.1) in the nearly incompressible case, we consider a variant of the smooth test case presented by [Yi17, Section 7.1]. Let $\Omega = (0,1)^2 \subset \mathbb{R}^2$, take $T = 0.5$, and consider the quasi-static multiple-network poroelasticity equations (I.1.1) with $A = 2$, $c_j = 1.0$, $K_j = 1.0$, $\alpha_j = 1.0$, and $S_j = 0$ for $j = 1, 2$. Moreover, we let $E = 1.0$ and $\nu = 0.49999$ for

$$\mu = \frac{E}{2(1+\nu)} \approx \frac{1}{3}, \quad \lambda = \frac{\nu E}{(1-2\nu)(1+\nu)} \approx 16\,666.$$

To discretize (I.1.1), we consider a Crank-Nicolson discretization in time and a standard mixed finite element discretization in space in this example. More precisely, we approximate the displacement u using continuous piecewise quadratic vector fields (and denote the approximation by u_h) and the fluid pressures p_j for $j = 1, 2$ using continuous piecewise linears defined relative to a uniform mesh of Ω of mesh size h. As exact solutions, we let

$$u((x_0, x_1), t) = t \begin{pmatrix} (\sin(2\pi x_1)(-1 + \cos(2\pi x_0)) + \frac{1}{\mu+\lambda} \sin(\pi x_0)\sin(\pi x_1)) \\ (\sin(2\pi x_0)(1 - \cos(2\pi x_1)) + \frac{1}{\mu+\lambda} \sin(\pi x_0)\sin(\pi x_1)) \end{pmatrix},$$

and

$$p_j((x_0, x_1, t)) = -jt \sin(\pi x_0)\sin(\pi x_1).$$

The resulting approximation errors for $u(T)$ in the $L^2(\Omega)$ and $H^1(\Omega)$ norms are listed in Table I.1 for a series of meshes generated by nested uniform refinements, together with the corresponding rates of convergence. We observe that the convergence rates are one order sub-optimal for this choice of spatial discretization.

h	$\lVert u(T) - u_h(T) \rVert$	Rate	$\lVert u(T) - u_h(T) \rVert_{H^1}$	Rate
H	0.169		2.066	
$H/2$	0.040	2.09	0.980	1.08
$H/4$	0.010	2.04	0.480	1.03
$H/8$	0.002	2.03	0.235	1.03
$H/16$	0.001	2.09	0.110	1.10
Optimal		3		2

Table I.1: Approximation errors in the L^2 ($\lVert \cdot \rVert$)- and H^1 ($\lVert \cdot \rVert_{H^1}$)-norms and associated convergence rates for a standard mixed finite element discretization for a smooth manufactured solution test case for a nearly incompressible material (Example I.1.1). H corresponds to a uniform mesh constructed by dividing the unit square into 4×4 squares and dividing each square by a diagonal.

The primary objective of this paper is to propose and analyze a new variational formulation and a corresponding spatial discretization of the MPET equations that are robust with respect to a nearly incompressible poroelastic matrix; i.e. the implicit constants in the error estimates are uniformly bounded for arbitrarily large $\lambda > 0$. To this end, we introduce a formulation with one additional scalar field unknown. For the MPET equations (I.1.1) with potentially multiple networks, the additional computational cost is thus small. Instead of taking the "solid pressure" $\lambda \operatorname{div} u$ as a new unknown, we take the total pressure, which is defined as a weighted sum of the network pressures and the solid pressure, as the new unknown. Such a formulation has previously been shown to be advantageous in the context of parameter-robust preconditioners for the Biot model [LMW17]. Here, we focus on stability and error estimates of the total pressure formulation for the more general MPET equations. The construction of preconditioners for the MPET equations will be addressed in a forthcoming paper.

Our new theoretical results include an energy estimate for the continuous variational formulation that is robust in the relevant parameter limits, in particular, that is uniform in the Lamé parameter λ, storage coefficients c_j for $j = 1, \ldots, A$, and transfer coefficients $\xi_{j \leftarrow i}$ for $i, j = 1, \ldots, A$, and a robust *a priori* error estimate for a class of compatible semi-discretizations of the new formulation. These theoretical results are supported by numerical experiments. Finally, we also present new numerical MPET simulations modelling blood and tissue fluid interactions in a physiologically realistic human brain.

This paper is organized as follows. Section I.2 presents notation and general preliminaries. In Section I.3, we introduce a total-pressure-based variational formulation (I.3.6) for the quasi-static MPET equations (I.1.1), together with a robust energy estimate in Theorem I.3.3. We continue in Section I.4 by proposing a general class of compatible semi-discretizations (I.4.1) of this formulation, and estimate the *a priori* discretization errors in Proposition I.4.1 and the semi-discrete errors for a specific choice of finite element spaces in Theorem I.4.2 and Proposition I.4.4. These theoretical results are corroborated by synthetic numerical convergence experiments in Section I.5. In Section I.6, we present a more physiologically realistic numerical experiment using a 4-network MPET model to investigate blood and tissue fluid flow in the human brain. Some conclusions and directions of future research are highlighted in Section III.5.

I.2 Notation and preliminaries

Throughout this paper we use $X \lesssim Y$ to denote the inequality $X \leq CY$ with a generic constant $C > 0$ which is independent of mesh sizes. If needed, we will write C explicitly in inequalities but it can vary across expressions.

I.2.1 Sobolev spaces

Let Ω be a bounded polyhedral domain in $\mathbb{R}^d$ ($d = 1, 2$, or 3) with boundary $\partial\Omega$. We let $L^2(\Omega)$ be the set of square-integrable real-valued functions on Ω. The inner product of $L^2(\Omega)$ and the induced norm are denoted by $\langle \cdot, \cdot \rangle$ and $\| \cdot \|$, respectively. For a finite-dimensional inner product space $\mathbb{X}$, typically $\mathbb{X} = \mathbb{R}^d$, let $L^2(\Omega;\mathbb{X})$ be the space of $\mathbb{X}$-valued functions such that each component is in $L^2(\Omega)$. The inner product of $L^2(\Omega;\mathbb{X})$ is naturally defined by the inner product of $\mathbb{X}$ and $L^2(\Omega)$, so we use the same notation $\langle\cdot,\cdot\rangle$ and $\|\cdot\|$ to denote the inner product and norm on $L^2(\Omega;\mathbb{X})$. For a non-negative real-valued function on Ω (or symmetric positive semi-definite tensor-valued function on Ω) w, we also introduce the short-hand notations

$$\langle u, v\rangle_w = \langle wu, v\rangle, \quad \|u\|_w^2 = \langle u, u\rangle_w, \tag{I.2.1}$$

noting that the latter is a norm only when w is strictly positive a.e. on Ω (or is positive definite a.e. on Ω).

For a non-negative integer m, $H^m(\Omega)$ denotes the standard Sobolev spaces of real-valued functions based on the L^2-norm, and $H^m(\Omega;\mathbb{X})$ is defined similarly based on $L^2(\Omega;\mathbb{X})$. To avoid confusion with the weighted L^2-norms cf. (I.2.1) we use $\|\cdot\|_{H^m}$ to denote the H^m-norm (both for $H^m(\Omega)$ and $H^m(\Omega;\mathbb{X})$). For $m \geq 1$, we use $H^m_{0,\Gamma}(\Omega)$ to denote the subspace of $H^m(\Omega)$ with vanishing trace on $\Gamma \subset \partial\Omega$, and $H^m_{0,\Gamma}(\Omega;\mathbb{X})$ is defined similarly [Eva98]. For $\Gamma = \partial\Omega$, we write $H^m_0(\Omega)$ and analogously $H^m_0(\Omega;\mathbb{X})$.

I.2.2 Spaces involving time

We will consider an interval $[0,T]$, $T > 0$. For a reflexive Banach space $\mathcal{X}$, let $C^0([0,T];\mathcal{X})$ denote the set of functions $f : [0,T] \to \mathcal{X}$ that are continuous in $t \in [0,T]$. For an integer $m \geq 1$, we define

$$C^m([0,T];\mathcal{X}) = \{f \mid \partial^i f/\partial t^i \in C^0([0,T];\mathcal{X}),\ 0 \leq i \leq m\},$$

where $\partial^i f/\partial t^i$ is the i-th time derivative in the sense of the Fréchet derivative in $\mathcal{X}$ (see e.g. [Yos80]).

For a function $f : [0,T] \to \mathcal{X}$, we define the space-time norm

$$\|f\|_{L^r([0,T];\mathcal{X})} = \begin{cases} \left(\int_0^T \|f(s)\|_{\mathcal{X}}^r \,\mathrm{d}s\right)^{1/r}, & 1 \leq r < \infty, \\ \operatorname{ess\,sup}_{t\in[0,T]} \|f(t)\|_{\mathcal{X}}, & r = \infty. \end{cases}$$

We define the Bochner spaces $W^{k,r}([0,T];\mathcal{X})$ for a non-negative integer k and $1 \leq r \leq \infty$ as the closure of $C^k([0,T];\mathcal{X})$ with the norm $\|f\|_{W^{k,r}([0,T];\mathcal{X})} = \sum_{i=0}^k \|\partial^i f/\partial t^i\|_{L^r([0,T];\mathcal{X})}$.

I.2.3 Finite element spaces

Let $\mathcal{T}_h$ be an admissible, conforming, simplicial tessellation of the domain Ω. For any integer $k \geq 1$, we let $\mathcal{P}_k(\mathcal{T}_h)$ denote the space of continuous piecewise polynomials of order k defined relative to $\mathcal{T}_h$, and $\mathcal{P}_k^d(\mathcal{T}_h)$ as the space of d-tuples with components in $\mathcal{P}_k$. We will typically omit the reference to $\mathcal{T}_h$ when context allows. We let $\mathring{\mathcal{P}}_k$ denote the restriction of these piecewise polynomial spaces to conform with given essential homogeneous boundary conditions.

I.2.4 Parameter values

Based on physical considerations and typical applications, we will make the following assumptions on the material parameter values. First, we assume that the Biot-Willis coefficients $\alpha_j \in (0,1]$, $j = 1, \dots, A$, and the storage coefficients $c_j > 0$ are constant in time for $j = 1, \dots, A$. In the analysis, we will pay particular attention to robustness of estimates with respect to arbitrarily large λ and arbitrarily small (but not vanishing) c_j's. We also comment on the case $c_j = 0$ in Remark I.4.3.

We will assume that the hydraulic conductivities K_j are constant in time, but possibly spatially-varying and that these satisfy standard ellipticity constraints: i.e. there exist positive constants K_j^- and K_j^+ such that

$$K_j^- \le K_j(x) \le K_j^+ \quad \forall\, x \in \Omega.$$

We assume that the transfer coefficients $\xi_{j\leftarrow i}$ are constant in time and non-negative: i.e. $\xi_{j\leftarrow i}(x) \ge 0$ for $1 \le i, j \le A$, $x \in \Omega$.

I.2.5 Boundary conditions

We will consider (I.1.1) augmented by the following standard boundary conditions. First, we assume that the boundary decomposes in two parts: $\partial\Omega = \Gamma_D \cup \Gamma_N$ with $\Gamma_D \cap \Gamma_N = \emptyset$ and $|\Gamma_D|, |\Gamma_N| > 0$ where $|\Gamma|$ is the Lebesgue measure of Γ. We use n to denote the outward unit normal vector field on $\partial\Omega$. Relative to this partition, we consider the homogeneous boundary conditions

$$u = 0 \quad \text{on } \Gamma_D, \tag{I.2.2a}$$

$$C\varepsilon(u) \cdot n = 0 \quad \text{on } \Gamma_N, \tag{I.2.2b}$$

$$p_j = 0 \quad \text{on } \partial\Omega \quad \text{for } j = 1, \dots, A. \tag{I.2.2c}$$

The subsequent formulation and analysis can easily be extended to cover inhomogeneous and other types of boundary conditions.

I.2.6 Key inequalities

For the space $V = H^1_{0,\Gamma_D}(\Omega)$, Korn's inequality [Bra01, p. 288] holds; i.e. there exists a constant $C > 0$ depending only on Ω and Γ_D such that

$$\|u\| \le C\|\varepsilon(u)\| \quad \forall\, u \in V. \tag{I.2.3}$$

Furthermore, for the combination of spaces V and $Q_0 = L^2(\Omega)$, the following (continuous Stokes) inf-sup condition holds: there exists a constant $C > 0$ depending only on Ω and Γ_D such that

$$\sup_{u \in V} \frac{\langle \operatorname{div} u, q\rangle}{\|u\|_{H^1}} \ge C\|q\| \quad \forall\, q \in L^2(\Omega). \tag{I.2.4}$$

Our discretization schemes will also satisfy corresponding discrete versions of Korn's inequality and the inf-sup condition with constants independent of the discretization.

I.2.7 Initial conditions

The MPET equations (I.1.1) must also be complemented by appropriate initial conditions. In particular, in agreement with the assumption that $c_j > 0$ for $j = 1, \dots, A$, we assume that initial conditions are given for all p_j:

$$p_j(x, 0) = p_j^0(x), \quad x \in \Omega, \quad j = 1, \dots, A. \tag{I.2.5}$$

Given such p_j^0, we note that we may compute $u(x, 0) = u^0(x)$ from (I.1.1a), which in particular yields $\operatorname{div} u(x, 0) = \operatorname{div} u^0(x)$ for $x \in \Omega$. In the following, we will assume that any initial conditions given are compatible in the sense described here.

I.3 A new formulation for multiple-network poroelasticity

In this section, we introduce a new variational formulation for the quasi-static multiple-network poroelasticity equations targeting the incompressible and nearly incompressible regime. Inspired by [LMW17; OR16], we introduce an additional variable, namely the *total pressure*. In the subsequent subsections, we present the augmented governing equations, introduce a corresponding variational formulation, and demonstrate the robustness of this formulation via an energy estimate.

I.3.1 Governing equations introducing the total pressure

Let u and p_j for $j = 1, \dots, A$ be solutions of (I.1.1) with boundary conditions given by (I.2.2), initial conditions given by (I.2.5) and recall the isotropic stiffness tensor assumption, cf. (I.1.2). Additionally, we now introduce the total pressure p_0 defined as

$$p_0 = \lambda \operatorname{div} u - \textstyle\sum_{j=1}^{A} \alpha_j p_j. \tag{I.3.1}$$

Defining $\alpha_0 = 1$ for the purpose of short-hand, and rearranging, we thus have that

$$\operatorname{div} u = \lambda^{-1} \textstyle\sum_{i=0}^{A} \alpha_i p_i. \tag{I.3.2}$$

For simplicity, we denote $\alpha = (\alpha_0, \alpha_1, \dots, \alpha_A)$ and $p = (p_0, p_1, \dots, p_A)$, and we can thus write

$$\textstyle\sum_{i=0}^{A} \alpha_i p_i = \alpha \cdot p$$

in the following.

Inserting (I.3.2) and its time-derivative into (I.1.1b), we obtain an augmented system of quasi-static multiple-network poroelasticity equations: for $t \in (0, T]$, find the displacement vector field u and the pressure scalar fields p_i for $i = 0, \dots, A$ such that

$$\operatorname{div} u - \lambda^{-1} \alpha \cdot p = 0, \tag{I.3.3a}$$

$$-\operatorname{div}(2\mu\varepsilon(u) + p_0 I) = f, \tag{I.3.3b}$$

$$c_j \dot{p}_j + \alpha_j \lambda^{-1} \alpha \cdot \dot{p} - \operatorname{div}(K_j \nabla p_j) + S_j = g_j \quad j = 1, \dots, A. \tag{I.3.3c}$$

We note that $p_0(x, 0)$ can be computed from (I.2.5) and (I.3.1).

Remark I.3.1. *In the limit $\lambda = \infty$, the equations for the displacement u and total pressure p_0, and the network pressures p_i decouple, and* (I.3.3) *reduces to a Stokes system for (u, p_0) and a system of parabolic equations for p_j:*

$$\begin{aligned} -\operatorname{div}(2\mu\varepsilon(u) + p_0 I) &= f, \\ \operatorname{div} u &= 0, \\ c_j \dot{p}_j - \operatorname{div}(K_j \nabla p_j) + S_j &= g_j \quad j = 1, \ldots, A. \end{aligned}$$

We next present and study a continuous variational formulation based on the total pressure formulation (I.3.3) of the quasi-static multiple-network poroelasticity equations.

I.3.2 Variational formulation

With reference to the notation for domains and Sobolev spaces as introduced in Section I.2, let

$$V = H^1_{0,\Gamma_D}(\Omega; \mathbb{R}^d), \quad Q_0 = L^2(\Omega), \quad Q_j = H^1_0(\Omega) \quad j = 1, \ldots, A. \qquad \text{(I.3.5)}$$

Also denote $Q = Q_0 \times Q_1 \times \cdots \times Q_A$.

Multiplying (I.3.3) by test functions and integrating by parts with boundary conditions given by (I.2.2) and initial conditions given by (I.2.5) yield the following variational formulation: given compatible u^0 and p^0_j, f and g_j for $j = 1, \ldots, A$, find $u \in C^1([0, T]; V)$ and $p_i \in C^1([0, T], Q_i)$ for $i = 0, \ldots, A$ such that

$$\begin{aligned} \langle 2\mu\varepsilon(u), \varepsilon(v)\rangle + \langle p_0, \operatorname{div} v\rangle &= \langle f, v\rangle & \forall\, v \in V, \quad & \text{(I.3.6a)} \\ \langle \operatorname{div} u, q_0\rangle - \langle \lambda^{-1}\alpha \cdot p, q_0\rangle &= 0 & \forall\, q_0 \in Q_0, \quad & \text{(I.3.6b)} \\ \langle c_j \dot{p}_j + \alpha_j \lambda^{-1} \alpha \cdot \dot{p} + S_j, q_j\rangle + \langle K_j \nabla p_j, \nabla q_j\rangle &= \langle g_j, q_j\rangle & \forall\, q_j \in Q_j, \quad & \text{(I.3.6c)} \end{aligned}$$

for $j = 1, \ldots, A$ and such that $u(\cdot, 0) = u^0(\cdot)$ and $p_j(\cdot, 0) = p^0_j(\cdot)$ for $j = 1, \ldots, A$.

The following lemma is a modified version of Lemma 3.1 in [Lee16] and will be used in the energy estimates below. For the sake of completeness, we present its proof here.

Lemma I.3.2. *Let $\mathcal{F}$, $\mathcal{G}$, $\mathcal{G}_1$, $\mathcal{X} : [0, T] \to \mathbb{R}$ be continuous, non-negative functions. Suppose that $\mathcal{X}(t)$ satisfies*

$$\mathcal{X}^2(t) \leq C_0 \mathcal{X}^2(0) + C_1 \mathcal{X}(0) + \mathcal{G}_1(t) + \int_0^t [\mathcal{F}(s)\mathcal{X}(s) + \mathcal{G}(s)] \, \mathrm{d}s, \qquad \text{(I.3.7)}$$

for all $t \in [0, T]$ with constants $C_0 \geq 1$ and $C_1 > 0$. Then for any $t \in [0, T]$,

$$\mathcal{X}(t) \lesssim \mathcal{X}(0) + \max\left\{ C_1 + \int_0^t \mathcal{F}(s) \, \mathrm{d}s, \left(\mathcal{G}_1(t) + \int_0^t \mathcal{G}(s) \, \mathrm{d}s \right)^{\frac{1}{2}} \right\}. \qquad \text{(I.3.8)}$$

Proof. It suffices to show the estimate for the smallest t such that

$$\mathcal{X}(t) = \max_{s\in[0,T]} \mathcal{X}(s).$$

By this assumption, $\mathcal{X}(t) = \max_{s\in[0,T]} \mathcal{X}(s)$ and $\mathcal{X}(s) < \mathcal{X}(t)$ for all $0 \le s < t$. We now consider two cases: either

$$C_1\mathcal{X}(0) + \int_0^t \mathcal{F}(s)\mathcal{X}(s)\,\mathrm{d}s \ge \mathcal{G}_1(t) + \int_0^t \mathcal{G}(s)\,\mathrm{d}s \tag{I.3.9}$$

or

$$C_1\mathcal{X}(0) + \int_0^t \mathcal{F}(s)\mathcal{X}(s)\,\mathrm{d}s < \mathcal{G}_1(t) + \int_0^t \mathcal{G}(s)\,\mathrm{d}s. \tag{I.3.10}$$

If (I.3.9) holds, then (I.3.7) gives

$$\begin{aligned}\mathcal{X}^2(t) &\le C_0\mathcal{X}^2(0) + 2C_1\mathcal{X}(0) + 2\int_0^t \mathcal{F}(s)\mathcal{X}(s)\,\mathrm{d}s \\ &\le C_0\mathcal{X}^2(0) + 2C_1\mathcal{X}(0) + 2\mathcal{X}(t)\int_0^t \mathcal{F}(s)\,\mathrm{d}s.\end{aligned}$$

Dividing both sides by $\mathcal{X}(t)$ yields (I.3.8) because $\mathcal{X}(t) \ge \mathcal{X}(0)$.

On the other hand, if (I.3.10) is the case, then (I.3.7) gives

$$\mathcal{X}^2(t) \le C_0\mathcal{X}^2(0) + 2\mathcal{G}_1(t) + 2\int_0^t \mathcal{G}(s)\,\mathrm{d}s,$$

and taking the square roots of both sides gives (I.3.8). ■

Theorem I.3.3 below establishes a basic energy estimate for solutions of (I.3.6), but also for solutions with an additional right-hand side (for the sake of reuse in the *a priori* error estimates).

Theorem I.3.3 (Energy estimate for quasi-static multiple-network poroelasticity)**.** *For given $f \in C^1([0,T];L^2(\Omega))$, $\beta \in C^1([0,T];L^2(\Omega))^{A+1}$ and $\gamma_j \in L^2([0,T];L^2(\Omega))$ for $j = 1,\dots,A$, assume that $u \in C^1([0,T];V)$ and $p_i \in C^1([0,T];Q_i)$ for $i = 0,\dots,A$ solve*

$$\begin{aligned}\langle 2\mu\varepsilon(u), \varepsilon(v)\rangle + \langle p_0, \operatorname{div} v\rangle &= \langle f, v\rangle \quad &\forall\, v \in V, \qquad &\text{(I.3.11a)}\\ \langle \operatorname{div} u, q_0\rangle - \langle \lambda^{-1}\alpha\cdot p, q_0\rangle &= \langle g_0, q_0\rangle \quad &\forall\, q_0 \in Q_0, \qquad &\text{(I.3.11b)}\\ \langle c_j\dot{p}_j + \alpha_j\lambda^{-1}\alpha\cdot\dot{p} + S_j, q_j\rangle + \langle K_j\nabla p_j, \nabla q_j\rangle &= \langle g_j, q_j\rangle \quad &\forall\, q_j \in Q_j, \qquad &\text{(I.3.11c)}\end{aligned}$$

for $j = 1,\dots,A$ and $u(0) = u^0$ and $p_j(0) = p_j^0$ for $j = 1,\dots,A$, and where $g_0 = -\lambda^{-1}\alpha\cdot\beta$ and $g_j = \gamma_j + \alpha_j\lambda^{-1}\alpha\cdot\dot{\beta}$ for $j = 1,\dots,A$. Then the following energy estimate holds for all $t \in (0,T]$:

$$
\begin{aligned}
&\|\varepsilon(u(t))\|_{2\mu} + \sum_{j=1}^{A} \|p_j(t)\|_{c_j} + \|\alpha \cdot p(t)\|_{\lambda^{-1}} \\
&\qquad + \left(\int_0^t \sum_{j=1}^{A} \| \nabla p_j\|_{K_j}^2 + \sum_{i,j=1}^{A} \|p_j - p_i\|_{\xi_{j\leftarrow i}}^2 \,\mathrm{d}s \right)^{\frac{1}{2}} \\
&\lesssim I_0 + \int_0^t \left[\|\dot{f}\| + \|\alpha \cdot \dot{\beta}\|_{\lambda^{-1}} \right] \mathrm{d}s + \left(\|f(t)\|^2 + \int_0^t \sum_{j=1}^{A} \|\gamma_j\|^2 \,\mathrm{d}s \right)^{\frac{1}{2}}, \qquad \text{(I.3.12)}
\end{aligned}
$$

where

$$
I_0 = \|\varepsilon(u(0))\|_{2\mu} + \sum_{j=1}^{A} \|p_j(0)\|_{c_j} + \|\alpha \cdot p(0)\|_{\lambda^{-1}} + \|f(0)\|, \qquad \text{(I.3.13)}
$$

and where the inequality constant is independent of λ *and* c_j *for* $j = 1, \dots, A$, *but dependent on* K_j *for* $j = 1, \dots, A$.

Moreover,

$$
\|p_0(t)\| \lesssim \|\varepsilon(u(t))\|_{2\mu} \qquad \text{(I.3.14)}
$$

holds.

Proof. The result follows using standard techniques. Note that the time derivative of (I.3.11b) reads as

$$
\langle \operatorname{div} \dot{u}, q_0 \rangle - \langle \lambda^{-1} \alpha \cdot \dot{p}, q_0 \rangle = -\langle \lambda^{-1} \alpha \cdot \dot{\beta}, q_0 \rangle \quad \forall\, q_0 \in Q_0. \qquad \text{(I.3.15)}
$$

Taking $v = \dot{u}$ in (I.3.11a), $q_j = p_j$ for $1 \le j \le A$ in (I.3.11c) and $q_0 = -p_0$ in (I.3.15), summing the equations, and rearranging some constants (recalling that $\alpha_0 = 1$), we obtain:

$$
\begin{aligned}
\langle \varepsilon(u), \varepsilon(\dot{u}) \rangle_{2\mu} + \sum_{j=1}^{A} \langle \dot{p}_j, p_j \rangle_{c_j} + \sum_{j=1}^{A} \langle S_j, p_j \rangle + \sum_{j=1}^{A} \| \nabla p_j\|_{K_j}^2 + \langle \alpha \cdot \dot{p}, \alpha \cdot p \rangle_{\lambda^{-1}} \\
= \langle f, \dot{u} \rangle + \langle \lambda^{-1} \alpha \cdot \dot{\beta}, \alpha \cdot p \rangle + \sum_{j=1}^{A} \langle \gamma_j, p_j \rangle. \qquad \text{(I.3.16)}
\end{aligned}
$$

By definition (I.1.3), and the assumption that $\xi_{j\leftarrow i} = \xi_{i\leftarrow j}$, it follows that

$$
\sum_{j=1}^{A} \langle S_j, p_j \rangle = \sum_{j=1}^{A} \sum_{i=1}^{A} \langle \xi_{j\leftarrow i}(p_j - p_i), p_j \rangle = \frac{1}{2} \sum_{j=1}^{A} \sum_{i=1}^{A} \|p_j - p_i\|_{\xi_{j\leftarrow i}}^2. \qquad \text{(I.3.17)}
$$

Combining (I.3.16) and (I.3.17), and pulling out the time derivatives, we find that

$$\frac{1}{2}\frac{\mathrm{d}}{\mathrm{dt}}\left(\|\varepsilon(u)\|_{2\mu}^2+\sum_{j=1}^{A}\|p_j\|_{c_j}^2+\|\alpha\cdot p\|_{\lambda^{-1}}^2\right)+\sum_{j=1}^{A}\|\nabla p_j\|_{K_j}^2+\frac{1}{2}\sum_{i,j=1}^{A}\|p_j-p_i\|_{\xi_{j\leftarrow i}}^2$$
$$=\langle f,\dot{u}\rangle+\langle\lambda^{-1}\alpha\cdot\dot{\beta},\alpha\cdot p\rangle+\sum_{j=1}^{A}\langle\gamma_j,p_j\rangle.$$

Integrating in time from 0 to t gives

$$\begin{aligned}
&\|\varepsilon(u(t))\|_{2\mu}^2+\sum_{j=1}^{A}\|p_j(t)\|_{c_j}^2+\|\alpha\cdot p(t)\|_{\lambda^{-1}}^2\\
&\qquad+\int_0^t 2\left[\sum_{j=1}^{A}\|\nabla p_j\|_{K_j}^2+\sum_{i,j=1}^{A}\|p_j-p_i\|_{\xi_{j\leftarrow i}}^2\right]\mathrm{d}s\\
&\qquad=\|\varepsilon(u(0))\|_{2\mu}^2+\sum_{j=1}^{A}\|p_j(0)\|_{c_j}^2+\|\alpha\cdot p(0)\|_{\lambda^{-1}}^2\\
&\qquad\quad+2\int_0^t\left[\langle f,\dot{u}\rangle+\langle\lambda^{-1}\alpha\cdot\dot{\beta},\alpha\cdot p\rangle+\sum_{j=1}^{A}\langle\gamma_j,p_j\rangle\right]\mathrm{d}s. \qquad (\text{I.3.18})
\end{aligned}$$

Note first that

$$\begin{aligned}
\int_0^t\langle f,\dot{u}\rangle\,\mathrm{d}s&=\langle f(t),u(t)\rangle-\langle f(0),u(0)\rangle-\int_0^t\langle\dot{f},u\rangle\,\mathrm{d}s\\
&\leq\|f(t)\|\|u(t)\|+\|f(0)\|\|u(0)\|+\int_0^t\|\dot{f}\|\|u\|\,\mathrm{d}s\\
&\lesssim\|f(t)\|\|\varepsilon(u(t))\|_{2\mu}+\|f(0)\|\|\varepsilon(u(0))\|_{2\mu}+\int_0^t\|\dot{f}\|\|\varepsilon(u)\|_{2\mu}\,\mathrm{d}s\\
&\lesssim\frac{1}{4\epsilon_0}\|f(t)\|^2+\epsilon_0\|\varepsilon(u(t))\|_{2\mu}^2+\|f(0)\|\|\varepsilon(u(0))\|_{2\mu}+\int_0^t\|\dot{f}\|\|\varepsilon(u)\|_{2\mu}\,\mathrm{d}s,
\end{aligned}$$

using Young's inequality (with ϵ) for any $\epsilon_0>0$. Again using Young's inequality with ϵ, Poincare's inequality on Q_j and the assumption of uniform positivity of K_j on the last terms on the right hand side of (I.3.18), we have that for each $j=1,\ldots,A$ and any $\epsilon_j>0$:

$$\langle\gamma_j,p_j\rangle\leq\frac{1}{4\epsilon_j}\|\gamma_j\|^2+\epsilon_j\|p_j\|^2\lesssim\frac{1}{4\epsilon_j}\|\gamma_j\|^2+\epsilon_j\|\nabla p_j\|_{K_j}^2,$$

with the last inequality depending on K_j. Choosing ϵ_j for $j=0,1,\ldots,A$ appropriately and transferring terms thus gives

$$
\begin{aligned}
&\|\varepsilon(u(t))\|_{2\mu}^2 + \sum_{j=1}^{A} \|p_j(t)\|_{c_j}^2 + \|\alpha \cdot p(t)\|_{\lambda^{-1}}^2 \\
&\qquad + \int_0^t \left[\sum_{j=1}^{A} \| \nabla p_j\|_{K_j}^2 + \sum_{i,j=1}^{A} \|p_j - p_i\|_{\xi_{j\leftarrow i}}^2 \right] \mathrm{d}s \\
&\lesssim \|\varepsilon(u(0))\|_{2\mu}^2 + \|f(0)\| \|\varepsilon(u(0))\|_{2\mu} + \sum_{j=1}^{A} \|p_j(0)\|_{c_j}^2 + \|\alpha \cdot p(0)\|_{\lambda^{-1}}^2 + \|f(t)\|^2 \\
&\qquad + \int_0^t \sum_{j=1}^{A} \left[\|\gamma_j\|^2 + \|\dot{f}\| \|\varepsilon(u)\|_{2\mu} + \langle \lambda^{-1} \alpha \cdot \dot{\beta}, \alpha \cdot p \rangle \right] \mathrm{d}s.
\end{aligned}
$$

Finally, the Cauchy-Schwarz inequality combined with Lemma I.3.2, taking $C_1 = \|f(0)\|$, $\mathcal{G}_1(t) = \|f(t)\|^2$, and

$$
\begin{aligned}
\mathcal{X}(t)^2 &= \|\varepsilon(u)\|_{2\mu}^2 + \sum_{j=1}^{A} \|p_j\|_{c_j}^2 + \|\alpha \cdot p\|_{\lambda^{-1}}^2 \\
&\qquad + \int_0^t \left[\sum_{j=1}^{A} \| \nabla p_j\|_{K_j}^2 + \sum_{i,j=1}^{A} \|p_j - p_i\|_{\xi_{j\leftarrow i}}^2 \right] \mathrm{d}s, \\
\mathcal{F}(s) &= \|\dot{f}(s)\| + \|\alpha \cdot \dot{\beta}(s)\|_{\lambda^{-1}}, \\
\mathcal{G}(s) &= \sum_{j=1}^{A} \|\gamma_j(s)\|^2,
\end{aligned}
$$

give the desired estimate.

The bound for p_0 immediately follows from an inf-sup type argument: by the choice of V and Q_0, the inf-sup condition (see e.g. [Bra01]), by (I.3.6a), and Korn's inequality, we obtain that for any $t \in (0, T]$:

$$
\|p_0(t)\| \lesssim \sup_{v \in V, v \neq 0} \frac{|\langle \operatorname{div} v, p_0(t) \rangle|}{\|v\|_{H^1}} = \sup_{v \in V, v \neq 0} \frac{|\langle 2\mu\varepsilon(u(t)), \varepsilon(v) \rangle|}{\|v\|_{H^1}} \lesssim \|\varepsilon(u(t))\|_{2\mu} \tag{I.3.19}
$$

holds with constant depending on μ. ■

We remark that Theorem I.3.3 gives a uniform bound on u in $L^\infty(0, T; V)$, $p_0 \in L^\infty(0, T; Q_0)$, and p_j in $L^2(0, T; Q_j)$ for $j = 1, \dots, A$, for arbitrarily large λ and arbitrarily small $c_j > 0$ for $j = 1, \dots, A$ in particular.

I.4 Semi-discretization of multiple network poroelasticity

In this section, we present a finite element semi-discretization of the total pressure variational formulation (I.3.3) of the quasi-static multiple-network poroelasticity equations. We introduce both abstract compatibility assumptions (**A1** and **A2** below) and a specific choice of conforming, mixed finite element spaces. We end this section by an *a priori* error estimate for the discretization error in the abstract case, and an *a priori* semi-discrete error estimate for a specific family of mixed finite element spaces.

I.4.1 Finite element semi-discretization

Let $\mathcal{T}_h$ denote a conforming, shape-regular, simplicial discretization of Ω with discretization size $h > 0$. Relative to $\mathcal{T}_h$, we define finite element spaces $V_h \subset V$ and $Q_{i,h} \subset Q_i$ for $i = 0, \dots, A$. We assume that V_h and $Q_{i,h}$, $i = 0, \dots, A$ satisfy two compatibility assumptions (**A1**, **A2**) as follows:

A1: $V_h \times Q_{0,h}$ is a stable (in the Brezzi [Bre74] sense) finite element pair for the Stokes equations.

A2: $Q_{j,h}$ is an H^1-conforming finite element space for $j = 1, \dots, A$.

We also denote $Q_h = Q_{0,h} \times Q_{1,h} \times \cdots \times Q_{A,h}$.

With reference to these element spaces, we define the following semi-discrete total pressure-based variational formulation of the quasi-static multiple-network poroelasticity equations: for $t \in (0, T]$, find $u_h(t) \in V_h$ and $p_{i,h}(t) \in Q_{i,h}$ for $i = 0, \dots, A$ such that

$$\langle 2\mu\varepsilon(u_h), \varepsilon(v)\rangle + \langle p_{0,h}, \operatorname{div} v\rangle = \langle f, v\rangle \qquad \forall\, v \in V_h, \tag{I.4.1a}$$

$$\langle \operatorname{div} u_h, q_0\rangle - \langle \lambda^{-1}\alpha \cdot p_h, q_0\rangle = 0 \qquad \forall\, q_0 \in Q_{0,h}, \tag{I.4.1b}$$

$$\langle c_j \dot{p}_{j,h} + \alpha_j \lambda^{-1}\alpha \cdot \dot{p}_h + S_{j,h}, q_j\rangle + \langle K_j \nabla p_{j,h}, \nabla q_j\rangle = \langle g_j, q_j\rangle \quad \forall\, q_j \in Q_{j,h}, \tag{I.4.1c}$$

for $j = 1, \dots, A$. Here $S_{j,h} = \sum_{i=1}^{A} \xi_{j\leftarrow i}(p_{j,h} - p_{i,h})$ cf. (I.1.3) and $p_h = (p_{0,h}, \dots, p_{A,h})$.

I.4.2 Auxiliary interpolation operators

As a preliminary step for the *a priori* error analysis of the semi-discrete formulation, we introduce a set of auxiliary interpolation operators. In particular, we define interpolation operators

$$\Pi_h^V : V \to V_h, \qquad \Pi_h^{Q_i} : Q_i \to Q_{i,h} \quad i = 0, \dots, A,$$

as follows.

First, for any $(u, p_0) \in V \times Q_0$, we define its interpolant $(\Pi_h^V u, \Pi_h^{Q_0} p_0) \in V_h \times Q_{0,h}$ as the unique discrete solution to the Stokes-type system of equations:

$$\langle 2\mu\varepsilon(\Pi_h^V u), \varepsilon(v)\rangle + \langle \Pi_h^{Q_0} p_0, \operatorname{div} v\rangle = \langle 2\mu\varepsilon(u), \varepsilon(v)\rangle + \langle p_0, \operatorname{div} v\rangle \quad \forall\, v \in V_h, \tag{I.4.2a}$$

$$\langle \operatorname{div} \Pi_h^V u, q_0 \rangle = \langle \operatorname{div} u, q_0 \rangle \qquad \forall\, q_0 \in Q_{0,h}. \tag{I.4.2b}$$

The interpolant is well-defined and bounded by assumption **A1** and the given boundary conditions.

Second, for $j = 1, \dots, A$, we define the interpolation operators $\Pi_h^{Q_j}$ as a weighted elliptic projection: i.e. for any $p_j \in Q_j$, we define its interpolant $\Pi_h^{Q_j} p_j \in Q_{j,h}$ as the unique solution of

$$\langle K_j \nabla \Pi_h^{Q_j} p_j, q \rangle = \langle K_j \nabla p_j, \nabla q \rangle \quad \forall\, q \in Q_{j,h}. \tag{I.4.3}$$

This interpolant is well-defined and bounded by assumption **A2** and the given boundary conditions.

I.4.3 Specific choice of finite element spaces: a family of Taylor-Hood type elements

In this paper, we will pay particular attention to one specific family of mixed finite element spaces for the total pressure-based semi-discretization of the multiple-network poroelasticity equations, namely a family of Taylor-Hood type element spaces [BP79; TH73]. More precisely, we note that assumptions **A1** and **A2** are easily satisfied by the conforming mixed finite element space pairing:

$$V_h = \mathring{\mathcal{P}}_{l+1}^d(\mathcal{T}_h), \quad Q_{0,h} = \mathcal{P}_l(\mathcal{T}_h), \quad Q_{j,h} = \mathring{\mathcal{P}}_{l_j}(\mathcal{T}_h), \tag{I.4.4}$$

for polynomial degrees $l \geq 1$ and $l_j \geq 1$ for $j = 1, \dots, A$. We will refer to the spaces (I.4.4) as Taylor-Hood type elements of order l and l_j. The superimposed ring in (I.4.4) denotes the restriction of the piecewise polynomial spaces to conform to the given essential boundary conditions.

For this choice of finite element spaces, in particular, for the Taylor-Hood elements of order l, the following error estimate holds for the Stokes-type interpolant defined by (I.4.2) (see e.g. [BF91; Bof94; Bof97]). For $1 \leq m \leq l+1$, if $u \in H_{0,\Gamma_D}^{m+1}(\Omega)$ and $p_0 \in H^m$, then

$$\|u - \Pi_h^V u\|_{H^1} + \|p_0 - \Pi_h^{Q_0} p_0\| \lesssim h^m \left(\|u\|_{H^{m+1}} + \|p_0\|_{H^m} \right). \tag{I.4.5}$$

Moreover, the following error estimate holds for the elliptic interpolants defined by (I.4.3) (see e.g. [BS08, Chap. 5]): For $j = 1, \dots, A$, for $1 \leq m \leq l_j$, if $p_j \in H_0^{m+1}$, it holds that

$$\|p_j - \Pi_h^{Q_j} p_j\|_{H^1} \lesssim h^m \|p_j\|_{H^{m+1}}, \tag{I.4.6}$$

and under the full elliptic regularity assumption of Ω,

$$\|p_j - \Pi_h^{Q_j} p_j\| \lesssim h^{m+1} \|p_j\|_{H^{m+1}}. \tag{I.4.7}$$

In the next subsection, we show optimal error estimates of semi-discrete solutions assuming that both of the above estimates hold.

I.4.4 Semi-discrete *a priori* error analysis

Assume that (u, p) is a solution of the continuous quasi-static multiple-network poroelasticity equations (I.3.6) and that (u_h, p_h) solves the corresponding semi-discrete problem (I.4.1). We introduce the semi-discrete (approximation) errors

$$e_u(t) \equiv u(t) - u_h(t), \quad e_{p_j}(t) \equiv p_j(t) - p_{j,h}(t) \quad j = 0, \dots, A, \tag{I.4.8}$$

and denote $e_p = (e_{p_0}, \dots, e_{p_A})$. We also introduce the standard decomposition of the errors into interpolation (superscript I) and discretization (superscript h) errors:

$$e_u \equiv e_u^I + e_u^h, \quad e_u^I \equiv u - \Pi_h^V u, \quad e_u^h \equiv \Pi_h^V u - u_h, \tag{I.4.9a}$$

$$e_{p_j} \equiv e_{p_j}^I + e_{p_j}^h, \quad e_{p_j}^I \equiv p_j - \Pi_h^{Q_j} p_j, \quad e_{p_j}^h \equiv \Pi_h^{Q_j} p_j - p_{j,h} \quad j = 0, \dots, A. \tag{I.4.9b}$$

Proposition I.4.1 below provides estimates for the discretization errors that are robust with respect to c_j and λ. In particular, the implicit constants in the estimates are uniformly bounded for arbitrarily large λ and arbitrarily small $c_j > 0$ for $j = 1, \dots, A$. We also note that the discretization errors of u in the $L^\infty(0, T; V)$-norm and p_j in the $L^2(0, T; Q_j)$-norms for $j = 1, \dots, A$ converge at a higher rate than the corresponding interpolation errors, as the discretization errors are bounded essentially by the initial discretization error of u in the V-norm, by the initial discretization error of p_i in the L^2-norm for $i = 0, \dots, A$ and by the interpolation error of p_i in the $L^2(0, T; L^2)$-norm.

Proposition I.4.1. *Assume that $(u, p) \in C^1(0, T; V) \times C^1(0, T; Q)$ solves the total pressure-based variational formulation of the MPET equations* (I.3.6) *for given f and g_j for $j = 1, \dots, A$. Assume that $V_h \times Q_h$ satisfies assumptions **A1**-**A2**, that $(u_h, p_h) \in C^1(0, T; V_h) \times C^1(0, T; Q_h)$ solves the corresponding finite element semi-discrete problem* (I.4.1)*, and that the discretization errors e_u^h and e_p^h are defined by* (I.4.9)*. Then, the following estimate holds for all $t \in (0, T]$:*

$$\begin{aligned} &\|\varepsilon(e_u^h(t))\|_{2\mu} + \sum_{j=1}^{A} \|e_{p_j}^h(t)\|_{c_j} + \|\alpha \cdot e_p^h(t)\|_{\lambda^{-1}} \\ &\qquad + \left(\int_0^t \sum_{j=1}^{A} \| \nabla e_{p_j}^h \|_{K_j}^2 + \sum_{i,j=1}^{A} \|e_{p_j}^h - e_{p_i}^h\|_{\xi_{j \leftarrow i}}^2 \, \mathrm{d}s \right)^{\frac{1}{2}} \\ &\lesssim E_0^h + \int_0^t \|\alpha \cdot e_p^I\|_{\lambda^{-1}} \, \mathrm{d}s + \left(\int_0^t \sum_{j=1}^{A} \|c_j \dot{e}_{p_j}^I + S_j(e_p^I)\|^2 \, \mathrm{d}s \right)^{\frac{1}{2}}, \end{aligned} \tag{I.4.10}$$

with an implicit constant independent of h, T, λ, c_j and $\xi_{j \leftarrow i}$ for $i, j = 1, \dots, A$ where $S_j(e_p) = \sum_{i=1}^{A} \xi_{j \leftarrow i}(e_{p_j} - e_{p_i})$ and

$$E_0^h = \|\varepsilon(e_u^h(0))\|_{2\mu} + \textstyle\sum_{j=1}^{A} \|e_{p_j}^h(0)\|_{c_j} + \|\alpha \cdot e_p^h(0)\|_{\lambda^{-1}}. \tag{I.4.11}$$

Moreover, for $t \in (0, T]$,

$$\|e^h_{p_0}(t)\| \lesssim \|\varepsilon(e^h_u(t))\|_{2\mu}. \tag{I.4.12}$$

Proof. A standard subtraction of (I.4.1) from (I.3.6) gives that the errors e_u and e_p satisfy the error equations:

$$\langle 2\mu\varepsilon(e_u), \varepsilon(v)\rangle + \langle e_{p_0}, \operatorname{div} v\rangle = 0 \quad \forall\, v \in V_h, \tag{I.4.13a}$$

$$\langle \operatorname{div} e_u, q_0\rangle - \langle \lambda^{-1}\alpha \cdot e_p, q_0\rangle = 0 \quad \forall\, q_0 \in Q_{0,h}, \tag{I.4.13b}$$

$$\langle c_j \dot{e}_{p_j} + \alpha_j\lambda^{-1}\alpha \cdot \dot{e}_p + S_j(e_p), q_j\rangle + \langle K_j \nabla e_{p_j}, \nabla q_j\rangle = 0 \quad \forall\, q_j \in Q_{j,h}, \tag{I.4.13c}$$

for $j = 1, \dots, A$ with $S_j(e_p) = \sum_{i=1}^{A} \xi_{j\leftarrow i}(e_{p_j} - e_{p_i})$. By the definition of the interpolation operators Π_h, we obtain the reduced error representations:

$$\langle 2\mu\varepsilon(e^h_u), \varepsilon(v)\rangle + \langle e^h_{p_0}, \operatorname{div} v\rangle = 0 \qquad \forall\, v \in V_h, \tag{I.4.14a}$$

$$\langle \operatorname{div} e^h_u, q_0\rangle - \langle \lambda^{-1}\alpha \cdot e^h_p, q_0\rangle = \langle g^I_0, q_0\rangle \quad \forall\, q_0 \in Q_{0,h}, \tag{I.4.14b}$$

$$\langle c_j \dot{e}^h_{p_j} + \alpha_j\lambda^{-1}\alpha \cdot \dot{e}^h_p + S_j(e^h_p), q_j\rangle + \langle K_j \nabla e^h_{p_j}, \nabla q_j\rangle = \langle g^I_j, q_j\rangle \quad \forall\, q_j \in Q_{j,h}, \tag{I.4.14c}$$

for $j = 1, \dots, A$ where $g^I_0 = \lambda^{-1}\alpha \cdot e^I_p$ and $g^I_j = -c_j\dot{e}^I_{p_j} - \alpha_j\lambda^{-1}\alpha \cdot \dot{e}^I_p - S_j(e^I_p)$. Noting that e^h_u and e^h_p satisfy the assumptions of Theorem I.3.3 with $f = 0$, $\beta = -e^I_p$ and $\gamma_j = -c_j\dot{e}^I_{p_j} - S_j(e^I_p)$, the semi-discrete discretization error estimate (I.4.10) follows.

Further, by the same techniques as used for the bound (I.3.14), and assumption **A1** combined with (I.4.14a), we observe that

$$\|e^h_{p_0}(t)\| \lesssim \sup_{v\in V_h, v\neq 0} \frac{|\langle \operatorname{div} v, e^h_{p_0}(t)\rangle|}{\|v\|_{H^1}} = \sup_{v\in V_h, v\neq 0} \frac{|\langle 2\mu\varepsilon(e^h_u(t)), \varepsilon(v)\rangle|}{\|v\|_{H^1}} \lesssim \|\varepsilon(e^h_u(t))\|_{2\mu}, \tag{I.4.15}$$

with constant depending on μ, thus yielding (I.4.12). ■

We now consider error estimates associated with the specific choice of Taylor-Hood type finite element spaces as introduced in Section I.4.3. Theorem I.4.2 below presents a complete semi-discrete error estimate for this case, and is easily extendable to other elements satisfying **A1** and **A2**.

Theorem I.4.2. *Assume that* (u, p) *and* (u_h, p_h) *are defined as in Proposition I.4.1 over Taylor-Hood type elements of order* l *and* l_j *for* $j = 1, \dots, A$ *as defined by* (I.4.4)*, and that* (e_u, e_p) *is defined by* (I.4.8). *Assume that* (u, p) *is sufficiently regular. Then the following three estimates hold for all* $t \in (0, T]$ *with implicit* *constants independent of* h, T, λ, c_j *and* $\xi_{j\leftarrow i}$ *for* $i, j = 1, \dots, A$. *First,*

$$\begin{aligned}\|u(t)-u_h(t)\|_{H^1} \lesssim E_0^h + h^{l+1}\left(\|u(t)\|_{H^{l+2}} + \|u\|_{L^1(0,t;H^{l+2})} + \|p_0\|_{L^1(0,t;H^{l+1})}\right) \\ + \sum_{j=1}^{A} h^{l_j+1}\left(\|p_j\|_{L^1(0,t;H^{l_j+1})} + \|\dot{p_j}, p_j\|_{L^2(0,t;H^{l_j+1})}\right), \end{aligned} \qquad \text{(I.4.16)}$$

holds with E_0^h *defined in* (I.4.11), *and*

$$\|\dot{p_j}, p_j\|_{L^2(0,t;H^{l_j+1})} \equiv \|\dot{p}_j\|_{L^2(0,t;H^{l_j+1})} + \|p_j\|_{L^2(0,t;H^{l_j+1})}.$$

In addition,

$$\begin{aligned}\sum_{j=1}^{A}\|p_j - p_{j,h}\|_{L^2(0,t;H^1)} \lesssim E_0^h + h^{l+1}\left(\|u\|_{L^1(0,t;H^{l+2})} + \|p_0\|_{L^1(0,t;H^{l+1})}\right) \\ + \sum_{j=1}^{A} h^{l_j}\|p_j\|_{L^2(0,t;H^{l_j+1})} + h^{l_j+1}\left(\|p_j\|_{L^1(0,t;H^{l_j+1})} + \|\dot{p_j}, p_j\|_{L^2(0,t;H^{l_j+1})}\right)\end{aligned} \qquad \text{(I.4.17)}$$

and

$$\|p_0(t) - p_{0,h}(t)\| \lesssim h^{l+1}(\|p_0(t)\|_{H^{l+1}} + \|u(t)\|_{H^{l+2}}) + \|\varepsilon(e_u^h(t))\|_{2\mu} \qquad \text{(I.4.18)}$$

hold.

Proof. Let (u, p), (u_h, p_h) and (e_u, e_p) be as stated. By the triangle inequality, the definition of e_u^h, Korn's inequality, and (I.4.5) for any $t \in (0, T]$, we have that

$$\begin{aligned}\|u(t) - u_h(t)\|_{H^1} &\leq \|u(t) - \Pi_h^V u(t)\|_{H^1} + \|\Pi_h^V u(t) - u_h(t)\|_{H^1} \\ &\lesssim h^{l+1}\|u(t)\|_{H^{l+2}} + \|\varepsilon(e_u^h(t))\|_{2\mu},\end{aligned}$$

with inequality constant depending on Ω and μ. Further, Proposition I.4.1 gives for any $t \in (0, T]$ that

$$\|\varepsilon(e_u^h(t))\|_{2\mu} \lesssim E_0^h + \int_0^t \|\alpha \cdot e_p^I\|_{\lambda^{-1}}\,\mathrm{d}s + \left(\int_0^t \sum_{j=1}^{A}\|c_j \dot{e}_{p_j}^I + S_j(e_p^I)\|^2\,\mathrm{d}s\right)^{\frac{1}{2}}, \qquad \text{(I.4.19)}$$

where E_0^h is defined by (I.4.11). Applying (I.4.5) and (I.4.7), we note that for any $t \in (0, T]$

$$\|\alpha \cdot e_p^I(t)\|_{\lambda^{-1}} \lesssim h^{l+1}\left(\|u(t)\|_{H^{l+2}} + \|p_0(t)\|_{H^{l+1}}\right) + \sum_{j=1}^{A} h^{l_j+1}\|p_j(t)\|_{H^{l_j+1}}. \qquad \text{(I.4.20)}$$

Similarly, by (I.4.7) and the definition of S_j, we have that

$$\sum_{j=1}^{A} \|c_j \dot{e}^I_{p_j}(t) + S_j(e^I_p(t))\| \lesssim \sum_{j=1}^{A} h^{l_j+1}\|\dot{p}_j(t)\|_{H^{l_j+1}} + h^{l_j+1}\|p_j(t)\|_{H^{l_j+1}}. \quad \text{(I.4.21)}$$

Combining the above estimates and rearranging terms yield (I.4.16).

Turning to the pressures p_j, analogously using the triangle inequality, (I.4.6), the Poincaré inequality, and the assumptions on K_j, we have for any $t \in (0, T]$ and any $j = 1, \dots, A$ that

$$\begin{aligned} \|p_j - p_{j,h}\|_{L^2(0,t;H^1)} &\leq \|p_j - \Pi_h^{Q_j} p_j\|_{L^2(0,t;H^1)} + \|\Pi_h^{Q_j} p_j - p_{j,h}\|_{L^2(0,t;H^1)} \\ &\lesssim h^{l_j}\|p_j\|_{L^2(0,t;H^{l_j+1})} + \left(\int_0^t \|\nabla e^h_{p_j}(s)\|^2_{K_j}\,\mathrm{d}s\right)^{\frac{1}{2}}, \end{aligned}$$

where the constant in the second inequality depends on Ω and the lower bound on K_j. Using Proposition I.4.1 together with (I.4.20) and (I.4.21), we thus obtain the estimate given by (I.4.17).

Finally, (I.4.18) follows from

$$\|p_0(t) - p_{0,h}(t)\| \leq \|p_0(t) - \Pi_h^{Q_0} p_0(t)\| + \|\Pi_h^{Q_0} p_0(t) - p_{0,h}(t)\|,$$

(I.4.5), and (I.4.12). ■

Remark I.4.3. *We remark that the estimates of Theorem I.3.3, Proposition I.4.1, and Theorem I.4.2 all hold uniformly as $c_j \to 0$, including in the case $c_j = 0$, for any $j = 1, \dots, A$.*

Theorem I.4.2 above provides an optimal estimate for p_j in the $L^\infty(0,t;H^1)$-norm for $j = 1, \dots, A$. Moreover, Proposition I.4.1 also yields an optimal estimate for p_j in the $L^\infty(0,t;L^2)$-norm for $j = 1, \dots, A$, as summarized in Proposition I.4.4 below.

Proposition I.4.4. *Let (u, p), (u_h, p_h), (e_u, e_p) be as in Theorem I.4.2 and let $c_j > 0$ for $j = 1, \dots, A$. Then, the following estimate holds for all $t \in (0, T]$ with implicit constant independent of h, T, λ and $\xi_{j \leftarrow i} \geq 0$ for any $i, j = 1, \dots, A$:*

$$\begin{aligned} &\sum_{j=1}^{A} \|e_{p_j}(t)\| \lesssim E_0^h + h^{l+1}\left(\|u\|_{L^1(0,t;H^{l+2})} + \|p_0\|_{L^1(0,t;H^{l+1})}\right) \\ &+ \sum_{j=1}^{A} h^{l_j+1}\left(\|p_j\|_{H^{l_j+1}} + \|p_j\|_{L^1(0,t;H^{l_j+1})} + \|p_j\|_{L^2(0,t;H^{l_j+1})} + \|\dot{p}_j\|_{L^2(0,t;H^{l_j+1})}\right) \end{aligned} \quad \text{(I.4.22)}$$

with E_0^h in (I.4.11).

Proof. Using the triangle inequality and (I.4.7), we find that

$$\sum_{j=1}^{A} \|e_{p_j}\| \leq \sum_{j=1}^{A} \|e^I_{p_j}\| + \|e^h_{p_j}\| \lesssim \sum_{j=1}^{A} h^{l_j+1} \|p_j\|_{H^{l_j+1}} + \|e^h_{p_j}\|. \qquad \text{(I.4.23)}$$

Further, using Proposition I.4.1 and the assumption that $c_j > 0$ for all j, (I.4.20), and (I.4.21), we obtain (I.4.22). ■

I.5 Numerical convergence experiments

In this section, we present a set of numerical examples to illustrate the theoretical results presented. In particular, we examine the convergence of the numerical approximations for test cases with smooth solutions. All numerical simulations in this section and in the subsequent Section I.6 were run using the FEniCS finite element software [Aln+15] (version 2018.1+), and the simulation and post-processing code is openly available [PR18].

I.5.1 Convergence in the nearly incompressible case

We consider the manufactured solution test case introduced in Example I.1.1. As before, we consider a series of uniform meshes of the computational domain. The coarsest mesh size H corresponds to a uniform mesh constructed by dividing the unit square into 4×4 squares and dividing each square by a diagonal.

We let $V_h \times Q_h$ be the lowest-order Taylor-Hood-type elements, as defined by (I.4.4) with $l = 1$ and $l_j = 1$ for $j = 1, \dots, A$, for the semi-discrete total pressure variational formulation (I.4.1). For this experiment, we used a Crank-Nicolson discretization in time with time step size $\Delta t = 0.125$ and $T = 0.5$. Since the exact solutions are linear in time, we expected this choice of temporal discretization to be exact. Indeed, we tested with multiple time step sizes and found that the errors did not depend on the time step size.

We computed the approximation error of $u_h(T)$ and $p_h(T)$ in the L^2 and H^1-norms. The resulting errors for u_h, $p_{0,h}$, and $p_{1,h}$ are presented in Table I.2, together with computed convergence rates. The errors and convergence rates of $p_{2,h}$ were comparable and analogous to those of $p_{1,h}$ and, for this reason, not reported here.

From Theorem I.4.2 and Proposition I.4.4, we expect second order convergence (with decreasing mesh size h) for $u(T)$ in the H^1-norm, second order convergence for $p_0(T)$ in the L^2-norm, first order convergence for $p_j(T)$ in the H^1-norm and second order convergence for $p_j(T)$ in the L^2-norm (since $c_j > 0$) for $j = 1, \dots, A$. The numerically computed errors are in agreement with these theoretical results. In particular, we recover the optimal convergence rates of 2 for u_h in the H^1-norm, 2 for p_j in the L^2-norm and 1 for p_j in the H^1-norm.

Additionally, we observe that we recover the optimal convergence rate of 3 for $u_h(T)$ in the L^2-norm for this test case. Further investigations indicate that this does not hold for general ν: with $\nu = 0.4, 0.2$, the convergence rate for

h	$\Vert u(T) - u_h(T)\Vert$	Rate	$\Vert u(T) - u_h(T)\Vert_{H^1}$	Rate
H	3.13×10^{-2}		7.28×10^{-1}	
$H/2$	3.64×10^{-3}	3.11	1.98×10^{-1}	1.88
$H/4$	4.35×10^{-4}	3.06	5.06×10^{-2}	1.96
$H/8$	5.36×10^{-5}	3.02	1.27×10^{-2}	1.99
$H/16$	6.67×10^{-6}	3.01	3.19×10^{-3}	2.00
Optimal		3		2

h	$\Vert p_1(T) - p_{1,h}(T)\Vert$	Rate	$\Vert p_1(T) - p_{1,h}(T)\Vert_{H^1}$	Rate
H	3.69×10^{-2}		4.21×10^{-1}	
$H/2$	9.57×10^{-3}	1.92	2.16×10^{-1}	0.96
$H/4$	2.47×10^{-3}	1.98	1.09×10^{-1}	0.99
$H/8$	6.21×10^{-4}	1.99	5.45×10^{-2}	1.00
$H/16$	1.55×10^{-4}	2.00	2.73×10^{-2}	1.00
Optimal		2		1

h	$\Vert p_0(T) - p_{0,h}(T)\Vert$	Rate
H	1.42×10^{-1}	
$H/2$	3.10×10^{-2}	2.19
$H/4$	7.56×10^{-3}	2.04
$H/8$	1.88×10^{-3}	2.01
$H/16$	4.70×10^{-4}	2.00
Optimal		2

Table I.2: Approximation errors and convergence rates for the total pressure-based mixed finite element discretization for the smooth manufactured test case for a nearly incompressible material introduced in Example I.1.1. We observe that the optimal convergence is restored for the total pressure-based scheme. This is in contrast to the sub-optimal rates observed with the standard scheme (cf. Table I.1). The coarsest mesh size H corresponds to the mesh-size of a uniform mesh constructed by dividing the unit square into 4×4 squares and dividing each square by a diagonal.

$u_h(T)$ in the L^2-norm is reduced to between 2 and 3, cf. Table I.3a– I.3b. We performed simulation with $\nu = 0.3, 0.1$ and the results are analogous to the ones for $\nu = 0.4, 0.2$ and therefore are not reported here. No asymptotic behaviour is observed.

I.5.2 Convergence in the vanishing storage coefficient case

We also considered the same test case, total-pressure-based discretization, and set-up as described in Section I.5.1, but now with $c_j = 0$ for $j = 1, 2$. The

h	$\|u(T) - u_h(T)\|$	Rate	$\|u(T) - u_h(T)\|_{H^1}$	Rate
H	3.12×10^{-2}		7.25×10^{-1}	
$H/2$	3.86×10^{-3}	3.02	1.98×10^{-1}	1.87
$H/4$	5.47×10^{-4}	2.82	5.08×10^{-2}	1.96
$H/8$	9.90×10^{-5}	2.47	1.28×10^{-2}	1.99
$H/16$	2.19×10^{-5}	2.18	3.20×10^{-3}	2.00

(a) $\nu = 0.4$

h	$\|u(T) - u_h(T)\|$	Rate	$\|u(T) - u_h(T)\|_{H^1}$	Rate
H	3.19×10^{-2}		7.33×10^{-1}	
$H/2$	4.24×10^{-3}	2.91	2.01×10^{-1}	1.87
$H/4$	6.96×10^{-4}	2.61	5.15×10^{-2}	1.96
$H/8$	1.46×10^{-4}	2.25	1.30×10^{-2}	1.99
$H/16$	3.46×10^{-5}	2.08	3.24×10^{-3}	2.00

(b) $\nu = 0.2$

Table I.3: Displacement approximation errors and convergence rates for the total pressure-based mixed finite element discretization for the smooth manufactured test case introduced in Example I.1.1 but with $\nu = 0.4, 0.2$. The coarsest mesh size H corresponds to a uniform mesh constructed by dividing the unit square into 4×4 squares and dividing each square by a diagonal. We note that the third order convergence rate for $u_h(T)$ in the L^2-norm observed in Table I.3a–I.3b is reduced to order $2 - 3$ in this case with $\nu = 0.4, 0.2$.

corresponding errors are presented in Table I.4. We note that we observe the same optimal convergence rates as before for this case with $c_j = 0$.

I.5.3 Convergence of the discretization error

Proposition I.4.1 indicates superconvergence of the discretization errors e_u^h and $e_{p_j}^h$. In particular, this result predicts that for the lowest-order Taylor-Hood-type elements, we expect to observe second order convergence for the discretization error of p_j in the $L^2(0, T; H^1)$-norm. To examine this numerically, we consider the same test case, total-pressure-based discretization, and set-up as described in Section I.5.1, but now compute the error between the elliptic interpolants and the finite element approximation. The results are given in Table I.5 for p_1. The numerical results were entirely analogous for p_2 and therefore not shown. We indeed observe the second order convergence of $e_{p_j}^h(T)$ (for $j = 1, 2$) in the H^1-norm as indicated by Proposition I.4.1.

h	$\|u(T) - u_h(T)\|$	Rate	$\|u(T) - u_h(T)\|_{H^1}$	Rate
H	3.13×10^{-2}		7.28×10^{-1}	
$H/2$	3.64×10^{-3}	3.11	1.98×10^{-1}	1.88
$H/4$	4.35×10^{-4}	3.06	5.06×10^{-2}	1.96
$H/8$	5.36×10^{-5}	3.02	1.27×10^{-2}	1.99
$H/16$	6.67×10^{-6}	3.01	3.19×10^{-3}	2.00
Optimal		3		2

h	$\|p_1(T) - p_{1,h}(T)\|$	Rate	$\|p_1(T) - p_{1,h}(T)\|_{H^1}$	Rate
H	3.95×10^{-2}		4.21×10^{-1}	
$H/2$	1.06×10^{-2}	1.90	2.16×10^{-1}	0.96
$H/4$	2.69×10^{-3}	1.97	1.09×10^{-1}	0.99
$H/8$	6.75×10^{-4}	1.99	5.45×10^{-2}	1.00
$H/16$	1.69×10^{-4}	2.00	2.73×10^{-2}	1.00
Optimal		2		1

h	$\|p_0(T) - p_{0,h}(T)\|$	Rate
H	1.46×10^{-1}	
$H/2$	3.25×10^{-2}	2.17
$H/4$	7.97×10^{-3}	2.03
$H/8$	1.99×10^{-3}	2.00
$H/16$	4.96×10^{-4}	2.00
Optimal		2

Table I.4: Approximation errors and convergence rates for the total pressure-based mixed finite element discretization for the smooth manufactured test case introduced in Example I.1.1 but with vanishing storage coefficients ($c_j = 0$ for $j = 1, 2$). We observe the optimal convergence also for this set of parameter values. The coarsest mesh size H corresponds to a uniform mesh constructed by dividing the unit square into 4×4 squares and dividing each square by a diagonal.

h	$\|\Pi_h^1 p_1(T) - p_{1,h}(T)\|$	Rate	$\|\Pi_h^1 p_1(T) - p_{1,h}(T)\|_{H^1}$	Rate
H	2.98×10^{-3}		1.46×10^{-2}	
$H/2$	9.12×10^{-4}	1.71	4.25×10^{-2}	1.78
$H/4$	2.40×10^{-4}	1.92	1.11×10^{-2}	1.94
$H/8$	6.09×10^{-5}	1.98	2.79×10^{-2}	1.99
$H/16$	1.53×10^{-5}	2.00	6.99×10^{-2}	2.00
Theoretical		2		2

Table I.5: Discretization errors and convergence rates for p_1 for the total pressure-based mixed finite element discretization for the smooth manufactured test case for a nearly incompressible material introduced in Example I.1.1. We indeed observe the higher (second) order convergence of $e_{p_1}^h(T)$ in the H^1-norm as indicated by Proposition I.4.1. The coarsest mesh size H corresponds to a uniform mesh constructed by dividing the unit square into 4×4 squares and dividing each square by a diagonal.

I.6 Simulating fluid flow and displacement in a human brain using a 4-network model

In this section, we consider a variant of the 4-network model presented in [TV11] defined over a human brain mesh with physiologically inspired parameters and boundary conditions. In particular, we consider the MPET equations (I.1.1) with $A = 4$. The original 4 networks of [TV11] represent (1) interstitial fluid-filled extracellular spaces, (2) arteries, (3) veins and (4) capillaries. In view of recent findings [Abb+18] however, we conjecture that it may be more physiologically interesting to interpret the extracellular compartment as a paravascular network.

The computational domain is defined by Version 2 of the Colin 27 Adult Brain Atlas FEM mesh [Fan10], in particular a coarsened version of this mesh with 99 605 cells and 29 037 vertices, and is illustrated in Figure I.1 (left). The domain boundary consists of the outer surface of the brain, referred to below as the *skull*, and of inner convexities, referred to as the *ventricles*, cf. Figure I.1 (right). We selected three points in the domain $x_0 = (89.9, 108.9, 82.3)$ (center), $x_1 = (102.2, 139.3, 82.3)$ (point in the central z-plane), and $x_2 = (110.7, 108.9, 98.5)$ (point in the central y-plane). The relative locations of these points within the domain are also illustrated in Figure I.1 (left).

We consider the following set of boundary conditions for the system for all $t \in (0, T)$. All boundary pressure values are given in mmHg below, noting that 1 mmHg $\approx$ 133.32 Pa. We assume that the displacement is fixed on the outer

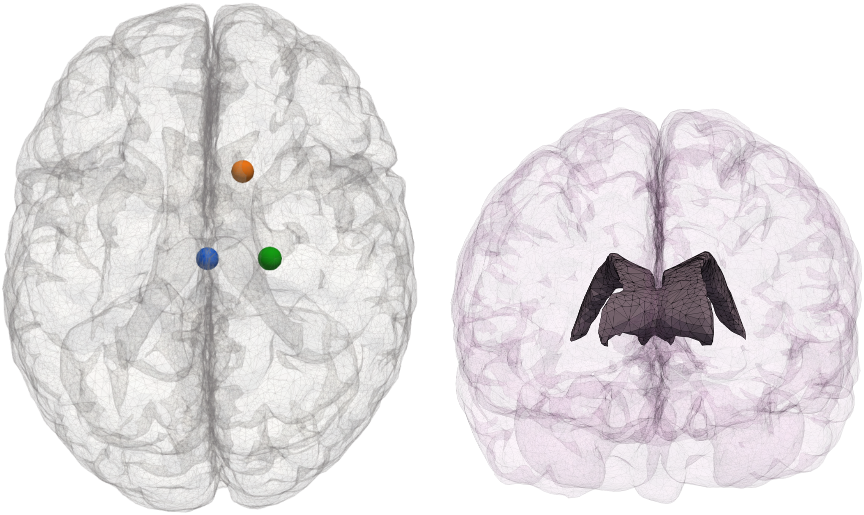

Figure I.1: Left: The human brain computational mesh used in Section I.6 with 99 605 cells and 29 037 vertices. View from top i.e. along the negative z-axis. The points x_0 (blue), x_1 (orange), x_2 (green) are marked with spheres. Right: The inner (ventricular) boundaries of the computational mesh. View from front i.e. along negative y-axis.

boundary and prescribe a total stress on the inner boundary:

$$u = 0 \quad \text{on skull}, \quad (C\varepsilon(u) - \textstyle\sum_{j=1}^{4} \alpha_j p_j I) \cdot n = s\, n \quad \text{on ventricles},$$

where n is the outward boundary normal and s is defined as

$$s = -\sum_{j=1}^{4} \alpha_j \tilde{p}_j,$$

where $\tilde{p}_j$ for $j = 1, \dots, 4$ are given below. We assume that the fluid in network 1 is in direct communication with the surrounding cerebrospinal fluid, and that a cerebrospinal fluid pressure is prescribed. In particular, we assume that the cerebrospinal fluid pressure pulsates around a baseline pressure of 5 (mmHg) with a peak transmantle pressure difference magnitude of $\delta = 0.012$ (mmHg):

$$p_1 = 5 + 2\sin(2\pi t) \quad \text{on skull}, \quad p_1 = 5 + (2 + \delta)\sin(2\pi t) \equiv \tilde{p}_1 \quad \text{on ventricles}.$$

We assume that a pulsating arterial blood pressure is prescribed at the outer boundary, while on the inner boundaries, we assume no arterial flux:

$$p_2 = 70 + 10\sin(2\pi t) \equiv \tilde{p}_2 \quad \text{on skull}, \quad \nabla p_2 \cdot n = 0 \quad \text{on ventricles}.$$

For the venous compartment, we assume that a constant pressure is prescribed at both boundaries:

$$p_3 = 6 \equiv \tilde{p}_3 \quad \text{on skull and ventricles}.$$

Symbol	Value(s)	Units	Reference
ν	0.4999		Comparable with [Nag+87]
E	1500	Pa	Comparable with [Bud+15]
c_1	3.9×10^{-4}	Pa^{-1}	[Guo+18, Table 2]
c_2, c_4	2.9×10^{-4}	Pa^{-1}	[Guo+18, Table 2]
c_3	1.5×10^{-5}	Pa^{-1}	[Guo+18, Table 2]
α_1	0.49		[Guo+18, Table 2]
α_2, α_4	0.25		[Guo+18, Table 2]
α_3	0.01		[Guo+18, Table 2]
K_1	$1.57 \cdot 10^{-5}$	$\mathrm{mm}^2\ \mathrm{Pa}^{-1}\ \mathrm{s}^{-1}$	[Var+16, Table 1]
$K_2, K_3, K_4,$	$3.75 \cdot 10^{-2}$	$\mathrm{mm}^2\ \mathrm{Pa}^{-1}\ \mathrm{s}^{-1}$	[Var+16, Table 1]
$\xi_{2\leftarrow 4}, \xi_{4\leftarrow 3}, \xi_{4\leftarrow 1}, \xi_{1\leftarrow 3}$	1.0×10^{-6}	$\mathrm{Pa}^{-1}\ \mathrm{s}^{-1}$	Comparable with [Mic+13]
$\xi_{1\leftarrow 2}, \xi_{2\leftarrow 3}$	0.0	$\mathrm{Pa}^{-1}\ \mathrm{s}^{-1}$	[Var+16]

Table I.6: Material parameters used for the multiple network poroelasticity equations (I.1.1) with $A = 4$ networks for the numerical experiments in Section I.6. We remark that a wide range of parameter values can be found in the literature and the ones used here represents one sample set of representative values.

Finally, for the capillary compartment, we assume no flux at both boundaries:

$$\nabla p_4 \cdot n = 0 \quad \text{on skull and ventricles.}$$

We consider the following initial conditions:

$$u = 0, \quad p_1 = 5, \quad p_2 = 70, \quad p_3 = 6, \quad p_4 = (p_2 + p_3)/2 \equiv \tilde{p}_4,$$

and material parameters as reported in Table I.6.

We computed the resulting solutions using the total pressure mixed finite element formulation with the lowest order Taylor-Hood type elements ($l = 1$ and $l_j = 1$ for $j = 1, \dots, 4$ in (I.4.4)), a Crank-Nicolson type discretization in time with time step $\Delta t = 0.0125$ (s) over the time interval $(0.0, 3.0)$ (s). The linear systems of equations were solved using a direct solver (MUMPS). For comparison, we also computed solutions with a standard mixed finite element formulation (as described and used in Example I.1.1) and otherwise the same numerical set-up. The number of degrees of freedom is 666198 for the standard formulation and 695235 for the total pressure formulation. The numerical results using the total pressure formulation are presented in Figures I.2 and I.3. In particular, snapshots of the displacement and network pressures at peak arterial

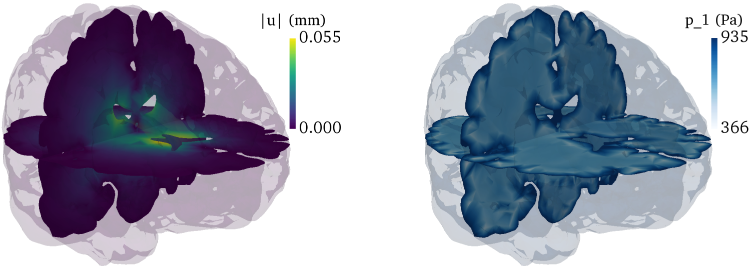

(a) Displacement magnitude $|u(\bar{t})|$ (b) Extracellular pressure $p_1(\bar{t})$

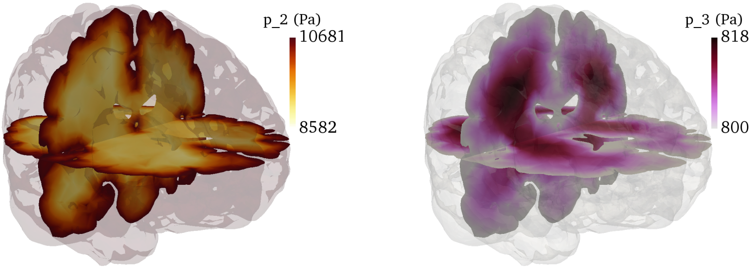

(c) Arterial pressure $p_2(\bar{t})$ (d) Venous pressure $p_3(\bar{t})$

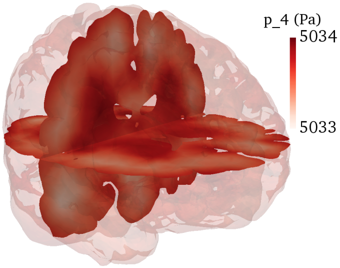

(e) Capillary pressure $p_4(\bar{t})$

Figure I.2: Results of numerical experiment described in Section I.6 using the total pressure formulation. Plots show slices of computed quantities at $\bar{t} = 2.25$ (s) corresponding to the peak arterial inflow in the 2nd cycle. From left to right and top to bottom: (a) displacement magnitude $|u|$, (b) extracellular pressure p_1, (c) arterial blood pressure p_2, (d) venous blood pressure p_3 and (e) capillary blood pressure p_4.

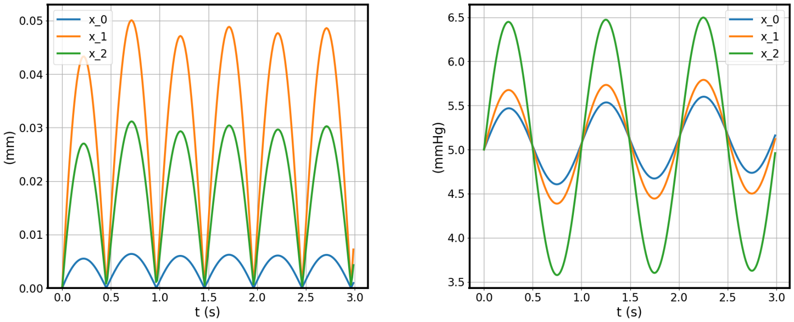

(a) Displacement magnitude $|u(x_i)|$ (b) Extracellular pressure $p_1(x_i)$

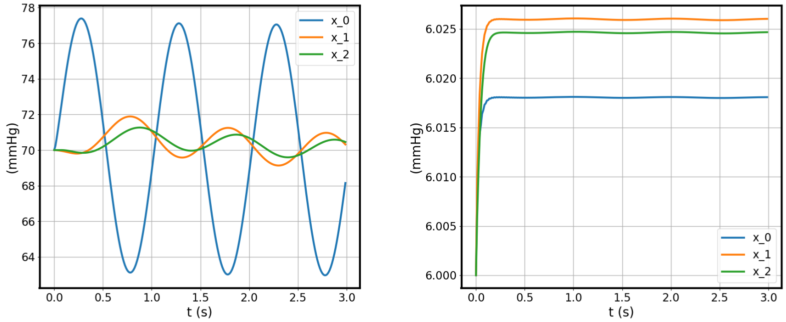

(c) Arterial pressure $p_2(x_i)$ (d) Venous pressure $p_3(x_i)$

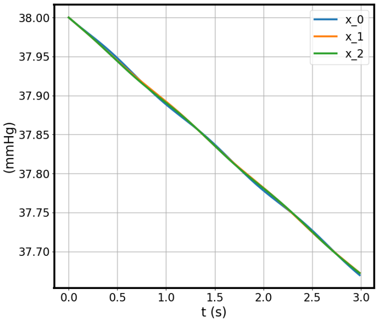

(e) Capillary pressure $p_4(x_i)$

Figure I.3: Results of numerical experiment described in Section I.6 using the total pressure formulation. Plots show computed quantities over time $t \in (0.0, 3.0)$ for a set of three points x_0, x_1, x_2. See Figure I.1 for the location and precise coordinates of the points x_i. From left to right and top to bottom: (a) displacement magnitude $|u|$, (b) extracellular pressure p_1, (c) arterial blood pressure p_2, (d) venous blood pressure p_3 and (e) capillary blood pressure p_4.

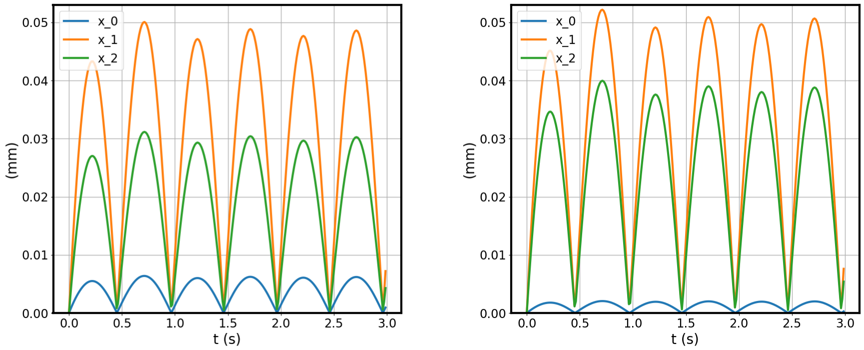

(a) Total pressure formulation

(b) 'Standard' formulation

Figure I.4: Comparison of displacements computed using the standard and total pressure formulation (cf. Section I.6). Plots of displacement magnitude $|u(x_i, t)|$ versus time t, for a set of points x_0, x_1, x_2 (see Figure I.1 for the location and precise coordinates of the points x_i): (a) Total-pressure mixed finite element formulation, (b) Standard mixed finite element formulation (cf. Example I.1.1). The computed displacements clearly differ between the two solution methods.

inflow in the 3rd cycle ($t = 2.25$ (s)) are presented in Figure I.2. Plots of the displacement magnitude and network pressures in a set of points versus time are presented in Figure I.3.

We also compared the solutions computed using the total pressure and standard mixed finite element formulation. Plots of the displacement magnitude in a set of points over time are presented in Figure I.4. We clearly observe that the computed displacements using the two formulations differ. For instance, the displacement magnitude in the point x_0 computed using the standard formulation is less than half the magnitude computed using the total pressure formulation. We also visually compared the pressures computed using the two formulations and found only minimal differences for this test case (data not shown for the standard formulation).

I.7 Conclusions

In this paper, we have presented a new mixed finite element formulation for the quasi-static multiple-network poroelasticity equations. Our formulation introduces a single additional scalar field unknown, the total pressure. We prove, via energy and semi-discrete *a priori* error estimates, that this formulation is robust in the limits of incompressibility ($\lambda \to \infty$) and vanishing storage coefficients ($c_j \to 0$), in contrast to standard formulations. Finally, numerical experiments support the theoretical results. For the numerical experiments presented here, we have used direct linear solvers. In future work, we will address iterative solvers and preconditioning of the MPET equations.

References

[Abb+18] Abbott, N. J. et al. “The role of brain barriers in fluid movement in the CNS: is there a "glymphatic" system?” In: *Acta Neuropathol.* (2018), pp. 1–21.

[Agu+08] Aguilar, G. et al. “Numerical stabilization of Biot’s consolidation model by a perturbation on the flow equation”. In: *Inter. J. Numer. Meth. Eng.* vol. 75, no. 11 (2008), pp. 1282–1300.

[Aln+15] Alnæs, M. et al. “The FEniCS project version 1.5”. In: *Archive of Numerical Software* vol. 3, no. 100 (2015), pp. 9–23.

[Ber+15] Berger, L. et al. “Stabilized lowest-order finite element approximation for linear three-field poroelasticity”. In: *SIAM J. Sci. Comp.* vol. 37, no. 5 (2015), A2222–A2245.

[BF91] Brezzi, F. and Falk, R. S. “Stability of higher-order Hood–Taylor methods”. In: *SIAM J. Numer. Anal.* vol. 28, no. 3 (1991), pp. 581–590.

[Bof94] Boffi, D. “Stability of higher order triangular Hood-Taylor methods for the stationary Stokes equations”. In: *Math. Models Methods Appl. Sci.* vol. 4, no. 2 (1994), pp. 223–235.

[Bof97] Boffi, D. “Three-dimensional finite element methods for the Stokes problem”. In: *SIAM J. Numer. Anal.* vol. 34, no. 2 (1997), pp. 664–670.

[BP79] Bercovier, M. and Pironneau, O. “Error estimates for finite element method solution of the Stokes problem in the primitive variables”. In: *Numer. Math.* vol. 33, no. 2 (1979), pp. 211–224.

[Bra01] Braess, D. *Finite elements: Theory, fast solvers, and applications in solid mechanics (2nd edition)*. Cambridge University Press, 2001.

[Bre74] Brezzi, F. “On the existence, uniqueness and approximation of saddle-point problems arising from Lagrangian multipliers”. In: *Rev. Française Automat. Informat. Recherche Opérationnelle Sér. Rouge* vol. 8, no. R-2 (1974), pp. 129–151.

[BRK17] Bause, M., Radu, F., and Köcher, U. “Space–time finite element approximation of the Biot poroelasticity system with iterative coupling”. In: *Comput. Methods in Appl. Mech. Eng.* vol. 320 (2017), pp. 745–768.

[BS08] Brenner, S. C. and Scott, L. R. *The Mathematical Theory of Finite Element Methods.* Third. Springer, 2008, pp. 245–263.

[Bud+15] Budday, S. et al. “Mechanical properties of gray and white matter brain tissue by indentation”. In: *J. Mech. Behav. Biomed. Mater.* vol. 46 (2015), pp. 318–330.

[Eva98] Evans, L. C. *Partial differential equations.* Vol. 19. Graduate Studies in Mathematics. Providence, RI: American Mathematical Society, 1998, pp. xviii+662.

[Fan10] Fang, Q. “Mesh-based Monte Carlo method using fast ray-tracing in Plücker coordinates”. In: *Biomed. Opt. Express* vol. 1, no. 1 (2010), pp. 165–175.

[Guo+18] Guo, L. et al. “Subject-specific multi-poroelastic model for exploring the risk factors associated with the early stages of Alzheimer’s disease”. In: *Interface Focus* vol. 8, no. 1 (2018), p. 20170019.

[Hu+17] Hu, X. et al. “A nonconforming finite element method for the Biot’s consolidation model in poroelasticity”. In: *J. Comput. Appl. Math.* vol. 310 (2017), pp. 143–154.

[Ili+12] Iliff, J. J. et al. “A paravascular pathway facilitates CSF flow through the brain parenchyma and the clearance of interstitial solutes, including amyloid-β”. In: *Sci. Transl. Med.* vol. 4, no. 147 (2012), 147ra111.

[Jes+15] Jessen, N. A. et al. “The glymphatic system: a beginner’s guide”. In: *Neurochem. Res.* vol. 40, no. 12 (2015), pp. 2583–2599.

[KS05] Korsawe, J. and Starke, G. “A least-squares mixed finite element method for Biot’s consolidation problem in porous media”. In: *SIAM J. Numer. Anal.* vol. 43, no. 1 (2005), pp. 318–339.

[Lee16] Lee, J. J. “Robust error analysis of coupled mixed methods for Biot’s consolidation model”. In: *J. Sci. Comput.* vol. 69, no. 2 (2016), pp. 610–632.

[Lee17] Lee, J. J. “Robust three-field finite element methods for Biot’s consolidation model in poroelasticity”. In: *BIT* (Oct. 2017).

[LMW17] Lee, J. J., Mardal, K.-A., and Winther, R. “Parameter-Robust Discretization and Preconditioning of Biot’s Consolidation Model”. In: *SIAM J. Sci. Comp.* vol. 39, no. 1 (2017), A1–A24.

[Mic+13] Michler, C. et al. “A computationally efficient framework for the simulation of cardiac perfusion using a multi-compartment Darcy porous-media flow model”. In: *Int. J. Numer. Method Biomed. Eng.* vol. 29, no. 2 (2013), pp. 217–232.

[MTL96] Murad, M. A., Thomée, V., and Loula, A. F. “Asymptotic behavior of semidiscrete finite-element approximations of Biot’s consolidation problem”. In: *SIAM J. Numer. Anal.* vol. 33, no. 3 (1996), pp. 1065–1083.

[Nag+87] Nagashima, T. et al. “Biomechanics of hydrocephalus: a new theoretical model”. In: *Neurosurgery* vol. 21, no. 6 (1987), pp. 898–904.

[Nor+10] Nordbotten, J. M. et al. “A posteriori error estimates for approximate solutions of the Barenblatt-Biot poroelastic model”. In: *Comput. Methods Appl. Math.* vol. 10, no. 3 (2010), pp. 302–314.

[OR16] Oyarzúa, R. and Ruiz-Baier, R. “Locking-free finite element methods for poroelasticity”. In: *SIAM J. Numer. Anal.* vol. 54, no. 5 (2016), pp. 2951–2973.

[PR18] Piersanti, E. and Rognes, M. E. *Supplementary material (code) for A mixed finite element method for nearly incompressible multiple-network poroelasticity' by J. J. Lee, E. Piersanti, K.-A. Mardal and M. E. Rognes.* Apr. 2018.

[PW07] Phillips, P. J. and Wheeler, M. F. “A coupling of mixed and continuous Galerkin finite element methods for poroelasticity. I. The continuous in time case”. In: *Comput. Geosci.* vol. 11, no. 2 (2007), pp. 131–144.

[Rod+17] Rodrigo, C. et al. “New stabilized discretizations for poroelasticity and the Stokes' equations”. In: *arXiv preprint arXiv:1706.05169* (2017).

[Sho00] Showalter, R. E. “Diffusion in poro-elastic media”. In: *J. Math. Anal. Appl.* vol. 251, no. 1 (2000), pp. 310–340.

[SM02] Showalter, R. E. and Momken, B. “Single-phase flow in composite poroelastic media”. In: *Math. Methods Appl. Sci.* vol. 25, no. 2 (2002), pp. 115–139.

[TH73] Taylor, C. and Hood, P. “A numerical solution of the Navier-Stokes equations using the finite element technique”. In: *Comput. Fluids* vol. 1, no. 1 (1973), pp. 73–100.

[TV11] Tully, B. J. and Ventikos, Y. “Cerebral water transport using multiple-network poroelastic theory: application to normal pressure hydrocephalus”. In: *J. Fluid Mech.* vol. 667 (2011), pp. 188–215.

[Var+16] Vardakis, J. C. et al. “Investigating cerebral oedema using poroelasticity”. In: *Med. Eng. Phys.* vol. 38, no. 1 (2016), pp. 48–57.

[Yi14] Yi, S.-Y. “Convergence analysis of a new mixed finite element method for Biot's consolidation model”. In: *Numer. Methods Partial Differential Equations* vol. 30, no. 4 (2014), pp. 1189–1210.

[Yi17] Yi, S.-Y. “A Study of Two Modes of Locking in Poroelasticity”. In: *SIAM J. Numer. Anal.* vol. 55, no. 4 (2017), pp. 1915–1936.

[Yos80] Yosida, K. *Functional Analysis.* 6th. Springer Classics in Mathematics. Springer-Verlag, 1980.

Paper III

Parameter robust preconditioning by congruence for multiple-network poroelasticity

E. Piersanti, J. J. Lee, T. Thompson, K.-A. Mardal, M. E. Rognes.

Published in *SIAM Journal on Scientific Computing*, August 2021, volume 43, issue 4, DOI: 10.1137/20M1326751.

Abstract

The mechanical behaviour of a poroelastic medium permeated by multiple interacting fluid networks can be described by a system of time-dependent partial differential equations known as the multiple-network poroelasticity (MPET) equations or multi-porosity/multi-permeability systems. These equations generalize Biot's equations, which describe the mechanics of the one–network case. The efficient numerical solution of the MPET equations is challenging, in part due to the complexity of the system and in part due to the presence of interacting parameter regimes. In this paper, we present a new strategy for efficiently and robustly solving the MPET equations numerically. In particular, we discuss an approach to formulating finite element methods and associated preconditioners for the MPET equations based on simultaneous diagonalization of the element matrices. We demonstrate the technique for the MPT equations, with large exchange variability, and the MPET equations for a nearly incompressible medium with large exchange variability. The approach is based on designing transformations of variables that simultaneously diagonalize (by congruence) the equations' key operators and subsequently constructing parameter-robust block-diagonal preconditioners for the transformed system. The proposed approach is supported by theoretical considerations as well as by numerical results.

III.1 Introduction

In this paper, we consider the preconditioned iterative solution of finite element discretizations of the multiple-network poroelasticity (MPET) equations. These equations traditionally originate in geomechanics where they are also known under the term multi-porosity/multi-permeability systems [BER93]. The MPET equations generalize Biot's equations [Bio41] from the one network to the multiple network case, and multi-compartment Darcy (MPT) equations [Mic+13] from a porous (but rigid) to a poroelastic medium. Over the last decade, the MPT and MPET equations have seen a surge of interest in biology and physiology; e.g. to model perfusion in the heart [Lee+15; Mic+13], brain [Józ+], liver [BLR19], or in cancer [Shi+20], or to model the interaction between elastic deformation and fluid flow and transport in the brain [Cho+16; ES13; MP17; TV11; TV13; Var+16].

Concretely, the quasi–static MPET equations read as follows [BER93]: for a given number of networks $J \in \mathbb{N}$, find the displacement u and the network pressures p_j for $j = 1, \ldots, J$ such that

$$-\operatorname{div}(2\mu\varepsilon(u) + \lambda \operatorname{div} u\mathbb{I}) + \textstyle\sum_j \alpha_j \nabla p_j = f, \tag{III.1.1a}$$

$$s_j \dot{p}_j + \alpha_j \operatorname{div} \dot{u} - \operatorname{div} K_j \nabla p_j + \textstyle\sum_i \xi_{j \leftarrow i}(p_j - p_i) = g_j, \tag{III.1.1b}$$

where $u = u(x,t)$, $p_j = p_j(x,t)$ for $x \in \Omega \subset \mathbb{R}^d$ $(d = 1, 2, 3)$, $t \in (0, T]$, and $\mathbb{I}$ is the $d \times d$ identity matrix. Physically, the equations (III.1.1) describe a porous and elastic medium permeated by a number of fluid networks under the assumptions that the solid matrix can be modeled as isotropic and linearly elastic with Lamé constants $\mu > 0$ and $\lambda > 0$, and the transfer between the networks is regulated by the corresponding pressure differences with exchange coefficients $\xi_{j \leftarrow i} \geq 0$. For each network j, we define the Biot-Willis coefficient $\alpha_j \in (0, 1]$ such that $\sum_j \alpha_j \leq 1$, the storage coefficient $s_j > 0$, and the hydraulic conductivity tensor $K_j = \kappa_j/\nu_j > 0$ with κ_j and ν_j being the permeability and fluid viscosity, respectively. Moreover, ∇ denotes the column-wise gradient, ε is the symmetric gradient, div denotes the (row-wise) divergence the superposed dot denotes the time derivative(s), and I denotes the identity matrix. On the right hand side, f represents body forces and g_j sources (or sinks) in network j for $j = 1, \ldots, J$.

The MPT equations represents a reduced version of (III.1.1) that result from ignoring the elastic contribution of the solid matrix. These equations then read as follows: for a given number of networks $J \in \mathbb{N}$, find the network pressures p_j for $j = 1, \ldots, J$ such that

$$-\operatorname{div} K_j \nabla p_j + \textstyle\sum_{i=1}^{J} \xi_{j \leftarrow i}(p_j - p_i) = g_j, \tag{III.1.2}$$

where for $i, j = 1, \ldots, J$, $p_j = p_j(x)$ for $x \in \Omega \subset \mathbb{R}^d$ $(d = 1, 2, 3)$, the parameters K_j and $\xi_{j \leftarrow i}$ remain the hydraulic conductivity and exchange coefficients, respectively, and g_j again represents other sources (or sinks) in each network. The relative size of the conductivities K_j and the exchange coefficients $\xi_{j \leftarrow i}$ may vary tremendously in applications. Large parameter variation is certainly present in applied problems of a physiological nature; a selection of representative parameter values, from research literature, is given in Table III.1. Here, we see that the hydraulic conductivities span four orders of magnitude while the exchange coefficients span fourteen orders of magnitude. Hence, there is a need for preconditioners that are robust with respect to variations in parameters.

Parameter	Unit	Value	Reference
Hydraulic conductivities (K_j)	$\mathrm{mm}^2\ (\mathrm{kPa\ s})^{-1}$		
Brain gray matter		2.0×10^{-3}	[Stø+16]
Brain white matter		2.0×10^{-2}	[Stø+16]
Cardiac arteries		1.0	[Mic+13]
Cardiac capillaries		2.0	[Mic+13]
Cardiac veins		10.0	[Mic+13]
Brain vasculature		3.75×10^{1}	[Var+16]
Brain fluid exchange		1.57×10^{-2}	[Var+16]
Exchange coefficients ($\xi_{j \to i}$)	$(\mathrm{kPa\ s})^{-1}$		
Brain capillary-vasculature		1.5×10^{-16}	[Var+16]
Brain capillary-tissue fluid		2.0×10^{-16}	[Var+16]
Brain tissue fluid-veins		2.0×10^{-10}	[Var+16]
Cardiac capillary-arteries		2.0×10^{-2}	[Mic+13]
Cardiac capillary-veins		5.0×10^{-2}	[Mic+13]

Table III.1: Sample parameter values for hydraulic conductivities and exchange coefficients with reference to (III.1.1) and/or (III.1.2).

Physiological applications, in particular, can benefit from preconditioners which are robust with respect to K_j, $\xi_{j \leftarrow i}$ and λ as in (III.1.1) and (III.1.2).

With this in mind, parameter-robust numerical approximations and solution algorithms for (III.1.1) is currently an active research topic. In the nearly incompressible case $\lambda \gg 1$, the standard two-field variational formulation of (III.1.1) is not robust. To address this challenge, we introduced and analyzed a mixed finite element method for the MPET equations based on a total pressure formulation in [Lee+19]. We note that the total pressure in case of one network was presented in [LMW17; OR16]. Hong et al. [Hon+19] shortly thereafter extended the three-field formulation in [HK18] to parameter-robust MPET equations taking the displacement, the network fluid fluxes and the network pressures as unknowns. In fact, the approach of [Hon+19] is the first result advancing preconditioners which are robust with respect to every material and discretization parameter; including the network transfer terms we consider here. As an alternative to these fully coupled approaches a form of splitting schemes has been analyzed by Lee [Lee19]. Regarding the iterative solution and preconditioning of the fully coupled formulations, a robust preconditioner for Biot's equations (the case for $J = 1$) was presented by Lee et al. [LMW17]. Hong et al. [Hon+19] presented both theoretical results and numerical examples regarding parameter-robust preconditioners for the MPET equations with their extended three-field-type formulation. Hong et al. further developed parameter-robust solver algorithms, an iterative solver algorithm using the iterative coupling approach (cf. [MW13]) in [Hon+20a], and an Uzawa-type algorithm in [Hon+20b].

In this paper, we present a parameter-robust preconditioning approach for linear systems of equations resulting from a conforming finite element discretization of the total pressure variational formulation of the MPET equations. The main focus of this work is to achieve preconditioners which are robust for large ratios of exchange coefficients. The potential of *diagonalization by congruence* was also mentioned by Hong et al [Hon+19, Rmk. 6]. In this manuscript, we discuss diagonalization by congruence as a general method in the context of preconditioning the MPET equations. The key idea is, as introduced for the MPT equations in [PRM19], to design a parameter-dependent transformation of the pressure variables $p = (p_1, \ldots, p_J)$ into a set of transformed variables $\tilde{p}$. The transformation should be such that the originally coupled exchange operator decouples while the originally decoupled diffusion operator remains decoupled (i.e. remains diagonal). We will discuss this approach, and its associated matrix theory in detail. We illustrate the use of the method to construct parameter-robust preconditioners for both the MPT equations (Section III.3) and the MPET equations (Section III.4).

There are several notable differences between the approach of the current work and that of [Hon+19]. First, the formulation of [Hon+19] introduces $2J+1$ unknowns for a multiple poroelasticity system consisting of J fluid networks. Conversely, the total pressure formulation, which we use here, requires $J+2$ unknowns. Thus, our approach can confer a significant computational savings for applications where J is appreciably large. Second, the spatial discretization in [Hon+19] employs several $H(\mathrm{div})$ finite element spaces; as a result, multiple $H(\mathrm{div})$ preconditioners are needed for robust preconditioning. Conversely, we discretize by means of continuous Galerkin finite elements; as a result, block preconditioners can be constructed using typical preconditioners for second order elliptic operators. It should be noted, though, that our approach does not satisfy local mass conservation; the paradigm of [Hon+19] is locally mass conservative, due to the $H(\mathrm{div})$ elements, with the price being an increase in computational cost. Third, the preconditioning results of [Hon+19] are unequivocally robust for all parameter ranges; a first result of its kind for generalized poroelasticity. Conversely, our approach requires a slight restriction, in general, of the parameter ranges for the network storage coefficients; this restriction can be removed, however, for materials with non-degenerate storage coefficients satisfying $\lambda^{-1} \lesssim s_j$ (c.f. Remark III.4.4). Overall, if the number of networks is small, local mass conservation is important for the application, or if the material storage coefficients are degenerate then [Hon+19] is a strong option. Conversely, if local mass conservation is not a strict application concern and the network storage coefficients are not degenerate, our approach confers a significant computational advantage, over that of [Hon+19], when the number of fluid networks (J) is large.

This manuscript is organized as follows. We introduce notation and review relevant preconditioning and matrix theory in Section III.2. We briefly consider the reduced case of the MPT equations in Section III.3 before turning to the analysis of the preconditioner for the MPET equations in Section III.4. Finally, we present some conclusions and outlook in Section III.5.

III.2 Preliminaries

In Section III.2.2 we briefly review preconditioning of parameter-dependent systems and state a known result regarding simultaneous diagonalization by congruence. Notation for the remainder of the manuscript is discussed in Section III.2.1.

III.2.1 Notation

In the subsequent manuscript, we use the following notation. Let Ω be an open, bounded domain in $\mathbb{R}^d$, $d = 2, 3$, with Lipschitz polyhedral boundary $\partial\Omega$. We denote by $L^2(\Omega)$ the space of square integrable functions on Ω with inner product $\langle \cdot, \cdot \rangle$ and norm $\| \cdot \|$. We denote by $H^m(\Omega)$ the standard Sobolev space with norm $\|\cdot\|_{H^m}$ and semi-norm $|\cdot|_{H^m}$ for $m \geq 1$ and $H^m(\Omega; \mathbb{R}^d)$ the corresponding d-vector fields. We use $H_0^m(\Omega)$ to denote the subspace of $H^m(\Omega)$ with vanishing trace on the boundary of Ω. Let Γ be a subset of $\partial\Omega$ such that $\partial\Omega \setminus \Gamma$ has a positive $(d-1)$-dimensional Lebesgue measure. $H_\Gamma^m(\Omega)$ is the subspace of $H^m(\Omega)$ such that the elements in $H_\Gamma^m(\Omega)$ have vanishing trace on Γ. $H_\Gamma^m(\Omega; \mathbb{R}^d)$ is the subspace of $H^m(\Omega; \mathbb{R}^d)$ such that every v_j in $(v_1, \ldots, v_d) \in H^m(\Omega; \mathbb{R}^d)$ is an element in $H_\Gamma^m(\Omega)$. Throughout this paper we set Γ a fixed subset of $\partial\Omega$ satisfying the aforementioned assumption.

We introduce the parameter-dependent L^2-inner product and norm:

$$\|p\|_\beta^2 = \langle p, p \rangle_\beta = \langle \beta p, p \rangle$$

for $\beta \in L^\infty(\Omega)$, $\beta(x) > 0$, and $p \in L^2(\Omega)$ (and similarly for vector or tensor fields). The notation $\mathbb{I}$ will denote an identity $d \times d$ matrix while I_V will denote the identity operator on a Hilbert space V. To be self-contained we recall the Kronecker product of matrices. If A in $\mathbb{R}^{m \times n}$ and $B \in \mathbb{R}^{r \times s}$ are two real-valued matrices then $A \otimes B$ is the $mr \times ns$ matrix defined by multiplying each entry of A by the matrix B. That is,

$$A \otimes B = \begin{bmatrix} a_{11}B & a_{12}B & \ldots & a_{1n}B \\ a_{21}B & a_{22}B & \ldots & a_{2n}B \\ \vdots & \ddots & \ddots & \vdots \\ a_{m1}B & a_{m2}B & \ldots & a_{mn}B \end{bmatrix}. \tag{III.2.1}$$

We can consider its natural extension for a matrix A and a linear operator B. More specifically, if W is a Hilbert space, Q is the $n-$fold product $Q = W \times W \times \cdots \times W$, A is an $n \times n$ matrix, and B is a linear operator on W, then $A \otimes B$ is the linear operator on Q defined by (III.2.1).

Finally, we introduce a notation for uniform proportionality, used throughout the manuscript, as

$$X \lesssim Y.$$

That is, $X \lesssim Y$ implies the existence of some real constant $c_0 > 0$ such that $X \leq c_0 Y$; any relationship between c_0 and pertinent mathematical objects, such as the total number of porous media networks considered, will be specified.

III.2.2 Preconditioning of parameter-dependent systems

In this paper, we consider the preconditioning of discretizations of the systems (III.1.1) and (III.1.2) under large parameter variations. Therefore, we begin by summarizing core aspects of the theory of parameter-robust preconditioning as presented in [MR11]. We will apply this theory for formulations of the MPT equations (III.1.2) and MPET equations (III.1.1) in the subsequent sections.

Let X be a separable, real Hilbert space with inner product $\langle \cdot, \cdot \rangle_X$, norm $\|\cdot\|_X$ and dual space X^*. Let $\mathcal{A} : X \to X$ be an invertible, symmetric isomorphism on X such that $\mathcal{A} \in \mathcal{L}(X, X^*)$ where $\mathcal{L}(X, X^*)$ is the set of bounded linear operators mapping X to its dual. Given $f \in X^*$ consider the problem of finding $x \in X$ such that

$$\mathcal{A}x = f. \tag{III.2.2}$$

The preconditioned problem reads as follows

$$\mathcal{B}\mathcal{A}x = \mathcal{B}f, \tag{III.2.3}$$

where $\mathcal{B} \in \mathcal{L}(X^*, X)$ is a symmetric isomorphism defining the preconditioner. The convergence rate of a Krylov space method for this problem can be bounded in terms of the condition number $\kappa(\mathcal{B}\mathcal{A})$ where

$$\kappa(\mathcal{B}\mathcal{A}) = \|\mathcal{B}\mathcal{A}\|_{\mathcal{L}(X,X)} \|(\mathcal{B}\mathcal{A})^{-1}\|_{\mathcal{L}(X,X)}.$$

Here, the operator norm $\|\mathcal{A}\|_{\mathcal{L}(X,X^*)}$ is defined by

$$\|\mathcal{A}\|_{\mathcal{L}(X,X^*)} = \sup_{x \in X} \frac{\|\mathcal{A}x\|_{X^*}}{\|x\|_X}. \tag{III.2.4}$$

Now, for a parameter ε (or more generally a set of parameters ε) consider the parameter-dependent operator $\mathcal{A}_\varepsilon$ and its preconditioner $\mathcal{B}_\varepsilon$. Assume that we can choose appropriate spaces X_ε and X_ε^* such that the norms

$$\|\mathcal{A}_\varepsilon\|_{\mathcal{L}(X_\varepsilon, X_\varepsilon^*)} \text{ and } \|\mathcal{A}_\varepsilon^{-1}\|_{\mathcal{L}(X_\varepsilon^*, X_\varepsilon)}$$

are bounded independently of ε. Similarly, we assume that we can find a preconditioner $\mathcal{B}_\varepsilon$ such that the norms $\|\mathcal{B}_\varepsilon\|_{\mathcal{L}(X_\varepsilon, X_\varepsilon^*)}$ and $\|\mathcal{B}_\varepsilon^{-1}\|_{\mathcal{L}(X_\varepsilon^*, X_\varepsilon)}$ are bounded independently of ε. Given these assumptions, the condition number $\kappa(\mathcal{B}_\varepsilon \mathcal{A}_\varepsilon)$ will be bounded independently of ε. We will refer to such a preconditioner as robust in (or with respect to) ε. We conclude this section with a change of variables result, recalled from basic matrix analysis [HJ90], that will prove effective in the sections that follow.

Lemma III.2.1 (Diagonalization by congruence). *Let W be a real Hilbert space and $Q = W \times W \times \cdots \times W$ be the n-fold direct product of W for a fixed $n \in \mathbb{N}$. Let $A : W \to W^*$, and $B : W \to W^*$ be linear operators. Suppose that $K, E \in \mathbb{R}^{n \times n}$ are symmetric matrices and that at least one of K or E is positive definite. Define the operators $S : Q \to Q^*$ and $T : Q \to Q^*$ by*

$$S = K \otimes A, \quad \textit{and} \quad T = E \otimes B,$$

where $\otimes$ is the Kronecker product. Consider the variational problem: given $f \in Q^*$ find $p = (p_1, p_2, \dots, p_n)^T \in Q$ such that

$$\langle Sp, q\rangle + \langle Tp, q\rangle = \langle f, q\rangle, \quad \forall\, q \in Q \tag{III.2.5}$$

where $\langle \cdot, \cdot\rangle$ is the duality pairing of Q^* and Q. Then there exists an invertible matrix $P \in \mathbb{R}^{n\times n}$ such that the above variational problem is equivalent to: find $\tilde{p} \in Q$ such that

$$\langle D_S\tilde{p}, q\rangle + \langle D_T\tilde{p}, q\rangle = \langle F, q\rangle, \quad \forall\, q \in Q, \tag{III.2.6}$$

where $F = (P^T \otimes I_{W^*})f$ for I_{W^*} the identity operator on W^*, and $D_S = \left(P^T KP\right) \otimes A$ and $D_T = \left(P^T EP\right) \otimes B$ are block diagonal linear operators from Q to Q^*.

Proof. Apply [HJ90, Theorem 4.5.17a-b p. 287] the hypotheses on the matrices K and E and properties of the tensor product; see Appendix III.A for detail. ■

III.3 Preconditioning the MPT equations via diagonalization

In this section, we present the method of simultaneous diagonalization by congruence, and demonstrate how the method can be applied to variational formulations and their associated preconditioners. Motivated by (III.1.1), we first consider the simpler MPT equations as in [PRM19]. The core idea is to reformulate the MPT equations using a change of pressure variables p. In particular, we aim to find a transformation of the variables $p \mapsto \tilde{p}$ such that the transformed system of pressure equations decouple. Here, we will consider a Hilbert space W and the J-fold product $Q = W \times W \times \cdots \times W$. Each pressure p_j, for $j = 1, 2, \dots, J$ satisfies $p_j \in W$ and we will write $p = (p_1, p_2, \dots, p_J) \in Q$. In the sections that follow, we briefly illustrate the core idea, formulation of the MPT equations and resulting preconditioner, and refer to [PRM19] for more details. This approach is then extended to the MPET equations in Section III.4.

III.3.1 The MPT equations in operator form

We consider the MPT equations as defined by (III.1.2). We further impose homogeneous Dirichlet boundary conditions for all pressures: $p_j = 0$ on $\partial\Omega$ for $1 \le j \le J$. Define $\xi_j = \sum_{i=1}^{J} \xi_{j\leftarrow i}$ for each $1 \le j \le J$. Let us define two $J \times J$ matrices:

$$K = \begin{pmatrix} K_1 & 0 & \cdots & 0 \\ 0 & K_2 & \cdots & 0 \\ \vdots & \vdots & \ddots & \vdots \\ 0 & 0 & \cdots & K_J \end{pmatrix}, \quad E = \begin{pmatrix} \xi_1 & -\xi_{1\leftarrow 2} & \cdots & -\xi_{1\leftarrow J} \\ -\xi_{1\leftarrow 2} & \xi_2 & \cdots & -\xi_{2\leftarrow J} \\ \vdots & \vdots & \ddots & \vdots \\ -\xi_{1\leftarrow J} & -\xi_{2\leftarrow J} & \cdots & \xi_J \end{pmatrix}. \tag{III.3.1}$$

The system (III.1.2) can be expressed in operator form as: given $g \in Q$ find $p \in Q$ satisfying

$$\mathcal{A}_{\mathrm{MPT}} p = g \quad \text{where} \quad \mathcal{A}_{\mathrm{MPT}} = -K \otimes \Delta + E \otimes I_W. \tag{III.3.2}$$

In the above, $-K \otimes \Delta : Q \to Q^*$ is the block diagonal operator such that its j-th block is given by the bilinear form $\langle K_j \nabla p_j, \nabla q_j \rangle$ for $p_j, q_j \in Q_j = W$, and $E \otimes I_W : Q \to Q^*$ is the block operator such that its (i,j)-block E_{ij} is defined by the bilinear forms

$$-\langle \xi_{i \leftarrow j} p_i, q_j \rangle \text{ if } i \neq j, \qquad \langle \xi_j p_j, p_j \rangle \text{ if } i = j.$$

We note that K is real, positive definite and diagonal (and thus invertible), and that E is real, symmetric and (weakly row) diagonally dominant by definition. In particular, E is symmetric positive semi-definite because of the identity

$$w E w^T = \sum_{1 \leq i,j \leq J} \xi_{i \leftarrow j} (w_i - w_j)^2, \tag{III.3.3}$$

for $w = (w_1, w_2, \dots, w_J)$ with the convention $\xi_{i \leftarrow i} = 0$. A naive block diagonal preconditioner $\mathcal{B}_{\mathrm{MPT}}$ can be constructed by taking the inverse of the diagonal blocks of $\mathcal{A}_{\mathrm{MPT}}$. However, as we demonstrated in [PRM19], the resulting preconditioner is not robust with respect to variations in the conductivity and exchange parameters. In fact, the condition numbers increased linearly with the ratio between the exchange and conductivity coefficients.

III.3.2 Diagonalizing the MPT equations by congruence

In this section we discuss a reformulation of the MPT equations which, in turn, leads directly to a parameter-robust preconditioner. Let $P \in \mathbb{R}^{J \times J}$ be an invertible linear transformation defining a change of variables and let $\tilde{p}$ and $\tilde{q}$ be the new set of variables such that

$$p = (P \otimes I_W)\, \tilde{p}, \quad q = (P \otimes I_W)\, \tilde{q}, \tag{III.3.4}$$

with $q = (q_1, q_2, \dots, q_J)$ and similarly for $\tilde{q}, \tilde{p}$. Since K and E are symmetric, we apply Lemma III.2.1, with $A = \Delta$ and $B = I_W$, to obtain a matrix, P, simultaneously diagonalizing K and E by congruence; that is, the equivalent operators $\left(P^T K P\right) \otimes \Delta$ and $\left(P^T E P\right) \otimes I_W$ are block diagonal. The resulting formulation (c.f. (III.2.6)) of the MPT equations reads as follows: find the transformed pressures $\tilde{p} = (\tilde{p}_1, \dots, \tilde{p}_J)$ such that, for a given $g \in Q$, we have the equality

$$\tilde{\mathcal{A}}_{\mathrm{MPT}} \tilde{p} = (-\tilde{K} \otimes \Delta + \tilde{E} \otimes I_W) \tilde{p} = \left(P^T \otimes I_W\right) g, \tag{III.3.5}$$

where $\tilde{K} = P^T K P$ and $\tilde{E} = P^T E P$ are diagonal with

$$\tilde{K} = \mathrm{diag}(\tilde{K}_1, \dots, \tilde{K}_J), \quad \tilde{E} = \mathrm{diag}(\tilde{\xi}_1, \dots, \tilde{\xi}_J). \tag{III.3.6}$$

III.3.3 Preconditioning the transformed MPT system

The parameter dependent norm, for the transformed system, can be immediately identified [PRM19] as

$$\|\tilde{p}\|^2_{\tilde{\mathcal{B}}_{\mathrm{MPT}}} = \sum_{j=1}^{J} \langle \tilde{K}_j \nabla \tilde{p}_j, \nabla \tilde{p}_j \rangle + \langle \tilde{\xi}_j \tilde{p}_j, \tilde{p}_j \rangle.$$

The associated preconditioner, arising from the above norm, for (III.3.5) is

$$\tilde{\mathcal{B}}_{\mathrm{MPT}} = \begin{pmatrix} (-\tilde{K}_1 \Delta + \tilde{\xi}_1 I)^{-1} & 0 & \cdots & 0 \\ 0 & (-\tilde{K}_2 \Delta + \tilde{\xi}_2 I)^{-1} & \cdots & 0 \\ \vdots & \vdots & \ddots & \vdots \\ 0 & 0 & \cdots & (-\tilde{K}_J \Delta + \tilde{\xi}_J I)^{-1} \end{pmatrix}. \tag{III.3.7}$$

Clearly, $\tilde{\mathcal{A}}_{\mathrm{MPT}}$ and $\tilde{\mathcal{B}}^{-1}_{\mathrm{MPT}}$ are trivially spectrally equivalent. We refer to [PRM19] for numerical experiments comparing the standard and transformed formulation and preconditioners.

III.3.4 Finding the transformation matrix

There are two cases that we will consider; the first case is when the matrix $C = K^{-1}E$ (c.f. Theorem (III.A.2)) has J distinct eigenvalues, while the second case will be for the case where at least one of the eigenvalues is repeated. In the case of distinct eigenvalues, the number of distinct eigenvalues of $C = K^{-1}E$ will depend on the material parameter values K_j and $\xi_{j\to i}$ for $1 \leq i, j \leq J$. In the common case where C has J distinct eigenvalues, the transformation matrix is easily defined as follows. Let $\lambda_1, \dots, \lambda_J$ be the real eigenvalues of C, and let $v_1, \dots, v_J$ be the corresponding normalized eigenvectors. Then,

$$P = [v_1, \dots, v_J], \tag{III.3.8}$$

will diagonalize K and E by congruence. In [PRM19], we presented numerical examples for the case of J distinct eigenvalues (with $J = 2$).

The congruence matrix for the case of repeated eigenvalues is also easily constructed. For these cases, the transform P can be constructed by repeated application of block-wise eigenvector matrices, see [HJ90] for the general procedure. In Example III.3.1 below, we present an example on how to obtain the transformation matrix P in the case where one of the eigenvalues has algebraic multiplicity 2 with $J = 3$.

Example III.3.1. In this example we show how to obtain the transformation matrix P for a three–network case when one of the eigenvalues of $K^{-1}E$ has algebraic multiplicity 2. In this example, due to the presence of the repeated eigenvector, the construction of P does not follow directly from the use of normalized eigenvectors and, thus, P is not normalized a priori. We will, however, normalize P following construction to maintain consistency with the previous case; in practice, either the normalized or non-normalized version of P may be used.

$$K = \begin{pmatrix} 1.0 & 0 & 0 \\ 0 & 0.0001 & 0 \\ 0 & 0 & 0.01 \end{pmatrix}, \quad E = \begin{pmatrix} 1.01 & -0.01 & -1.0 \\ -0.01 & 0.0101 & -0.0001 \\ -1.0 & -0.0001 & 1.0001 \end{pmatrix}. \tag{III.3.9}$$

By definition

$$C = K^{-1}E = \begin{pmatrix} 1.01 & -0.01 & -1.0 \\ -100 & 101 & -1.0 \\ -100 & -0.01 & 100.01 \end{pmatrix}. \tag{III.3.10}$$

The eigenvalues $\lambda_1, \lambda_2, \lambda_3$ and eigenvectors $[v_1, v_2, v_3] = P_1$ of C are then:

$$\begin{aligned} &\lambda_1 = 0, \quad \lambda_2 = \lambda_3 = 101.01; \\ &P_1 = \begin{pmatrix} -0.5773 & -0.0071 & -0.0091 \\ -0.5773 & 0.7070 & -0.4031 \\ -0.5773 & 0.7070 & 0.9150 \end{pmatrix}. \end{aligned} \tag{III.3.11}$$

In this specific case the eigenvalues λ_2, λ_3 have algebraic multiplicity 2 and geometrical multiplicity 1. If we try to diagonalize K and E by congruence via P_1, we obtain

$$\begin{aligned} P_1^T K P_1 &= \begin{pmatrix} 3.3670 \times 10^{-1} & 0 & 0 \\ 0 & 5.1007 \times 10^{-3} & 6.5069 \times 10^{-3} \\ 0 & 6.5069 \times 10^{-3} & 8.4729 \times 10^{-3} \end{pmatrix}, \\ P_1^T E P_1 &= 101.01 \begin{pmatrix} 0 & 0 & 0 \\ 0 & 5.1007 \times 10^{-3} & 6.5069 \times 10^{-3} \\ 0 & 6.5069 \times 10^{-3} & 8.4729 \times 10^{-3} \end{pmatrix}. \end{aligned} \tag{III.3.12}$$

In this case, the resulting matrices are block diagonal. The lower right blocks are multiples of each other. We can diagonalize the lower right blocks by computing the eigen-decomposition of either of these. The lower right block of $P_1^T K P_1$ is

$$\begin{pmatrix} 5.1007 \times 10^{-3} & 6.5069 \times 10^{-3} \\ 6.5069 \times 10^{-3} & 8.4729 \times 10^{-3} \end{pmatrix} \tag{III.3.13}$$

and its eigenpairs are

$$\begin{aligned} &\lambda_1 = 6.4967 \times 10^{-5}, \lambda_2 = 1.3508 \times 10^{-2}; \\ &P_2 = \begin{pmatrix} -0.79083 & -0.6120 \\ 0.6120 & -0.7908 \end{pmatrix}. \end{aligned} \tag{III.3.14}$$

The final transformation matrix P that diagonalizes K and E by congruence is then:

$$P = P_1 \begin{pmatrix} 1 & \begin{matrix} 0 & 0 \end{matrix} \\ \begin{matrix} 0 \\ 0 \end{matrix} & P_2 \end{pmatrix} = \begin{pmatrix} -5.7735 \times 10^{-1} & 7.1935 \times 10^{-5} & 1.1575 \times 10^{-2} \\ -5.7735 \times 10^{-1} & -8.0594 \times 10^{-1} & -1.1391 \times 10^{-1} \\ -5.7735 \times 10^{-1} & 8.6590 \times 10^{-4} & -1.1564 \end{pmatrix}. \tag{III.3.15}$$

Note that despite the columns of P_1 and P_2 are normalized with norm 1, the resulting matrix P's columns are not normalized. After the normalization, the matrix P looks as follows:

$$P = \begin{pmatrix} -5.7735 \times 10^{-1} & 8.9255 \times 10^{-5} & 9.9611 \times 10^{-2} \\ -5.7735 \times 10^{-1} & -9.9999 \times 10^{-1} & -9.8026 \times 10^{-2} \\ -5.7735 \times 10^{-1} & 1.0743 \times 10^{-4} & -9.9513 \times 10^{-1} \end{pmatrix}. \tag{III.3.16}$$

and the diagonalized matrices are as follows

$$\begin{aligned} \tilde{K} = P^T K P &= \begin{pmatrix} 3.3670 \times 10^{-1} & 0 & 0 \\ 0 & 1.0001 \times 10^{-4} & 0 \\ 0 & 0 & 1.0003 \times 10^{-2} \end{pmatrix}, \\ \tilde{E} = P^T E P &= \begin{pmatrix} 0 & 0 & 0 \\ 0 & 1.0102 \times 10^{-2} & 0 \\ 0 & 0 & 1.0104 \end{pmatrix}. \end{aligned} \tag{III.3.17}$$

III.4 Preconditioning the MPET equations via diagonalization

In this section, we present a change of variables for the total pressure formulation of the time-discrete MPET equations; we propose and analyze a preconditioning strategy for the resulting variational formulation. The change of MPET variables is guided by the change of MPT variables presented in the previous section. The notation Q signifies, as in Section III.3, the J-fold product of the Hilbert space W.

III.4.1 Total pressure formulation of the MPET equations

Throughout this paper we assume the boundary conditions:

$$u = 0 \text{ on } \Gamma, \quad (2\mu\varepsilon(u) + \lambda \operatorname{div} u \mathbb{I})\nu = 0 \text{ on } \partial\Omega \backslash \Gamma, \quad p_j = 0 \text{ on } \partial\Omega, j = 1, \ldots, J$$

where ν is the unit outward normal vector field on $\partial\Omega$. The total pressure formulation of Biot's equations [LMW17] and more generally the MPET equations [Lee+19] is a robust mixed variational formulation targeting the nearly incompressible limit ($\lambda \gg 1$). The total pressure, which we will see satisfies $p_0 \in L^2(\Omega)$, is defined by

$$p_0 = \lambda \operatorname{div} u - \alpha \cdot p, \tag{III.4.1}$$

where [1] $\alpha = (\alpha_1, \ldots, \alpha_J) \in \mathbb{R}^J$, $p = (p_1, \ldots, p_J) \in Q$ and $\alpha \cdot p = \sum_{i=1}^{J} \alpha_i p_i \in W$. The total pressure formulation of (III.1.1) then reads as follows: for $t \in (0, T]$,

---

[1] Note that we start counting at 1 in the definition of p here and throughout, in contrast to e.g. in [PRM19].

find the displacement vector field u and the pressure scalar fields p_0 and p_j for $j = 1, \dots, J$ such that

$$-\operatorname{div}(2\mu\varepsilon(u) + p_0\mathbb{I}) = f, \tag{III.4.2a}$$

$$\operatorname{div} u - \lambda^{-1}p_0 - \lambda^{-1}\alpha \cdot p = 0, \tag{III.4.2b}$$

$$\lambda^{-1}\dot{p}_0 + s_j\dot{p}_j - \operatorname{div}(K_j\nabla p_j) + \alpha_j\lambda^{-1}\alpha \cdot \dot{p} + \textstyle\sum_{i=1}^{J} \xi_{j\leftarrow i}(p_j - p_i) = g_j, \tag{III.4.2c}$$

for $j = 1, \dots, J$.

We consider an implicit Euler discretization in time of the total pressure formulation of the time-dependent MPET equations (III.4.2) and examine the resulting stationary problem at each time step. The resulting time-discrete version of (III.4.2) with time step $\tau > 0$ reads as follows: find the displacement u and the pressures p_j for $0 \leq j \leq J$ such that

$$-\operatorname{div}(2\mu\varepsilon(u) + p_0\mathbb{I}) = f, \tag{III.4.3a}$$

$$\operatorname{div} u - \lambda^{-1}p_0 - \lambda^{-1}\alpha \cdot p = 0, \tag{III.4.3b}$$

$$-s_jp_j - \alpha_j\lambda^{-1}p_0 - \alpha_j\lambda^{-1}\alpha \cdot p + \tau\operatorname{div}(K_j\nabla p_j) - \tau\textstyle\sum_{i=1}^{J} \xi_{j\leftarrow i}(p_j - p_i) = g_j, \tag{III.4.3c}$$

for $1 \leq j \leq J$ where the new right hand sides g_j for $j = 1, \dots, J$ have been negated and contain also terms from the previous time-step. Again, we impose homogeneous Dirichlet boundary conditions for all network pressures: $p_j = 0$ on $\partial\Omega$ for $1 \leq j \leq J$.

Let $V = H^1_\Gamma(\Omega; \mathbb{R}^d)$, $Q_0 = L^2(\Omega)$ and $Q_j = W = H^1_0(\Omega)$ for $1 \leq j \leq J$ and $\Omega \subset \mathbb{R}^d$. Let $Q = Q_1 \times \cdots \times Q_J$. As in Section III.3, we write $p = (p_1, \dots, p_J)$, $q = (q_1, \dots, q_J)$, and $g = (g_1, \dots, g_J)$. Multiplying by test functions, and integrating second-order derivatives by parts, we obtain the following variational formulation of (III.4.3): find $u \in V$ and $p_i \in Q_i$ for $i = 0, \dots, J$ such that

$$a(u, v) + b(v, p_0) = \langle f, v\rangle \quad \forall\, v \in V, \tag{III.4.4a}$$

$$b(u, q_0) - c_1(p_0, q_0) - c_2(q_0, p) = 0 \qquad \forall\, q_0 \in Q_0, \tag{III.4.4b}$$

$$-c_2(p_0, q) - c_3(p, q) = \langle g, q\rangle \quad \forall\, q \in Q. \tag{III.4.4c}$$

The bilinear forms $a : V \times V \to \mathbb{R}$ and $b : V \times Q_0 \to \mathbb{R}$ are defined as:

$$a(u, v) = \langle 2\mu\varepsilon(u), \varepsilon(v)\rangle, \qquad b(v, q_0) = \langle \operatorname{div} v, q_0\rangle, \tag{III.4.5}$$

while $c_1 : Q_0 \times Q_0 \to \mathbb{R}$, $c_2 : Q_0 \times Q \to \mathbb{R}$, and $c_3 : Q \times Q \to \mathbb{R}$ are defined as:

$$c_1(p_0, q_0) = \langle \lambda^{-1}p_0, q_0\rangle, \tag{III.4.6}$$

$$c_2(p_0, q) = \langle \lambda^{-1}\alpha \cdot q, p_0\rangle, \tag{III.4.7}$$

$$c_3(p, q) = \tau\sum_{j=1}^{J}\langle K_j\,\nabla p_j, \nabla q_j\rangle + \sum_{j=1}^{J}\langle s_jp_j, q_j\rangle, \tag{III.4.8}$$

$$+\tau\sum_{j=1}^{J}\sum_{i=1}^{J}\langle \xi_{j\leftarrow i}(p_j-p_i),q_j\rangle+\langle \lambda^{-1}\alpha\cdot p,\alpha\cdot q\rangle.$$

For future reference we define $c:(Q_0\times Q)\times(Q_0\times Q)\to\mathbb{R}$ via

$$c((p_0,p),(q_0,q))=c_1(p_0,q_0)+c_2(p_0,q)+c_2(q_0,p)+c_3(p,q). \tag{III.4.9}$$

III.4.2 MPET as a parameter-dependent saddle point system

Constructing parameter-robust block preconditioners for the system (III.4.4) is non-trivial. Here we demonstrate how the technique of diagonalization by congruence [PRM19], [Hon+19, Rmk. 6] allows for easily extending the MPT preconditioning approach to that of the MPET system. Note that the system (III.4.3) or equivalently (III.4.4) can be viewed as a saddle point problem with a stabilization term (given by the bilinear form c). Thus, the equations fit well into Brezzi saddle point theory [Bre74]. However, various material parameters in different ranges are involved in the system, so constructing parameter-robust preconditioners for this system is not a straightforward application of the Brezzi theory. Let us recall the parameter ranges we are concerned with in this paper. The existing literature cover the parameters

$$0\le s_j\lesssim 1,\qquad 0<K_j\ll 1,\qquad 1\lesssim\mu\lesssim\lambda<+\infty,\qquad (1\le j\le J).$$

In addition to these we are also interested in developing preconditioners which are robust for the ratios of the exchange coefficients $\xi_{i\to j}$'s.

We first consider construction of preconditioners utilizing the saddle point problem structure. To reveal the saddle point problem structure of (III.4.4) let us look at the operator form of (III.4.4), which is

$$\mathcal{A}_{\mathrm{MPET}}\begin{pmatrix}u\\p_0\\p\end{pmatrix}=\begin{pmatrix}-2\operatorname{div}(\mu\varepsilon) & -\nabla & \mathbf{0}\\ \operatorname{div} & -C_1 & -C_2^*\\ \mathbf{0} & -C_2 & -C_3\end{pmatrix}\begin{pmatrix}u\\p_0\\p\end{pmatrix}=\begin{pmatrix}f\\0\\g\end{pmatrix} \tag{III.4.10}$$

where $C_1:Q_0\to Q_0^*$, $C_2:Q_0\to Q^*$, $C_3:Q\to Q^*$ are the operators associated to the bilinear forms c_1, c_2, c_3 in (III.4.6), (III.4.7), (III.4.8). Here C_2^* is the adjoint operator of C_2. We can rewrite $\mathcal{A}_{\mathrm{MPET}}$ of (III.4.10) in the standard saddle point form

$$\mathcal{A}_{\mathrm{MPET}}=\begin{pmatrix}A & B_0^*\\ B_0 & -C\end{pmatrix}$$

by considering the product space grouping $V\times(Q_0\times Q)$ and identifying

$$A=-2\operatorname{div}(\mu\varepsilon),\qquad B_0=(\operatorname{div},\mathbf{0})^T,\qquad C=\begin{pmatrix}C_1 & C_2^*\\ C_2 & C_3\end{pmatrix}. \tag{III.4.11}$$

One of natural approaches to construct block preconditioners for this system is to use the block diagonal operator

$$\begin{pmatrix}A^{-1} & 0\\ 0 & (C+B_0A^{-1}B_0^*)^{-1}\end{pmatrix}$$

or its approximation. However, the operator $(C + B_0 A^{-1} B_0^*)^{-1}$ is not easy to implement efficiently in practice. Moreover, the analysis for spectral equivalence of this type of preconditioners is related to a non-trivial generalized eigenvalue problem. More precisely, the spectral equivalence is equivalent to uniform upper and lower bounds of the generalized eigenvalues, so it requires a deep analysis of the non-trivial generalized eigenvalue problem utilizing block matrix structures. In this paper we consider a general MPET model with general J and general (constant) exchange coefficients, so the number of blocks in block matrices is not restricted. This makes an analysis of the generalized eigenvalue problem even more challenging, so we will not pursue this approach further in this paper.

Another natural choice of block preconditioners for this system is a direct extension of the preconditioner in [LMW17]. In other words, we use the block diagonal operator of the form

$$\mathcal{B}_{\mathrm{MPET}} = \begin{pmatrix} (-\mu\Delta)^{-1} & 0 & 0 \\ 0 & I^{-1} & 0 \\ 0 & 0 & D^{-1} \end{pmatrix}, \tag{III.4.12}$$

where $I : Q_0 \to Q_0^*$ is the operator defined by the bilinear form $\langle p_0, q_0 \rangle$ for $p_0, q_0 \in Q_0$, $D : Q \to Q^*$ is the block diagonal operator such that its j-th diagonal block $(1 \leq j \leq J)$ is defined by selecting the j-th diagonal entry of the operator C_3 associated to the bilinear form (III.4.8); that is

$$\tau \langle K_j \nabla p_j, \nabla q_j \rangle + \langle s_j p_j, q_j \rangle + \tau \langle \xi_j p_j, q_j \rangle + \langle \lambda^{-1} \alpha_j p_j, \alpha_j q_j \rangle, \qquad p, q \in Q.$$

However, this preconditioner is not robust with respect to the material parameters, particularly for the hydraulic conductivity and the exchange coefficients. We illustrate numerical experiment results in Example III.4.1.

Example III.4.1. Let $\Omega = [0,1]^2 \subset \mathbb{R}^2$, and consider a structured triangulation $\mathcal{T}_h$ of Ω constructed by dividing Ω into $N \times N$ squares and then subdividing each square by a fixed diagonal. Let $J = 2$. Consider a finite element discretization of (III.4.4) using the lowest order Taylor–Hood-type elements i.e. continuous piecewise quadratics for each displacement component, and continuous piecewise linear for all pressures [Lee+19]. Let $\tau = 1.0$, $\mu = 1.0$, $s_j = 1.0$, $\alpha_j = 0.5$ and $K_1 = 1.0$, and consider ranges of values for $\lambda, \xi_{1\leftarrow 2}$ and K_2. We consider the case for $s_1 = s_2 = 1.0$ and $s_1 = s_2 = 0.0$. Starting from an initial random guess, we consider a MinRes solver of the resulting linear system of equations with an algebraic multigrid (Hypre AMG) preconditioner of the form (III.4.12). The convergence criterion used was

$$(\mathcal{B} r_k, r_k)/(\mathcal{B} r_0, r_0) \leq 10^{-6}$$

where r_k is the residual of the k-th iteration. The resulting number of Krylov iterations are shown in Table III.2 for $\xi_{1\to 2} = 10^6$ and ranges of K_2 and λ. We observe that the number of iterations is moderate (≈ 30) for K_2 of comparable magnitude (10^6) to $\xi_{1\leftarrow 2}$. The number of iterations increase with decreasing K_2: up to ≈ 1000 for $K_2 = 1$. For large K_2, the number of iterations seems

K_2	λ	$N = 16$	32	64	128
10^0	10^0	738	1271	1756	1938
	10^2	1024	1505	1679	1631
	10^4	1028	1506	1666	1628
	10^6	1004	1499	1677	1633
10^2	10^0	396	424	406	353
	10^2	337	368	351	333
	10^4	364	352	348	332
	10^6	345	357	361	328
10^4	10^0	65	65	62	60
	10^2	64	60	56	55
	10^4	62	60	57	55
	10^6	63	61	58	55
10^6	10^0	30	30	30	28
	10^2	34	31	29	29
	10^4	32	31	31	29
	10^6	33	31	31	29

Table III.2: Number of MinRes iterations (c.f. Example III.4.1): (III.4.4) as discretized with Taylor-Hood type elements and an algebraic multigrid preconditioner of the form (III.4.12). Of note is the fact that the number of iterations grow for K_2 decreasing relative to $\xi_{2\to 1} = 10^6$, and for increasing N.

independent of the mesh resolution N. In contrast, for smaller K_2 (relative to $\xi_{1\to 2}$), the number of iterations also increase with the mesh resolution. We note that the iteration counts do not vary substantially with λ.

III.4.3 Diagonalizing the MPET equations by congruence

In this subsection, we present MPET equations which are transformed via change of variables for construction of block preconditioners. As in the MPT problem we will find an invertible linear map $P \in \mathbb{R}^{J\times J}$ that provides a fortuitous co-diagonalization; we will then consider the change of variables

$$p = (P \otimes I_W)\,\tilde{p},$$

which will lead to a (partial) diagonalization, in the spirit of Lemma III.2.1, for the transformed MPET system in the new unknowns $(u, p_0, \tilde{p})$. For the discussions below let us give remarks on the block operators defined by c_1, c_2, c_3. Specifically, regarding α as a column vector,

$$C_2 = \left(\lambda^{-1}\alpha\right) \otimes I_W, \quad C_3 = -\tau K \otimes \Delta + (S + \tau E + L) \otimes I_W, \qquad \text{(III.4.13)}$$

with K and E as in (III.3.1), L is the matrix $L_{ij} = \lambda^{-1}\alpha_i\alpha_j$, S is the diagonal matrix such that its j-th entry is s_j, and I_W is the identity (functional) on W; we recall that Q is the J-fold Cartesian product of W. We will first describe the transformed MPET equations for general coordinate transformation, P. From the form of the transformed equations, we will extract the conditions for P that yield a system that is suitable for the construction of parameter-robust block preconditioners.

Suppose we have an, fixed but otherwise arbitrary, invertible coordinate transformation matrix $P \in \mathbb{R}^{J\times J}$. Applying this transformation of variables to the semi-discretized total pressure variational formulation of the MPET equations (III.4.4), we obtain the following variational formulation: find the displacement $u \in V$, the total pressure $p_0 \in Q_0$ and the transformed pressures $\tilde{p} = (\tilde{p}_1, \ldots, \tilde{p}_J) \in Q$ such that

$$\begin{aligned} a(u,v) + b(v,p_0) &= \langle f, v\rangle & \forall\, v \in V, \qquad &\text{(III.4.14a)}\\ b(u,q_0) - c_1(p_0,q_0) - \tilde{c}_2(q_0,\tilde{p}) &= 0 & \forall\, q_0 \in Q_0, \qquad &\text{(III.4.14b)}\\ -\tilde{c}_2(p_0,\tilde{q}) - \tilde{c}_3(\tilde{p},\tilde{q}) &= \langle g, (P\otimes I_W)\,\tilde{q}\rangle & \forall\, \tilde{q} \in Q \qquad &\text{(III.4.14c)} \end{aligned}$$

where

$$\tilde{c}_2(q_0,\tilde{q}) \equiv c_2(q_0,(P\otimes I_W)\,\tilde{q}), \qquad \tilde{c}_3(\tilde{p},\tilde{q}) \equiv c_3((P\otimes I_W)\,\tilde{p},(P\otimes I_W)\,\tilde{q}). \tag{III.4.15}$$

We define $\tilde{\mathcal{A}}_{\text{MPET}} : V \times Q_0 \times Q \to (V\times Q_0\times Q)^*$ as the operator corresponding to the bilinear form (III.4.14). The operator form of the transformed system (III.4.14) then reads as:

$$\tilde{\mathcal{A}}_{\text{MPET}} \begin{pmatrix} u \\ p_0 \\ \tilde{p} \end{pmatrix} = \begin{pmatrix} f \\ 0 \\ \tilde{g} \end{pmatrix}, \quad \tilde{\mathcal{A}}_{\text{MPET}} = \begin{pmatrix} A & B^T & \mathbf{0} \\ B & -C_1 & -\tilde{C_2}^* \\ \mathbf{0} & -\tilde{C_2} & -\tilde{C_3} \end{pmatrix}, \tag{III.4.16}$$

where $A = -2\operatorname{div}(\mu\varepsilon)$, $B = \operatorname{div}$ as before, and $\tilde{g} = \left(P^T \otimes I_W\right) g$. By inserting (III.4.13) and reordering, we note that

$$\begin{aligned} \tilde{C_2} &= P^T C_2 = (\lambda^{-1} P^T \alpha) \otimes I_W, \\ \tilde{C_3} &= P^T C_3 P = -\tau(P^T K P) \otimes \Delta + \left(P^T S P + P^T\,(\tau E + L)\,P\right) \otimes I_W. \end{aligned}$$

For simplicity we will write

$$\tilde{\alpha} = \left(P^T \otimes I_W\right) \alpha. \tag{III.4.17}$$

We now look to apply Lemma III.2.1 with the choice of operators $S = K \otimes \Delta$ and $T = (\tau E + L) \otimes I_W$. The matrices K and $\tau E + L$ satisfy the required conditions and, thus, there exists (c.f. Appendix III.A) an invertible transformation P simultaneously diagonalizing K and $\tau E + L$ by congruence. That is, we have matrices $\tilde{K}$ and $\tilde{\Gamma}$ given by the formulas

$$\tilde{K} = P^T K P = \operatorname{diag}(\tilde{K}_1, \ldots, \tilde{K}_J), \tag{III.4.18}$$

$$\tilde{\Gamma} = P^T \left(\tau E + L\right) P = \operatorname{diag}(\tilde{\gamma}_1, \dots, \tilde{\gamma}_J). \tag{III.4.19}$$

We point out that the storage coefficients $\{s_j\}_{j=1}^J$ are not involved in this simultaneous diagonalization process. This is critically important in order to achieve a preconditioner that is parameter-robust, even in the presence of vanishing storage coefficients. For future reference we briefly note that

$$\tilde{\gamma}_j \geq \tilde{\alpha}_j^2/\lambda, \tag{III.4.20}$$

follows from the definition of $\tilde{\Gamma}$ in (III.4.19) since E is positive semi-definite and therefore $\tilde{\gamma}_j$ is greater than or equal to the j-th diagonal entry of the matrix $\left(P^T LP\right)_{ij} = \lambda^{-1}\tilde{\alpha}_i\tilde{\alpha}_j$.

We also remark that the following identity holds for $\tilde{c}_3$:

$$\begin{aligned}\tilde{c}_3(\tilde{p}, \tilde{q}) = \tau \sum_{j=1}^{J} \langle \tilde{K}_j \nabla \tilde{p}_j, \nabla \tilde{q}_j \rangle + \sum_{j=1}^{J} \langle s_j \left((P \otimes I_W) \tilde{p} \right) \right)_j, \left((P \otimes I_W) \tilde{q} \right)_j \rangle, \\ \qquad \text{(III.4.21)} \\ + \tau \sum_{j=1}^{J}\sum_{i=1}^{J} \langle \xi_{j\leftarrow i} (((P \otimes I_W) \tilde{p})_j - ((P \otimes I_W) \tilde{p})_i), ((P \otimes I_W) \tilde{q})_j \rangle \\ + \langle \lambda^{-1} \tilde{\alpha} \cdot \tilde{p}, \tilde{\alpha} \cdot \tilde{q} \rangle\end{aligned}$$

where $\left((P \otimes I_W) \tilde{p}\right)_j$ is the j-th component of $(P \otimes I_W) \tilde{p}$.

III.4.4 Preconditioning of the transformed MPET system

In this subsection we show that a parameter-robust preconditioner can be constructed using an appropriate parameter-dependent norm.

We first define a parameter-dependent norm

$$\|(u, p_0, \tilde{p})\|_{\tilde{\mathcal{B}}}^2 = \|\varepsilon(u)\|_{2\mu}^2 + \|p_0\|_{(2\mu)^{-1}}^2 + \sum_{j=1}^{J} \| \nabla \tilde{p}_j \|_{\tau\tilde{K}_j}^2 + \sum_{j=1}^{J} \|\tilde{p}_j\|_{\tilde{\gamma}_j}^2 \tag{III.4.22}$$

and consider the associated block preconditioner of the form

$$\tilde{\mathcal{B}}_{\text{MPET}} = \begin{pmatrix} (-2\mu\Delta)^{-1} & 0 & 0 & \cdots & 0 \\ 0 & 2\mu I^{-1} & 0 & \cdots & 0 \\ 0 & 0 & (-\tau\tilde{K}_1\Delta + \tilde{\gamma}_1 I)^{-1} & \cdots & 0 \\ \vdots & \vdots & \vdots & \ddots & \vdots \\ 0 & 0 & 0 & \cdots & (-\tau\tilde{K}_J\Delta + \tilde{\gamma}_J I)^{-1} \end{pmatrix}. \tag{III.4.23}$$

Lemma III.4.2 (Continuity)**.** *Let $\tilde{\mathcal{A}}_{\text{MPET}}$ be defined by* (III.4.16)*, and consider the norm defined by* (III.4.22)*. We assume that $2\mu \leq M_0\lambda$ for some $M_0 > 0$ and $s_j \lesssim \tilde{\gamma}_j$ for $1 \leq j \leq J$. Then there exists a constant $C > 0$, dependent on M_0,* *the constants in* $s_j \lesssim \tilde{\gamma}_j$*, the matrix* P *but independent of any other problem parameters, such that*

$$\langle \tilde{\mathcal{A}}_{\mathrm{MPET}}(u, p_0, \tilde{p}), (v, q_0, \tilde{q}) \rangle \leq C \|(u, p_0, \tilde{p})\|_{\tilde{\mathcal{B}}} \|(v, q_0, \tilde{q})\|_{\tilde{\mathcal{B}}}, \tag{III.4.24}$$

for all $(u, p_0, \tilde{p}), (v, q_0, \tilde{q}) \in V \times Q_0 \times Q$*.*

Proof. By redistributing the material parameter weights and the Cauchy-Schwarz inequality, we obtain the preliminary upper bound

$$\langle \tilde{\mathcal{A}}_{\mathrm{MPET}}(u, p_0, \tilde{p}), (v, q_0, \tilde{q}) \rangle \leq Z_1 + Z_2 + Z_3 =: Z,$$

where

$$\begin{aligned}
Z_1 &= \|\varepsilon(u)\|_{2\mu} \|\varepsilon(v)\|_{2\mu} + \|p_0\|_{(2\mu)^{-1}} \|\operatorname{div} v\|_{2\mu} + \|q_0\|_{(2\mu)^{-1}} \|\operatorname{div} u\|_{2\mu}, \\
Z_2 &= \|p_0\|_{\lambda^{-1}} \|q_0\|_{\lambda^{-1}} + \|\tilde{\alpha} \cdot \tilde{q}\|_{\lambda^{-1}} \|p_0\|_{\lambda^{-1}} + \|\tilde{\alpha} \cdot \tilde{p}\|_{\lambda^{-1}} \|q_0\|_{\lambda^{-1}}, \\
Z_3 &= \textstyle\sum_{j=1}^{J} \left(\|\nabla \tilde{p}_j\|_{\tau \tilde{K}_j} \|\nabla \tilde{q}_j\|_{\tau \tilde{K}_j} + \|\tilde{p}_j\|_{\tilde{\gamma}_j} \|\tilde{q}_j\|_{\tilde{\gamma}_j} + \langle s_j (P\tilde{p})_j, (P\tilde{q})_j \rangle \right).
\end{aligned}$$

Since $\|\operatorname{div} u\| \leq \|\varepsilon(u)\|$ and by $2\mu \leq M_0 \lambda$ and the assumptions on s_j and $\tilde{\gamma}_j$, it follows that

$$\begin{aligned}
Z \lesssim &\left(\|\varepsilon(u)\|_{2\mu} + \|p_0\|_{(2\mu)^{-1}} + \|\tilde{\alpha} \cdot \tilde{p}\|_{\lambda^{-1}} + \textstyle\sum_{j=1}^{J} \left(\|\nabla \tilde{p}_j\|_{\tau \tilde{K}_j} + \|\tilde{p}_j\|_{\tilde{\gamma}_j} \right) \right) \\
&\times \left(\|\varepsilon(v)\|_{2\mu} + \|q_0\|_{(2\mu)^{-1}} + \|\tilde{\alpha} \cdot \tilde{q}\|_{\lambda^{-1}} + \textstyle\sum_{j=1}^{J} \left(\|\nabla \tilde{q}_j\|_{\tau \tilde{K}_j} + \|\tilde{q}_j\|_{\tilde{\gamma}_j} \right) \right).
\end{aligned}$$

By the triangle inequality and (III.4.20) we obtain

$$\|\tilde{\alpha} \cdot \tilde{p}\|_{\lambda^{-1}} \leq \sum_{j=1}^{J} \|\tilde{p}_j\|_{\tilde{\alpha}_j^2/\lambda} \leq \sum_{j=1}^{J} \|\tilde{p}_j\|_{\tilde{\gamma}_j} \tag{III.4.25}$$

and it completes the proof. ■

Lemma III.4.3 (Inf-sup condition)**.** *Let* $\tilde{\mathcal{A}}_{\mathrm{MPET}}$*,* $\tilde{\mathcal{B}}_{\mathrm{MPET}}$ *and all assumptions be as in Lemma III.4.2. Then, there exists a constant* $C > 0$*, dependent on* M_0*, the constants in* $s_j \lesssim \tilde{\gamma}_j$ *but independent of other material parameters, such that*

$$\inf_{(u, p_0, p)} \sup_{(v, q_0, q)} \frac{\langle \tilde{\mathcal{A}}_{\mathrm{MPET}}(u, p_0, p), (v, q_0, q) \rangle}{\|(u, p_0, p)\|_{\tilde{\mathcal{B}}} \|(v, q_0, q)\|_{\tilde{\mathcal{B}}}} \geq C, \tag{III.4.26}$$

where the inf *and* sup *are taken over the non-vanishing elements in* $V \times Q_0 \times Q$*.*

Proof. Consider any $(u, p_0, \tilde{p}) \in V \times Q_0 \times Q$, and choose $\tilde{q} = -\tilde{p}$, and $q_0 = -p_0$. Let $w \in V$ satisfy

$$\langle \operatorname{div} w, p_0 \rangle = \|p_0\|^2_{(2\mu)^{-1}}, \quad \|\varepsilon(w)\|_{2\mu} \leq C_0 \|p_0\|_{(2\mu)^{-1}}. \tag{III.4.27}$$

for a $C_0 > 0$ depending on the domain Ω via Korn's inequality, and next choose $v = u + 2\delta w$ for $\delta > 0$ to be further specified. We note that, with this choice of v, q_0, and q,

$$\|(v, q_0, \tilde{q})\|_{\tilde{\mathcal{B}}} \lesssim \|(u, p_0, \tilde{p})\|_{\tilde{\mathcal{B}}},$$

with inequality constant depending only on the domain Ω and the choice of δ since

$$\|\varepsilon(v)\|_{2\mu} \le \|\varepsilon(u)\|_{2\mu} + 2\delta C_0 \|p_0\|_{(2\mu)^{-1}} \lesssim \|(u, p_0, \tilde{p})\|_{\tilde{\mathcal{B}}}.$$

Therefore, it suffices to show that

$$\langle \tilde{\mathcal{A}}_{\mathrm{MPET}}(u, p_0, \tilde{p}), (v, q_0, \tilde{q})\rangle \gtrsim \|(u, p_0, \tilde{p})\|^2_{\tilde{\mathcal{B}}}. \tag{III.4.28}$$

Using the definition of $\tilde{\mathcal{A}}_{\mathrm{MPET}}$ together with (III.4.27), we find that

$$\begin{aligned}\langle \tilde{\mathcal{A}}_{\mathrm{MPET}}(u, p_0, \tilde{p}), (v, q_0, \tilde{q})\rangle &= \|\varepsilon(u)\|^2_{2\mu} + 2\delta\langle \varepsilon(u), \varepsilon(w)\rangle_{2\mu} + 2\delta\|p_0\|^2_{(2\mu)^{-1}} \\ &\quad + c_1(p_0, p_0) + 2\tilde{c}_2(p_0, \tilde{p}) + \tilde{c}_3(\tilde{p}, \tilde{p}).\end{aligned} \tag{III.4.29}$$

Note that $c_1(p_0, p_0) = \|p_0\|^2_{\lambda^{-1}}$, $\tilde{c}_2(p_0, \tilde{p}) = \langle \tilde{\alpha}\cdot\tilde{p}, p_0\rangle_{\lambda^{-1}}$, and

$$\tilde{c}_3(\tilde{p}, \tilde{p}) = \textstyle\sum_{j=1}^J (\|\nabla \tilde{p}_j\|^2_{\tau\tilde{K}_j} + \|\tilde{p}_j\|^2_{\tilde{\gamma}_j} + \langle s_j(P\tilde{p})_j, (P\tilde{p})_j\rangle)$$

from the definitions of $\tilde{c}_2$, $\tilde{c}_3$, and the congruent diagonalization. Recall the inequality (III.4.25). Then we obtain

$$\begin{aligned}&\delta\|p_0\|^2_{(2\mu)^{-1}} + c_1(p_0, p_0) + 2\tilde{c}_2(p_0, \tilde{p}) + \tilde{c}_3(\tilde{p}, \tilde{p}) \\ &\ge \delta\|p_0\|^2_{(2\mu)^{-1}} + \|p_0\|^2_{\lambda^{-1}} + 2\langle\tilde{\alpha}\cdot\tilde{p}, p_0\rangle_{\lambda^{-1}} + \textstyle\sum_{j=1}^J(\|\tilde{p}_j\|^2_{\tilde{\gamma}_j} + \|\nabla\tilde{p}_j\|^2_{\tau\tilde{K}_j}) \\ &\ge (\delta/M_0 + 1)\,\|p_0\|^2_{\lambda^{-1}} + 2\langle\tilde{\alpha}\cdot\tilde{p}, p_0\rangle_{\lambda^{-1}} + \textstyle\sum_{j=1}^J(\|\tilde{p}_j\|^2_{\tilde{\gamma}_j} + \|\nabla\tilde{p}_j\|^2_{\tau\tilde{K}_j}) \\ &= \|\sqrt{\delta/M_0 + 1}p_0 + \tilde{\alpha}\cdot\tilde{p}\|^2_{\lambda^{-1}} - \left(\frac{\delta}{M_0} + 1\right)^{-1}\|\tilde{\alpha}\cdot\tilde{p}\|^2_{\lambda^{-1}} \\ &\quad + \textstyle\sum_{j=1}^J(\|\tilde{p}_j\|^2_{\tilde{\gamma}_j} + \|\nabla\tilde{p}_j\|^2_{\tau\tilde{K}_j}) \\ &\ge \textstyle\sum_{j=1}^J\left(\dfrac{\delta}{M_0 + \delta}\|\tilde{p}_j\|^2_{\tilde{\gamma}_j} + \|\nabla\tilde{p}_j\|^2_{\tau\tilde{K}_j}\right)\end{aligned}$$

where the second inequality in the above follows from the assumption $2\mu \le M_0\lambda$ and the third inequality follows from (III.4.25). Thus,

$$\begin{aligned}&\langle \tilde{\mathcal{A}}_{\mathrm{MPET}}(u, p_0, \tilde{p}), (v, q_0, \tilde{q})\rangle \\ &\quad \ge \|\varepsilon(u)\|^2_{2\mu} + \delta\langle\varepsilon(u), \varepsilon(w)\rangle_{2\mu} + \delta\|p_0\|^2_{(2\mu)^{-1}} + \textstyle\sum_{j=1}^J\|\nabla\tilde{p}_j\|^2_{\tau\tilde{K}_j} \\ &\quad + \dfrac{\delta}{M_0 + \delta}\textstyle\sum_{j=1}^J\|\tilde{p}_j\|^2_{\tilde{\gamma}_j}.\end{aligned} \tag{III.4.30}$$

On the other hand, the Cauchy-Schwarz inequality, the definition of w, and Young's inequality give that

$$\delta|\langle\varepsilon(u), \varepsilon(w)\rangle_{2\mu}| \le \delta C_0\|\varepsilon(u)\|_{2\mu}\|p_0\|_{(2\mu)^{-1}} \le \frac{1}{2}\|\varepsilon(u)\|^2_{2\mu} + \frac{1}{2}\delta^2 C_0^2\|p_0\|^2_{(2\mu)^{-1}}. \tag{III.4.31}$$

Inserting the negation of (III.4.31) as a lower bound in (III.4.30), we thus obtain that

$$\begin{aligned}&\langle \tilde{\mathcal{A}}_{\mathrm{MPET}}(u, p_0, \tilde{p}), (v, q_0, \tilde{q})\rangle \\ &\geq \frac{1}{2}\|\varepsilon(u)\|^2_{2\mu} + \delta(1 - \frac{1}{2}\delta C_0^2)\|p_0\|^2_{(2\mu)^{-1}} + \textstyle\sum_{j=1}^{J}\left(\|\nabla\tilde{p}_j\|^2_{\tau\tilde{K}_j} + \dfrac{\delta}{M_0 + \delta}\|\tilde{p}_j\|^2_{\tilde{\gamma}_j}\right).\end{aligned}$$

By choosing δ, in particular e.g. by letting $\delta < 2/C_0^2$, the estimate (III.4.28) follows. ■

Remark III.4.4. *In Lemma III.4.2 and Lemma III.4.3 we assumed* $s_j \lesssim \tilde{\gamma}_j$ *for* $1 \leq j \leq J$ *and it covers the cases that* s_j*'s are degenerate. This assumption can be removed if* $\lambda^{-1} \lesssim s_j$, $1 \leq j \leq J$, *hold with constants of scale 1. For parameter-robust preconditioners we use* P *which gives a different simultaneous diagonalization. More precisely, we consider* P *satisfying* (III.4.18), *and* $P^T(S + \tau E + L)P = \operatorname{diag}(\tilde{\gamma}_1, \ldots, \tilde{\gamma}_J)$ *instead of* (III.4.19). *The norm* (III.4.22) *with these new* $\tilde{K}_j$*'s and* $\tilde{\gamma}_j$*'s, will be used to obtain parameter-robust preconditioners. Since the modification of proofs is straightforward and most steps are almost same, we omit the detailed proofs.*

For concreteness, we here illustrate the form of the MPET equations and of the proposed preconditioner in a specific example.

Example III.4.5. We consider the simple case of two networks with $K_1 = K_2 = 1.0$, $s_1 = s_2 = 1.0$, $\alpha_1 = \alpha_2 = 0.5$, $\lambda = 1.0$, $\xi_{1\to 2} = 0.0$, and $\tau = 1.0$. The transformation matrix in this case is

$$P = \frac{1}{\sqrt{2}}\begin{pmatrix} 1 & -1 \\ 1 & 1 \end{pmatrix}. \tag{III.4.32}$$

We remark that P is not normalized. The associated transformed MPET operator (cf. (III.4.16) and associated definitions), is then

$$\tilde{\mathcal{A}}_{\mathrm{MPET}} = \begin{pmatrix} -2\mu \operatorname{div}\varepsilon & -\nabla & 0 & 0 \\ \operatorname{div} & -\lambda^{-1} & -(\sqrt{2}\lambda)^{-1} & 0 \\ 0 & -(\sqrt{2}\lambda)^{-1} & -\Delta + \frac{3}{2} & 0 \\ 0 & 0 & 0 & -\Delta + 1 \end{pmatrix}, \tag{III.4.33}$$

and the proposed preconditioner will be in the following form:

$$\tilde{\mathcal{B}}_{\mathrm{MPET}} = \begin{pmatrix} (-2\mu \operatorname{div}\varepsilon)^{-1} & 0 & 0 & 0 \\ 0 & (2\mu)^{-1} & 0 & 0 \\ 0 & 0 & (-\Delta + 1)^{-1} & 0 \\ 0 & 0 & 0 & (-\Delta + 1)^{-1} \end{pmatrix}. \tag{III.4.34}$$

The objective of this example was to illustrate the layout of the operators in a simple case. The results for more general numerical examples will be presented later.

III.4.5 Numerical performance

Example III.4.6. In this example we demonstrate the robustness of the block diagonal preconditioner (III.4.23) for a mixed finite element discretization of the transformed total pressure MPET equations (III.4.16). We consider the same test case, discretization and solver set-up as described in Example III.4.1; the new preconditioner is the only modification. Parameter ranges are as follows: $K_2 \in [10^{-6}, 10^6]$, $\xi_{1\leftarrow 2} \in [10^{-6}, 10^6]$ and $\lambda \in [1, 10^6]$.

The resulting number of iterations are shown in Figure III.1 for $K_2 \in [10^{-6}, 1]$ and $\xi_{1\leftarrow 2} \in [1, 10^6]$ and $s_1 = s_2 = 1.0$; omitted values demonstrated similar behaviours. Each of the subplots in Figure III.1 represents a fixed choice of K_2 and $\xi_{1\leftarrow 2}$. In each subplot four curves are shown; these curves show the number of MinRes iterations corresponding to different values of λ, indicated by their respective symbols, at discretization levels $N = 16$, 32, 64 and 128. In Figure III.2 we performed the same experiments with $s_1 = s_2 = 0.0$.

For completeness we also performed numerical examples for $J = 3, 5, 10$ and $K_j = 1.0$, $s_j = 1.0$, $\xi_{1\leftarrow 2} \in [1, 10^6]$ and $\lambda \in [1, 10^6]$. Results are reported in Figure III.3.

The stopping criterion was

$$(\tilde{\mathcal{B}} r_k, r_k)/(\tilde{\mathcal{B}} r_0, r_0) \leq 10^{-6}$$

where r_k is the residual of the k-th iteration. We observe that the number of iterations is moderate in general. Moreover, the number of iterations does not grow for smaller K_2's relative to larger $\xi_{1\leftarrow 2}$ or larger N in contrast to what was observed for Example III.4.1.

Example III.4.7. In this final example we present a modified version of a 3D footing problem [Gas+08; Rod+18; Sto+19]; we demonstrate the problem for two fluid networks ($J = 2$) and use the standard unit cube, $\Omega = [0, 1]^3 \subset \mathbb{R}^3$, as computational domain. At the base of the domain, homogeneous Dirichlet conditions for the displacement and for both fluid pressures are imposed. At the top-most surface of the domain, i.e. $z = 1$, a load of $0.1 N/m^2$ is applied on the square $[0.25, 0.75] \times [0.25, 0.75]$, and a no flow condition is applied to the fluid pressures. For all remaining boundary sides of the domain, the zero stress condition is applied alongside a homogeneous Dirichlet condition for the fluid pressures. In the numerical experiments we vary the exchange coefficient $\xi_{1\leftarrow 2}$, and the mesh size, the other physical parameters are reported in Table III.3.

In table III.4, we report the number of MinRes iterations for each time-step (from 0.1 to 0.5), varying the mesh size and exchange parameters. The initial guess for the solution is set to zero. Similarly to what observed in Example III.4.6, the number of iterations is moderate also for this 3D case. In Fig. III.4 the solution for $t = 0.5$ is shown.

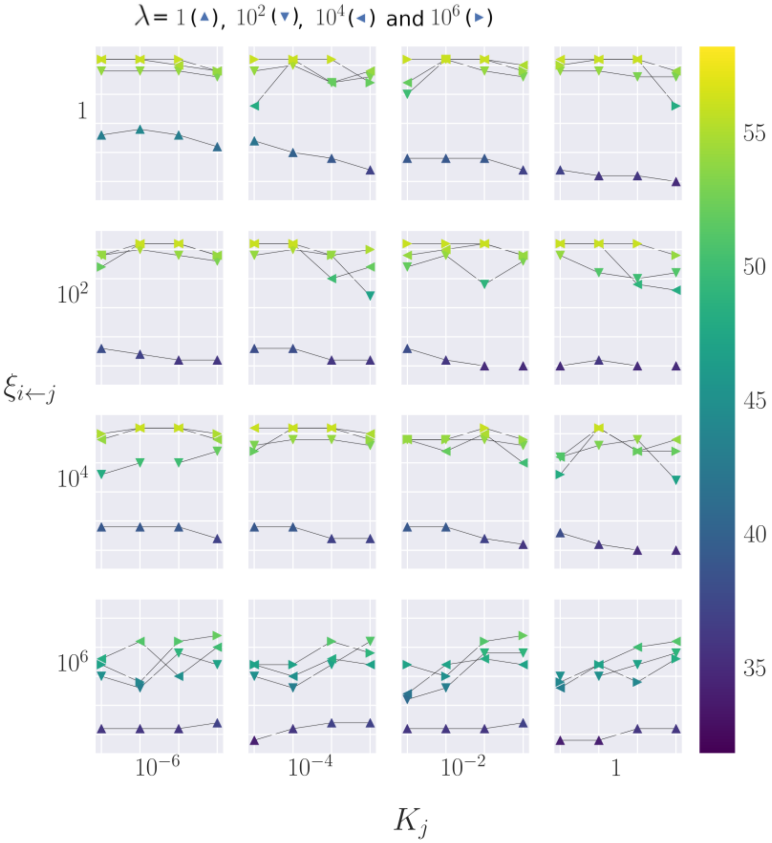

Figure III.1: Number of MinRes iterations: (III.4.4) discretized with Taylor-Hood type elements and algebraic multigrid, for $s_1 = s_2 = 1.0$. K_2 varies along the horizontal axis while the vertical axis shows variations in $\xi_{1\leftarrow 2}$ for K_2 fixed. Each subplot contains four piecewise linear curves; each curve is decorated by a symbol indicating a corresponding value of λ and corresponds to results for discretizations $N = 16, 32, 64$ and 128.

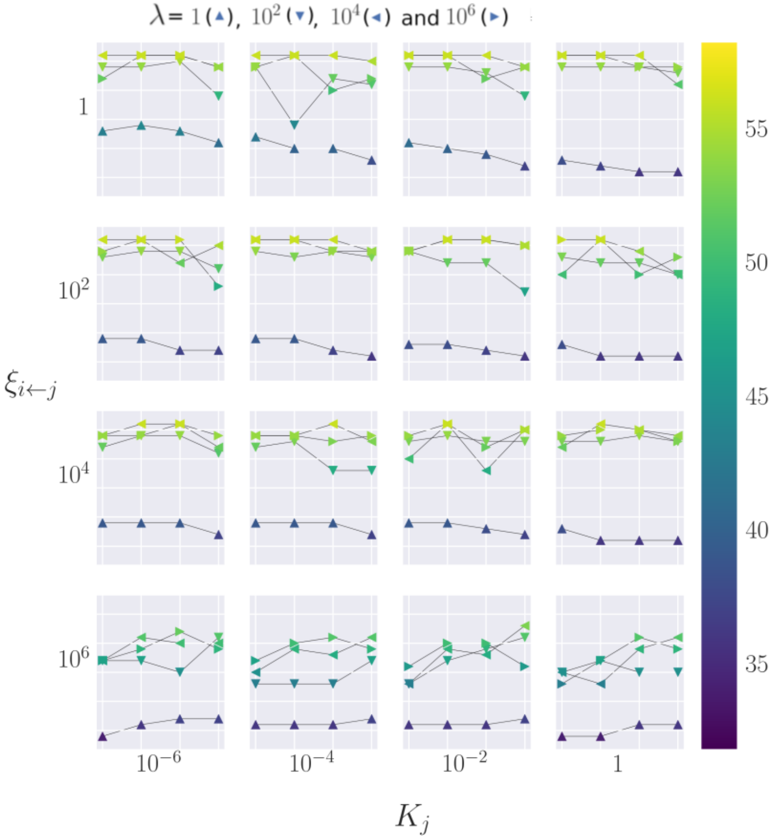

Figure III.2: Number of MinRes iterations: (III.4.4) discretized with Taylor-Hood type elements and algebraic multigrid for $s_1 = s_2 = 0$. K_2 varies along the horizontal axis while the vertical axis shows variations in $\xi_{1\leftarrow 2}$ for K_2 fixed. Each subplot contains four piecewise linear curves; each curve is decorated by a symbol indicating a corresponding value of λ and corresponds to results for discretizations $N = 16, 32, 64$ and 128.

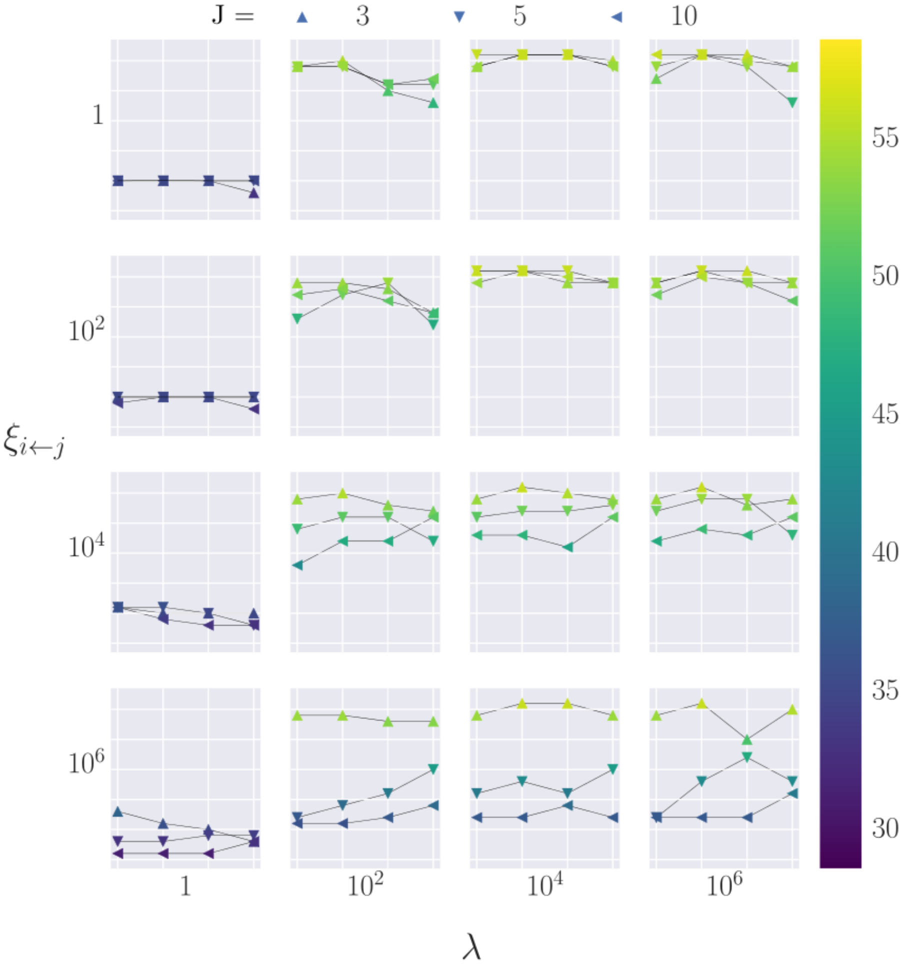

Figure III.3: Number of MinRes iterations: (III.4.4) for $J = 3, 5, 10$ discretized with Taylor-Hood type elements and algebraic multigrid for $K_j = 1.0$, $s_j = 1.0$. λ varies along the horizontal axis while the vertical axis shows variations in $\xi_{i\leftarrow j}$. Each subplot contains one piecewise linear curve and corresponds to results for discretizations $N = 16, 32, 64$ and 128.

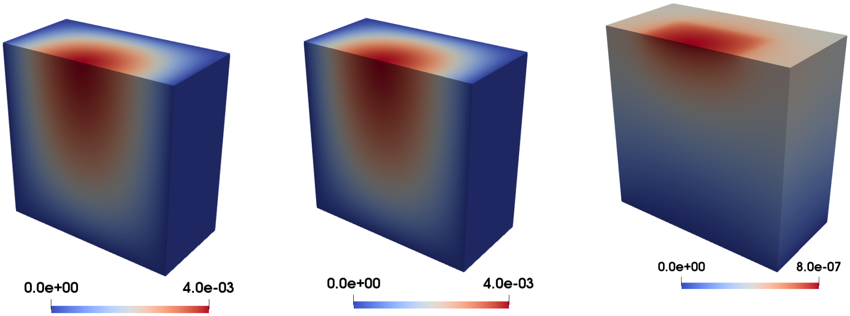

(a) fluid pressure p_1 (b) fluid pressure p_2 (c) displacement magnitude u

Figure III.4: A 3D Footing Problem, solution for $1/h = 32$, $\xi_{1\leftarrow 2} = 1.0$, at $t = 0.5$

Property	Symbol	Value	Units
Young's modulus	E	3×10^4	Pa
Poisson ratio	ν	0.45	[-]
Hydraulic conductivities	K_1, K_2	10^{-6}	$\mathrm{m}^2(\mathrm{Pa\ s})^{-1}$
Storage coefficients	s_1, s_2	0.0	Pa^{-1}
Biot coefficient	α_1, α_2	0.5	[-]

Table III.3: Parameters used in the numerical simulations

h	$\xi_{1\leftarrow 2}$	Number of iterations				
		$t = 0.1$	$t = 0.2$	$t = 0.3$	$t = 0.4$	$t = 0.5$
1/8	1.0×10^{-6}	87	97	97	97	97
	1.0	89	102	102	102	102
1/16	1.0×10^{-6}	90	102	102	102	102
	1.0	93	108	109	107	109
1/32	1.0×10^{-6}	95	107	107	107	107
	1.0	98	112	112	114	111

Table III.4: MinRes iterations for the footing problem (c.f. Example III.4.7).

III.5 Conclusions

In this paper, we have presented a new strategy for decoupling the total-pressure variational formulation of the multiple-network poroelasticity equations. The decoupling strategy is based on a transformation via a change of variables, allowing for simultaneous diagonalization by congruence of the equation operators. In particular, the transformed equations are readily amenable for block–diagonal preconditioning. Moreover, we have proposed a block-diagonal preconditioner for the transformed system and shown theoretically that the preconditioner and the equation operator are norm equivalent, independently of the material parameters, under reasonable parameter assumptions. The theoretical results are supported by numerical examples. Combined, these results allow the efficient iterative solution of the multiple-network poroelasticity equations, even in the case of nearly incompressible materials.

We note that our strategy is based on spatially constant material parameters. The applicability of this approach for spatially varying parameters has not yet been considered.

Appendix III.A Proof of Lemma III.2.1

We first recall a basic [HJ90] definition and result for posterity.

Definition III.A.1. A matrix $C \in \mathbb{C}^{n\times n}$ is *diagonalizable* if there exists an invertible transformation, P, such that $P^{-1}CP$ is diagonal. The matrix C is called *diagonalizable by congruence* if there exists P, not necessarily invertible, such that P^TCP is diagonal.

Theorem III.A.2 (4.5.17a-b p. 287, [HJ90])**.** *Suppose A and $B \in \mathbb{C}^{n\times n}$ are symmetric and that A is invertible. Then A and B are diagonalizable by congruence if and only if $C = A^{-1}B$ is diagonalizable.*

Proof of Lemma III.2.1. Assume K and E satisfy the hypotheses of Lemma III.2.1 and, without loss of generality, suppose that K is positive definite. Then K is invertible and we first show that this implies $C = K^{-1}E \in \mathbb{R}^{n\times n}$ is diagonalizable. We note that C satisfies

$$K^{1/2}CK^{-1/2} = K^{-1/2}EK^{-1/2},$$

where $K^{1/2}$ denotes the (unique, symmetric) principle square root of K. The right-hand side, above, is symmetric due to the symmetry of K and E. Thus C is similar to a real, symmetric matrix and is therefore diagonalizable. From [HJ90, 4.5.17a-b] there exists an invertible matrix $P \in \mathbb{R}^{n\times n}$ such that

$$P^TKP = \tilde{D}_K \quad \text{and} \quad P^TEP = \tilde{D}_E,$$

where $\tilde{D}_K$, $\tilde{D}_E \in \mathbb{R}^{n\times n}$ are diagonal matrices.

Recalling $Q = W \times \cdots \times W$, define the change of variables $\tilde{p} = (P^{-1} \otimes I_W)p$ for $p \in Q$ and substitute into (III.2.5) to get

$$\langle S(P \otimes I_W)\tilde{p}, q\rangle + \langle T(P \otimes I_W)\tilde{p}, q\rangle = \langle f, q\rangle, \quad \forall\, q \in Q.$$

Writing $q = (P \otimes I_W)(P^{-1} \otimes I_W)q$ and noting that the adjoint operator of $P \otimes I_W$ is $P^T \otimes I_{W^*}$, we have

$$\langle S(P \otimes I_W)\tilde{p}, q\rangle = \langle (P^T \otimes I_{W^*})S(P \otimes I_W)\tilde{p}, (P^{-1} \otimes I_W)q\rangle.$$

Since $S = K \otimes A$ we can obtain $(P^T \otimes I_{W^*})S(P \otimes I_W) = \tilde{D}_K \otimes A$ (by the Hadamard product). By a similar argument

$$\langle TP\tilde{p}, q\rangle = \langle (\tilde{D}_E \otimes B)\tilde{p}, (P^{-1} \otimes I_W)q\rangle.$$

Then $D_S := \tilde{D}_K \otimes A$ and $D_T := \tilde{D}_E \otimes B$ are block diagonal operators from Q to Q^*. Finally $\langle f, q\rangle = \langle (P^T \otimes I_{W^*})f, (P^{-1} \otimes I_W)q\rangle$ and the variational problem (III.2.6) follows because $q \in Q$ is arbitrary. ■

Remark III.A.3. *The construction of the matrix P, yielding both $P^TKP = D_1$ and $P^TEP = D_2$, is straightforward for the case when $C = K^{-1}E$ has n distinct eigenvalues. In this case C has n linearly independent eigenvectors; if $\{v_1, \dots, v_n\}$ denote these eigenvectors then $P = [v_1, \dots, v_n]$ is the matrix whose j-th column is v_j. When the eigenvalues of C are not distinct: P can be realized as the product of block-wise eigenvector matrices. The general procedure for this case is discussed in [HJ90]; an example has been discussed in Section III.3. As a point of praxis it should be noted that that diagonalization by congruence can face a practical challenge. In particular, if the eigenvalues of $C = K^{-1}E$ are very large and the eigenvectors of C have one or more small entries then computing the transformation matrix P, using off-the-shelf methods in e.g. Matlab or Mathematica, can be inexact. In such cases, the matrices P^TKP and P^TEP are strongly diagonally dominant but may have off diagonal entries that are approximately zero. In this case, alternative methods to compute the eigenvector matrix P may be useful. For instance, one may consider using a package, such as the Python mpmath package, that supports variable precision to compute the eigenvectors and transformation matrices.*

References

[BER93] Bai, M., Elsworth, D., and Roegiers, J.-C. "Multiporosity/multipermeability approach to the simulation of naturally fractured reservoirs". In: *Water Resources Research* vol. 29, no. 6 (1993), pp. 1621–1633.

[Bio41] Biot, M. A. "General theory of three-dimensional consolidation". In: *Journal of Applied Physics* vol. 12, no. 2 (1941), pp. 155–164.

[BLR19] Brašnová, J., Lukeš, V., and Rohan, E. "Identification of multi-compartment Darcy flow model material parameters". In: *20th International Conference Applied Mechanics 2018: April 9-11, 2018, Myslovice, Czech republic: conference proceedings.* 2019, pp. 9–13.

[Bre74] Brezzi, F. "On the existence, uniqueness and approximation of saddle-point problems arising from Lagrangian multipliers". In: *Rev. Française Automat. Informat. Recherche Opérationnelle Sér. Rouge* vol. 8, no. R-2 (1974), pp. 129–151.

[Cho+16] Chou, D. et al. "A fully dynamic multi-compartmental poroelastic system: Application to aqueductal stenosis". In: *Journal of biomechanics* vol. 49, no. 11 (2016), pp. 2306–2312.

[ES13] Eisenträger, A. and Sobey, I. “Multi-Fluid Poroelastic Modelling of CSF Flow Through the Brain”. In: *Poromechanics V: Proceedings of the Fifth Biot Conference on Poromechanics*. 2013, pp. 2148–2157.

[Gas+08] Gaspar, F. et al. “Distributive smoothers in multigrid for problems with dominating grad-div operators”. In: *Numerical Linear Algebra with Applications* vol. 15 (2008), pp. 661–683.

[HJ90] Horn, R. A. and Johnson, C. R. *Matrix Analysis*. 2nd. Cambridge University press. 1990.

[HK18] Hong, Q. and Kraus, J. “Parameter-robust stability of classical three-field formulation of Biot’s consolidation model”. In: *Electron. Trans. Numer. Anal.* vol. 48 (2018), pp. 202–226.

[Hon+19] Hong, Q. et al. “Conservative discretizations and parameter-robust preconditioners for Biot and multiple-network flux-based poroelasticity models”. In: *Numerical Linear Algebra with Applications* vol. 26, no. 4 (2019), e2242.

[Hon+20a] Hong, Q. et al. “Parameter-robust convergence analysis of fixed-stress split iterative method for multiple-permeability poroelasticity systems”. In: *Multiscale Model. Simul.* vol. 18, no. 2 (2020), pp. 916–941.

[Hon+20b] Hong, Q. et al. “Parameter-robust Uzawa-type iterative methods for double saddle point problems arising in Biot’s consolidation and multiple-network poroelasticity models”. In: *Math. Models. Methods. Appl. Sci.* vol. 30, no. 13 (2020), pp. 2523–2555.

[Józ+] Józsa, T. et al. *A cerebral circulation model for in silico clinical trials of ischaemic stroke*. In the proceedings of CompBioMed Conference 2019.

[Lee+15] Lee, J. et al. “Multiscale modelling of cardiac perfusion”. In: *Modeling the heart and the circulatory system*. Springer, 2015, pp. 51–96.

[Lee+19] Lee, J. J. et al. “A mixed finite element method for nearly incompressible multiple-network poroelasticity”. In: *SIAM Journal on Scientific Computing* vol. 41, no. 2 (2019), A722–A747.

[Lee19] Lee, J. J. “Unconditionally stable second order convergent partitioned methods for multiple-network poroelasticity”. In: *arXiv preprint arXiv:1901.06078* (2019).

[LMW17] Lee, J. J., Mardal, K.-A., and Winther, R. “Parameter-Robust Discretization and Preconditioning of Biot’s Consolidation Model”. In: *SIAM J. Sci. Comp.* vol. 39, no. 1 (2017), A1–A24.

[Mic+13] Michler, C. et al. “A computationally efficient framework for the simulation of cardiac perfusion using a multi-compartment Darcy porous-media flow model”. In: *Int. J. Numer. Method Biomed. Eng.* vol. 29, no. 2 (2013), pp. 217–232.

[MP17] Mokhtarudin, M. J. M. and Payne, S. J. “The study of the function of AQP4 in cerebral ischaemia–reperfusion injury using poroelastic theory”. In: *International Journal for Numerical Methods in Biomedical Engineering* vol. 33, no. 1 (2017), e02784.

[MR11] Mardal, K.-A. and R. Winther. “Preconditioning Discretizations of Systems of Partial Differential Equations”. In: *Numerical Linear Algebra with Applications* vol. 18 (2011), pp. 1–40.

[MW13] Mikelić, A. and Wheeler, M. F. “Convergence of iterative coupling for coupled flow and geomechanics”. In: *Comput. Geosci.* vol. 17, no. 3 (2013), pp. 455–461.

[OR16] Oyarzúa, R. and Ruiz-Baier, R. “Locking-free finite element methods for poroelasticity”. In: *SIAM Journal on Numerical Analysis* vol. 54, no. 5 (2016), pp. 2951–2973.

[PRM19] Piersanti, E., Rognes, M. E., and Mardal, K.-A. “Parameter robust preconditioning for multi–compartmental Darcy equations”. In: (in review for EnuMath 2019). 2019.

[Rod+18] Rodrigo, C. et al. “New stabilized discretizations for poroelasticity and the Stokes’ equations”. In: *Comput. Methods Appl. Mech. Engrg.* vol. 341 (2018), pp. 467–484.

[Shi+20] Shipley, R. et al. “A Four-Compartment Multiscale Model of Fluid and Drug Distribution in Vascular Tumours”. In: *International Journal for Numerical Methods in Biomedical Engineering* (2020), e3315.

[Stø+16] Støverud, K. H. et al. “Poro-elastic modeling of Syringomyelia–a systematic study of the effects of pia mater, central canal, median fissure, white and gray matter on pressure wave propagation and fluid movement within the cervical spinal cord”. In: *Computer Methods in Biomechanics and Biomedical Engineering* vol. 19, no. 6 (2016), pp. 686–698.

[Sto+19] Storvik, E. et al. “On the optimization of the fixed-stress splitting for Biot’s equations”. In: *Int. J. Numer. Methods. Eng.* vol. 120, no. 2 (2019), pp. 179–194.

[TV11] Tully, B. J. and Ventikos, Y. “Cerebral water transport using multiple-network poroelastic theory: application to normal pressure hydrocephalus”. In: *J. Fluid Mech.* vol. 667 (2011), pp. 188–215.

[TV13] Tully, B. and Ventikos, Y. “Modelling Normal Pressure Hydrocephalus as a ‘Two-Hit’Disease Using Multiple-Network Poroelastic Theory”. In: *ASME 2010 Summer Bioengineering Conference.* American Society of Mechanical Engineers Digital Collection. 2013, pp. 877–878.

[Var+16] Vardakis, J. C. et al. “Investigating cerebral oedema using poroelasticity”. In: *Med. Eng. Phys.* vol. 38, no. 1 (2016), pp. 48–57.

Paper IV

Are brain displacements and pressures within the parenchyma induced by surface pressure differences? A computational modelling study

E. Piersanti, M. E. Rognes, V. Vinje

Submitted to bioRχv DOI: 10.1101/2022.09.07.506967

Abstract

The intracranial pressure is implicated in many homeostatic processes in the brain and is a fundamental parameter in several diseases such as e.g. idiopathic normal pressure hydrocephalus (iNPH). The presence of a small but persistent pulsatile intracranial pulsatile transmantle pressure gradient (on the order of a few mmHg/m at peak) has recently been demonstrated in iNPH subjects. A key question is whether pulsatile ICP and displacements can be induced by a small pressure gradient originating from the brain surface e.g. pial arteries alone. In this study, we model the brain parenchyma as either a linearly elastic or a poroelastic medium and impose a pulsatile pressure gradient acting between the ventricular and the pial surfaces. Using this high-resolution physics-based model, we compute the effect of the pulsatile pressure gradient on parenchyma displacement, volume change, fluid pressure, and fluid flux. The resulting displacement field is pulsatile and in qualitatively and quantitatively good agreement with the literature, both with elastic and poroelastic models. However, the pulsatile forces on the boundaries are not sufficient for pressure pulse propagation through the brain parenchyma. Our results suggest that pressure differences originating over the brain surface via e.g. pial artery pulsatility are not sufficient to drive interstitial fluid (ISF) flow within the brain parenchyma and that potential pressure gradients found within the parenchyma rather arise from local pressure pulsations of blood vessels within the brain parenchyma itself.

IV.1 Introduction

The cerebrospinal fluid (CSF) is mainly contained in the subarachnoid space (SAS) and subarachnoid cisterns surrounding the brain parenchyma [SCC11] and plays an important role in maintaining the homeostasis of the brain [Mat+16]. Intracranial pressure (ICP), both its static and pulsatile components, is involved in many of these homeostatic processes [Wil16]. Its fluctuations are related to blood flow, respiration, and cerebral spinal fluid (CSF) flow in the brain. ICP has been the subject of investigations for many years and it is a fundamental parameter to diagnose diseases such as idiopathic normal pressure hydrocephalus (iNPH), and other forms of hydrocephalus [ES10b]. The ICP can also be influenced by changes in anatomy, obstruction of the aqueduct, and traumatic brain injuries for example, and by changes in the material properties of the brain parenchyma due to ageing. In hydrocephalus and iNPH, the intracranial pressure pulsations increase[WEM11], and moreover shunt response may be predicted by the pre-surgical pulse pressure[BS07].

The presence of a transmantle pressure gradient between different areas of the brain has been controversial. Some studies have reported the absence of a transmantle gradient in iNPH patients [ES10a; STW02], and therefore excluded it among the causes of iNPH. Moreover, a study from Eide [Eid08] showed how an uneven distribution of intracranial pulsatility is found in hydrocephalus patients. In more recent work from Vinje et al. [Vin+19] a small pulsatile gradient was analyzed and quantified between the subdural and intraventricular ICP. The analysis of [Vin+19] is based on overnight intracranial pressure measurements from subarachnoid and ventricles areas, in 10 iNPH patients. The pulsatile gradient is mainly characterized by a cardiac component of mean amplitude 1.46 mmHg/m and a respiratory component of mean amplitude 0.52 mmHg/m. However, to what extent these gradients affect pulsatile brain displacements has not yet been investigated. Moreover, the mechanisms behind this pulsatile gradient are not fully understood.

Pressure pulsations within the parenchyma may have at least two possible origins: a "systemic" pressure pulse propagating via the surrounding subarachnoid space (SAS) and then travelling through the entire brain tissue, or from blood vessel pulsations distributed with the parenchyma. The question is ultimately whether the pressure pulse travels through the brain tissue (extracellular matrix) or the blood vessels (blood vessel network). The answer is relevant to assess the possibility of perivascular flow also within the brain (along arterioles and capillaries), as pulsations originating from blood vessels have been suggested to drive bulk flow of perivascular fluid [Ili+13; Jes+15; Mes+18]. In addition, cardiovascular pulsations in the brain can be linked to Alzheimer's disease: cardiovascular impulse latency, propagation speed and direction present very different behaviour in patients with Alzheimer's disease and age-matched healthy volunteers[Raj+21].

The scope of the present paper is therefore to investigate the origin and effects of intracranial pressure gradient pulsatility on the brain parenchyma. We consider two different models for the brain parenchyma: linear elasticity and a one–network poroelasticity (Biot). The pulsatile pressure gradient is modelled as in [Vin+19] and it is applied to each model via appropriate boundary conditions. For the poroelastic case(s), we model the pial surface as permeable or as impermeable. For the linear elasticity case, we study the effect of the cardiac component for the pulsatile gradient alone, and the effect of brain parenchyma incompressibility. In this study, we observed a pulsating displacement field both with the linear elasticity and the poroelasticity model. With the poroelasticity model, we observe that the pressure prescribed on the pial surface does not propagate into the parenchyma neither with the impermeable nor a permeable pial membrane. With the current parameters and boundary conditions, we conclude that it is unlikely that a pulsating pressure difference between the pial and ventricular boundaries is responsible for fluid pressure propagation or interstitial fluid flow in the parenchyma.

IV.2 Materials and methods

IV.2.1 Computational domain

The computational domain is based on the Colin27 human adult brain atlas FEM mesh [Fan10](Figure IV.1a). This mesh consists of gray and white matter regions. Boundary markers were created to divide the domain boundary into one pial and one ventricular surface. The ventricular boundary is shown in Figure IV.1b. The mesh consists of 1 227 992 cells and 265 085 vertices. The minimum cell size h_{min} is 0.1 mm and the maximum cell size h_{max} is 15.7 mm

IV.2.2 Governing equations

IV.2.2.1 Linear elasticity

We first model the deformation of the brain parenchyma as that of an isotropic elastic solid as follows: find the displacement u such that

$$-\operatorname{div}(2\mu\epsilon(u) + \lambda \operatorname{div}(u)\mathbb{I}) = 0, \tag{IV.2.1}$$

where $u = u(x, t)$, for $x \in \Omega \subset \mathbb{R}^3$, $t \in (0, T]$, and $\mathbb{I}$ is the 3×3 identity matrix. The parameters $\lambda > 0$ and $\mu > 0$ are the Lamé elasticity constants.

IV.2.2.2 Poroelasticity

Biot's equations describe a linear, isotropic solid permeated by a single fluid network. The equations read as follows: find the displacement $u = u(x, t)$ and the fluid pressure $p = p(x, t)$ such that

$$-\operatorname{div}(2\mu\epsilon(u) + \lambda \operatorname{div} u\mathbb{I}) + \alpha \nabla p = 0, \tag{IV.2.2a}$$

$$s\dot{p} + \alpha \operatorname{div} \dot{u} - \operatorname{div} K \nabla p = 0. \tag{IV.2.2b}$$

In addition to the parameters present in the linear elasticity system (IV.2.1), we define the Biot-Willis coefficient $\alpha \in (0, 1]$, the storage coefficient $s > 0$, and the hydraulic conductivity tensor $K = \kappa/\nu > 0$ with κ and ν being the permeability and fluid viscosity, respectively. The (Darcy) fluid velocity v, representing the fluid velocity within the porous network i.e. the flow of interstitial fluid, is defined as

$$v = -K\nabla p. \tag{IV.2.3}$$

IV.2.3 Boundary conditions

We consider numerical experiments with different sets of boundary conditions for the elasticity and poroelasticity models. Specifically, we set a pressure difference between the subarachnoid space (pial surface) and the ventricles (ventricular surface). The pressure gradient is modelled, using data from [Vin+19], as a combination of two sinusoidal functions representing the cardiac cycle, with period $T_c = 1$ s, and the respiratory cycle, with period of $T_r = 4$s, respectively. With coefficients $a_c = 1.46$ mmHg/m, $a_r = 0.52$ mmHg/m, and assuming a brain width of $L = 7$ cm, we then compute the pressure difference between the pial and ventricular surface as $\mathrm{d}p = (a_c \sin(2\pi t) + a_r \sin(0.5\pi t))L$. Specifically, we set the pressure gradient (Fig. IV.1) as

$$\mathrm{d}p = \mathrm{d}p_{\text{cardiac}} + \mathrm{d}p_{\text{respiratory}} = 13.7\sin(2\pi t) + 4.9\sin(0.5\pi t) \quad \text{(Pa)}. \tag{IV.2.4}$$

IV.2.3.1 Linear elasticity

We impose a no-stress condition on the ventricular surface and a time-dependent pressure on the pial boundary of the parenchyma, resulting in the prescribed pressure difference dp. First, we investigate the effect of the cardiac cycle alone (Model A cf. Table IV.2), thus imposing the following Neumann-type boundary conditions

$$\begin{aligned} &\sigma \cdot n = 0 && \text{on the ventricular surface,} \\ &\sigma \cdot n = -13.7\sin(2\pi t)\text{Pa} && \text{on the pial surface.} \end{aligned}$$

Second, we consider the combined effect of the cardiac and respiratory cycle on the pressure difference (Model B-C cf. Table IV.2) with the following Neumann boundary conditions

$$\begin{aligned} &\sigma \cdot n = 0 && \text{on the ventricular surface,} \\ &\sigma \cdot n = -(13.7\sin(2\pi t) + 4.9\sin(0.5\pi t)) && \text{on the pial surface.} \end{aligned}$$

IV.2.3.2 Poroelasticity

In the poroelastic model, we impose pure Neumann conditions for the total stress $\sigma^* = \sigma - p\mathbb{I}$:

$$\sigma^* \cdot n = 0 \qquad \text{on the ventricular surface}$$

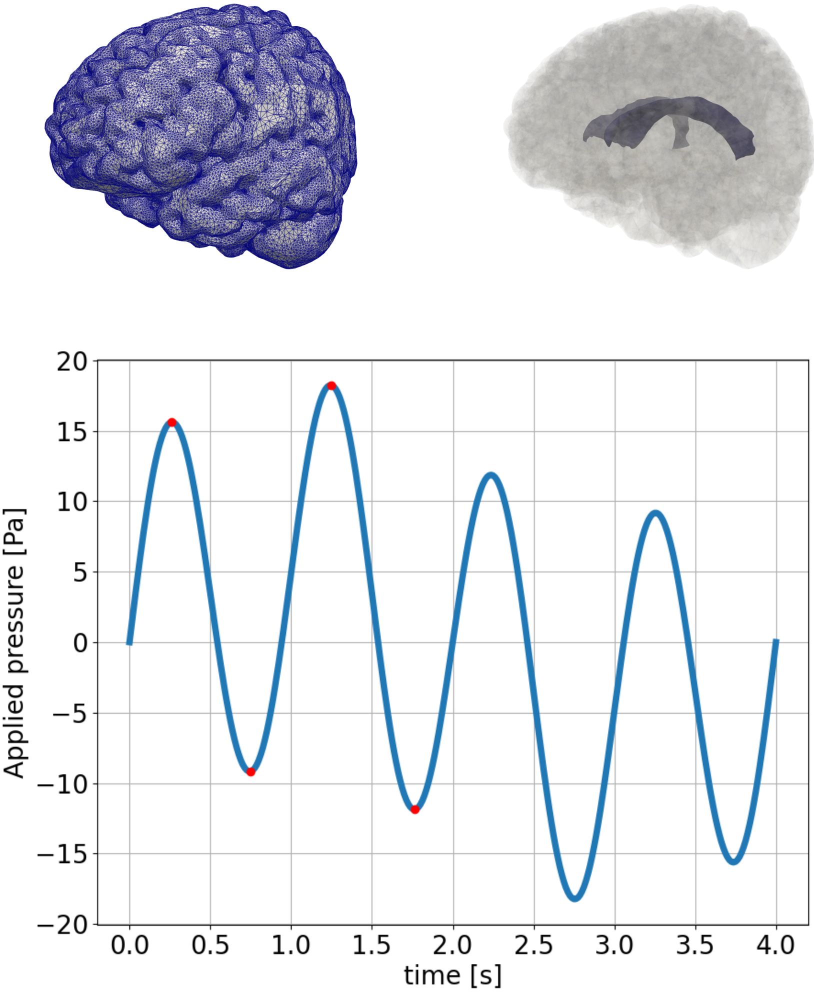

Figure IV.1: The computational mesh with edges (top left). The computational domain with highlighted ventricular surface (top right). The time-dependent applied pressure difference between the pial and ventricular surface (bottom). The red dots ($t = 0.2625, 0.75, 1.25, 1.75$) represent point of interest (peaks and valleys for $t < 2.0$).

$$\sigma^* \cdot n = -13.7 \sin(2\pi t) - 4.9 \sin(0.25\pi t) \qquad \text{on the pial surface}$$

We introduce the parameter $\beta \in [0, \infty)$ as the (membrane) permeability of the pial membrane and the additional boundary conditions

$$\begin{aligned} -K\nabla p \cdot n &= \beta p && \text{on the ventricular surface,} \\ -K\nabla p \cdot n &= \beta \left(p - (13.7 \sin(2\pi t) + 4.9 \sin(0.25\pi t))\right) && \text{on the pial surface,} \end{aligned}$$

These Robin-type boundary conditions model the pia as a partially permeable membrane with $\beta = (0, \infty)$, where for the lower bound $\beta = 0$ the pial membrane is impermeable (Neumann condition, Model D cf. Table IV.2), and for $\beta \to \infty$ the pial membrane is fully permeable (Dirichlet condition, Model E cf. Table IV.2).

IV.2.4 Material parameters and model variations

We systematically consider a set of parameters (Tab IV.1) and of models (Tab IV.2). In models A, B, and C, the brain parenchyma is modelled as an elastic medium, while for models D and E the parenchyma is modeled as a poroelastic medium permeated by a single fluid network. We also investigate the effect of different external forces via boundary conditions, and of different parameters. For model A, the pulsatile pressure difference includes the cardiac component only while for the other models the pulsatile pressure difference is the combination of the cardiac and respiratory components. Regarding the elastic properties of the brain parenchyma, we consider a rather incompressible material $\nu = 0.495$ for models A, B, D, and E, and we investigate the effect of an even more incompressible material $\nu = 0.4983$ in model C. To model flow in the tortuous ECS in the poroelastic cases (D-E), we consider a small hydraulic conductivity [Var+16] and we consider two different scenarios with a fully permeable or impermeable pial membrane.

Name	Symbol	Values	Units	Reference
Poisson ratio	ν	$0.495, 0.4983$	$[-]$	[SH07; SSM05]
Young's modulus	E	1642	Pa	[Bud+15]
Biot-Willis coefficient	α	1.0	[-]	[Guo+18]
Hydraulic conductivity	K	$1.57 \cdot 10^{-5}$	$\mathrm{mm^2Pa^{-1}s^{-1}}$	[Var+16]
Storage coefficient	s	$3.9 \cdot 10^{-4}$	$\mathrm{Pa^{-1}}$	[Guo+18]
Pial permeability	β	$0, \infty$	$\mathrm{mmPa^{-1}s^{-1}}$	

Table IV.1: Overview of material parameters used in numerical simulations, values and literature references.

Model	Constitutive equations	Forces	ν	β
A	Elastic	Cardiac	0.495	NA
B	Elastic	Cardiac and respiratory	0.495	NA
C	Elastic	Cardiac and respiratory	0.4983	NA
D	Poroelastic	Cardiac and respiratory	0.495	0
E	Poroelastic	Cardiac and respiratory	0.495	∞

Table IV.2: Overview of computational models

IV.2.5 Numerical methods

The equations were solved with the finite element with FEniCS [Aln+15]. We used P1 elements for the displacement in linear elasticity (Models A,B,C) and the lowest-order Taylor-Hood elements (P2-P1) [TH73] for displacement and pressure (Models D, E). For all models, we impose a Neumann boundary condition for the momentum equation(s) on the entire boundary. This setup implies that the solutions are determined up to rigid motions or a constant pressure only, therefore we imposed additional constraints via Lagrange multipliers [KMM15]. We used the implicit Euler scheme to discretize the equations in time. We performed convergence tests for several computational domains (see Supporting Information, Section B).

IV.2.6 Quantities of interest

For models A, B, and C, we report the displacement field u, its magnitude, and its values in selected points. The corresponding volume change is computed as:

$$\Delta V_e = \int_\Omega \operatorname{div}(u)\,\mathrm{d}x = \int_{\partial\Omega} u \cdot n\,\mathrm{d}s,$$

where we applied the divergence theorem. From the displacement field u, we compute the elastic stress tensor σ, and the von Mises stress σ_M as:

$$\sigma_M = \sqrt{\frac{3}{2} s : s},$$

where s is the deviatoric part of the stress tensor defined as $s = \sigma - \frac{1}{3}tr(\sigma)$. The von Mises stress provides information on the deviatoric stress while being a scalar value and therefore easier to visualize.

For the poroelastic models D and E, in addition to the above mentioned quantities, we analyze the fluid pressure p on the whole domain, and in selected planes and lines. The Darcy fluid velocity is computed as

$$v = -K \, \nabla \, p,$$

the fluid flux on the domain boundary is computed as

$$\Phi = \int_{\partial\Omega} v \cdot n\,\mathrm{d}s,$$

and the volume change caused by the fluid flux is

$$\Delta V_f = \int_0^T \Phi\,\mathrm{d}t,$$

where T defines the time period of interest (e.g. $T = 1$s for the cardiac cycle). To compare flow and volume changes to values in the literature, we distinguish between volume changes occurring due to expansion and flow at the pial membrane and expansion and flow at the ventricular surface.

To quantify the stroke volumes caused by elastic deformation and by the fluid flow we consider the curves ΔV_e, and ΔV_f respectively. In particular, we identify the peak and valley in the time period of interest $[0, T]$, sum their absolute values and divide by two. In the following, we describe the process to decompose the volume change curves into their cardiac and respiratory components.

IV.2.7 Separation of cardiac and respiratory components

The prescribed pulsatile pressure gradient is composed of a cardiac component ($T = 1\text{s}$) and a respiratory component ($T = 4\text{s}$). It is therefore natural to decompose the quantities of interest (described in the dedicated section) into the same components. First, consider the volume change caused by the elastic displacement. To compute the amplitude of the cardiac component of ΔV_e (t) we compute the arithmetic average of the magnitude of peaks and valleys of ΔV_e function over the $4s$ simulation for a total of 8 data points. Therefore, the cardiac component can be expressed as

$$\Delta V_{e,c}(t) = \frac{1}{8}\sum_{i=1}^{8} |\Delta V_e(\bar{t}_i)| \sin(2\pi t),$$

where $\bar{t}_i$ are the times corresponding to peaks or valleys of the function ΔV_e (t). The corresponding respiratory component can be obtained by subtraction as follows

$$\Delta V_{e,r}(t) = \Delta V_e(t) - \Delta V_{e,cardiac}(t)$$

The above operations can be repeated on the volume change curves of pial and ventricles separately.

Similarly, the fluid flux can be decomposed into its cardiac and respiratory components. However, these fluctuations are not expected to be in phase with the pressure pulsations (as is the case for displacements). In this case, we therefore first identify the amplitude of the respiratory component. To this end, we impose that the value of the respiratory component Φ_r at $t = 1\text{s}$ is the average between the peak value and the valley value in the neighbourhood of the chosen time $t = 1\text{s}$. Therefore the respiratory component can be expressed as

$$\Phi_r = \frac{(\Phi_{\text{peak}} + \Phi_{\text{valley}})}{2} \sin(0.5\pi t),$$

where Φ_{peak} and Φ_{valley} are the peak and valley values in the neighbourhood of $t = 1\text{s}$. The cardiac component can be obtained by subtraction

$$\Phi_c(t) = \Phi - \Phi_r(t).$$

The above operations can be repeated on the flux curves of pial and ventricles separately.

IV.2.8 Mesh convergence test

We performed numerical convergence tests using several meshes. All the mesh refinings were performed in the FEniCS software. From the Colin 27 mesh [Fan10] (COLIN27), we generated a finer mesh (COLIN27-GR1). From a coarsened version of the COLIN27 (COARSE) we generated two refined meshes: COARSE-GR1 and COARSE-GR2 where we applied the global refinement function in FEniCS once and twice, respectively. From the coarsened mesh COARSE, we also derived a mesh locally refined around the ventricular area (COARSE-RV), targeting the cells whose distance from the ventricles center d was $d < 30$ mm. Again, we performed a global refinement of the mesh COARSE-RV to obtain COARSE-RV-GR1. For the meshes described above, and listed with further details in IV.3, we simulated the linear elasticity equations described in IV.2.1 with P_1 finite element for the displacement u and the following pure Neumann boundary condition for the total stress such as

$$\begin{aligned} &\sigma^* \cdot n = 0 && \text{on the ventricular surface} \\ &\sigma^* \cdot n = -4.9\sin(2\pi t) - 13.7\sin(0.25\pi t) && \text{on the pial surface} \end{aligned}$$

We then compared the volume change of the pial and ventricular surfaces for the different meshes as shown in Fig IV.2. Meshes COARSE-RV-GR and COLIN27-GR1 yield very similar results: the max values differences are 1% for the pial and 1.5% for the ventricular volume change. The COARSE-RV-GR is less computationally expensive since it has 1 227 992 cells compared to 1 994 888 cells of COLIN27-GR1. The maximal difference in the quantities computed on COARSE-RV-GR and COARSE-GR2 is 12% for the change of volume at the ventricular surface, and 6.47% for the change of volume at the pial surface. In addition, COARSE-GR2 contains 5.2 times the number of cells of COARSE-RV-GR, making it computationally expensive. Therefore, we chose to perform our computations on mesh COARSE-RV-GR.

Name	number of cells	h_{min}	h_{max}
COARSE	99605	0.49	26.74
COARSE-GR1	796840	0.25	16.7386
COARSE-GR2	6374720	0.10	8.70
COARSE-RV	153499	0.25	25.1336
COARSE-RV-GR	1227992	0.10	15.6639
COLIN27	249361	0.49	13.50
COLIN27-GR1	1994888	0.20	9.18

Table IV.3: The mesh used for the mesh convergence: name, number of cells, minimum cell diameter and maximum cell diameter.

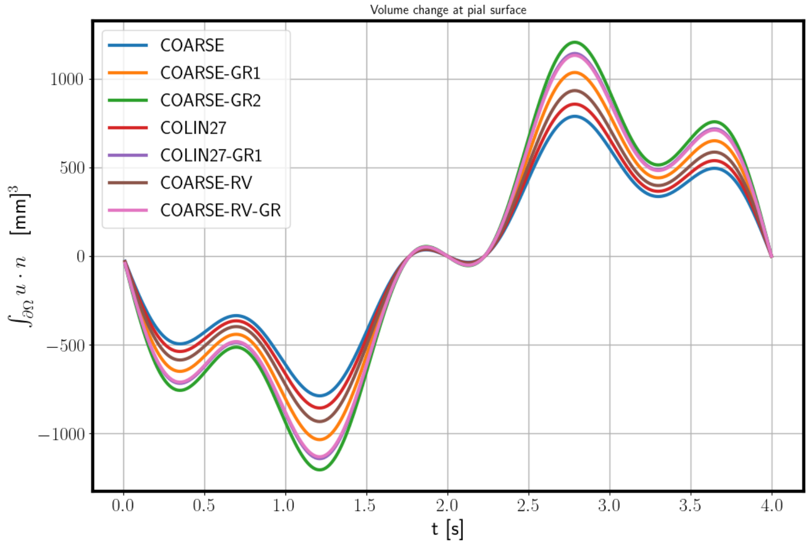

(a)

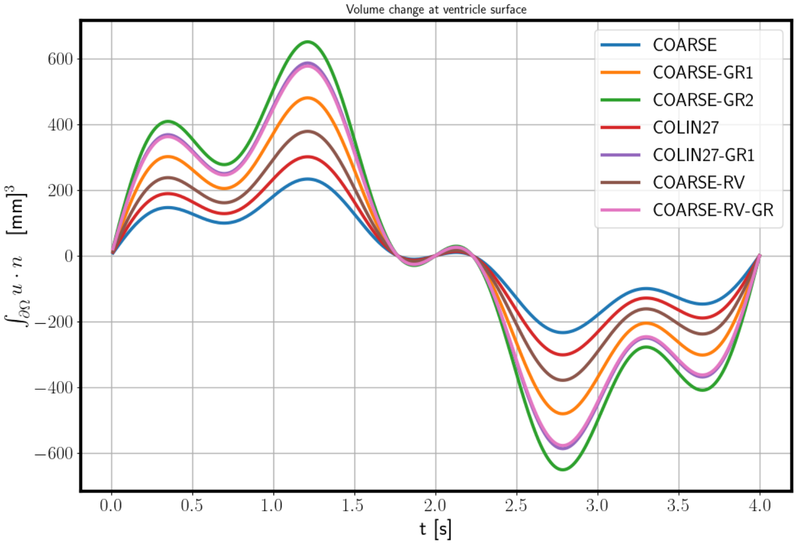

(b)

Figure IV.2: Convergence test for a linear elasticity case over the meshes in Tab. IV.3: volume change for the pial surface a and for the ventricular surface b. The COARSE-RV-GR-mesh (pink line) was used as the mesh for the numerical simulations.

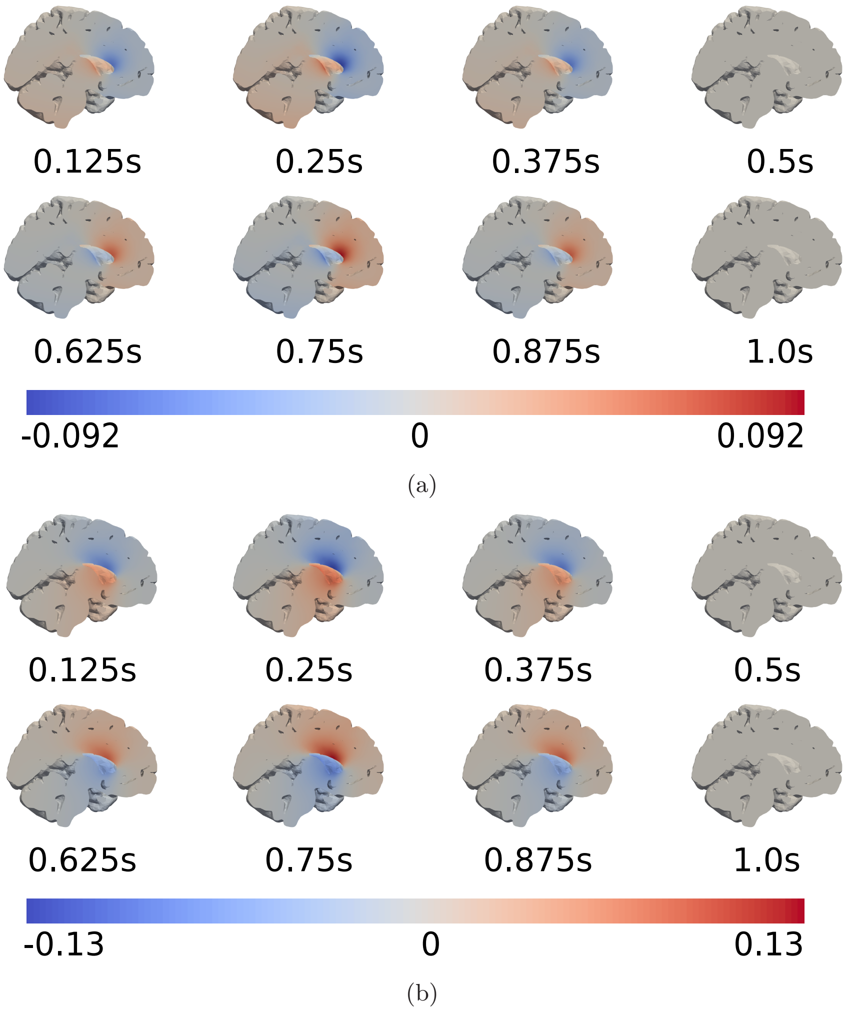

Figure IV.3: Snapshots at different times relative to the cardiac cycle of the displacement (in mm) induced by a cardiac pressure difference between the pial and ventricular boundary in the y-direction (a), and z-direction (b).

IV.3 Results

IV.3.1 Cardiac pulsatility induces pulsatile brain displacement

The applied pressure difference (Model A) induces a pulsatile displacement of the brain: the parenchyma is initially compressed, and then expands passing through no displacement at $t = 0.5$ s and $t = 1.0$ s. The peak displacement magnitude is 0.15 mm and occurs at $t = 0.25$s and $t = 0.75$s relative to the cardiac cycle (Figure IV.3). The peak x-, y-, and z-displacements occur at the same times

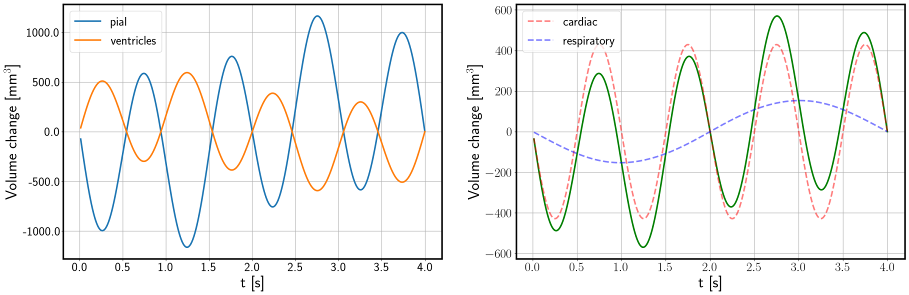

(a) Pial and ventricular volume change over time (mm^3).

(b) Change in total brain volume (mm^3) over time (green curve), cardiac component (red dashed curve), respiratory component (blue dashed curve).

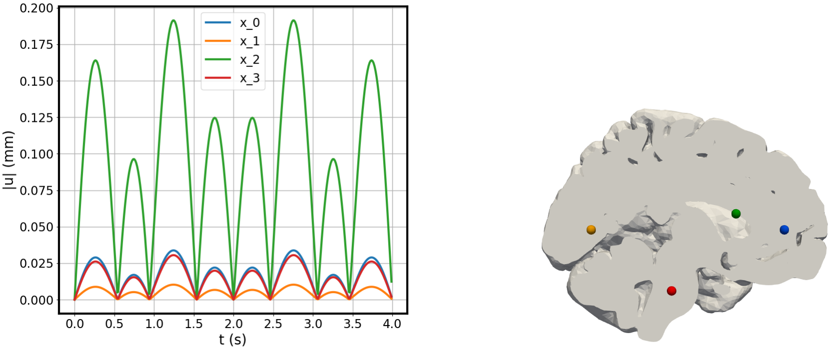

(c) Displacement magnitude $|u(x_p, t)|$ (mm) over time in four select points in the sagittal plane: $x_0 = (87, 170, 78)$ in the frontal lobe, $x_1 = (87, 50, 78)$ in the occipital lobe, $x_2 = (87, 140, 88)$ in the ventricular area near the boundary, $x_3 = (87, 100, 40)$ in the brain stem.

(d) Sagittal section of the brain parenchyma with points of interest: x_0 (blue), x_1 (orange), x_2 (green), x_3(red)

Figure IV.4: Volume changes and displacement magnitude under cardiac and respiratory pressure pulsations (Model B).

and are 0.10, 0.09 mm and 0.10mm, respectively. The negative and positive displacements are clearly separated, creating an ideal separation line that crosses the ventricle area, where the largest magnitudes are observed (Figure IV.3).

IV.3.2 Cardiac pulsatility dominates respiratory pulsatility in brain displacements

When applying a pressure difference between the pial and ventricular boundaries with both a cardiac and respiratory component (Model B), we observe an analogous behaviour as with only a cardiac contribution but now with a longer period, higher magnitudes, and more local maxima and minima. Again, negative and positive displacements are clearly separated resulting in a ideal separation line that crosses the ventricular area. Again, as the pressure increases on the pial surface (Figure IV.1) for $t < 2$ s, the brain is compressed, with a peak compression of 569.87 mm^3 at 1.25 s and a peak expansion of 569.87 mm^3 at 2.75s (Figure IV.4a-b). In particular, the volume change through the pial surface reaches the maximum of 1163.86 mm^3 at $2,75$s, while the volume change through the ventricular surface reaches the maximum of 594 mm^3 at 1.25 s. The volume change curves through the parenchyma and through the ventricles (Fig IV.4a) are shifted by π in phase.

The cardiac component dominates the respiratory component, both in the applied gradient and, as expected, in the induced displacement and volume change (Figure IV.4b-c). The peak volume change due to the cardiac component of the applied pressure gradient is 429 mm ^{3}, while the peak volume change due to the respiratory component of the applied pressure gradient is 153 mm^3 (Fig IV.4b). We observe the greatest displacement in the ventricular area (Figure IV.4c). The peak displacement magnitude max $\|u\|$ is 0.196 mm and occurs at $t = 1.25$ s and $t = 2.75$ s above the lateral ventricles near the boundary.

IV.3.3 Brain displacements persist under reduced compressibility

For a more incompressible parenchyma (Model C), we observe the same brain displacement patterns with less than 1.0 % change in displacement magnitude: the peak displacement magnitude for this case is 0.185 mm (compared to 0.196 mm in Model B) (data not shown).

IV.3.4 ISF pressure is nearly uniform with impermeable pial membrane

For the poroelastic case, we also observe an initial compression followed by an expansion of the parenchyma. Comparing with the elastic displacements at $t = 1.25$ s and $t = 2.75$ s, the peak displacement magnitude is 0.22, and occurs in close proximity of the ventricles (Figure IV.5a). The peak displacement predicted by the poroelastic model is 0.22 mm, which is higher than in the elastic model with the same driving forces. The overall pattern of displacement, including the relative importance of the cardiac versus respiratory component, is similar to displacements observed with the linear elasticity model.

During the 4s respiratory cycle, the fluid pressure p is nearly uniform in space with minimum and maximum values of -3.9 Pa and 3.5 Pa,

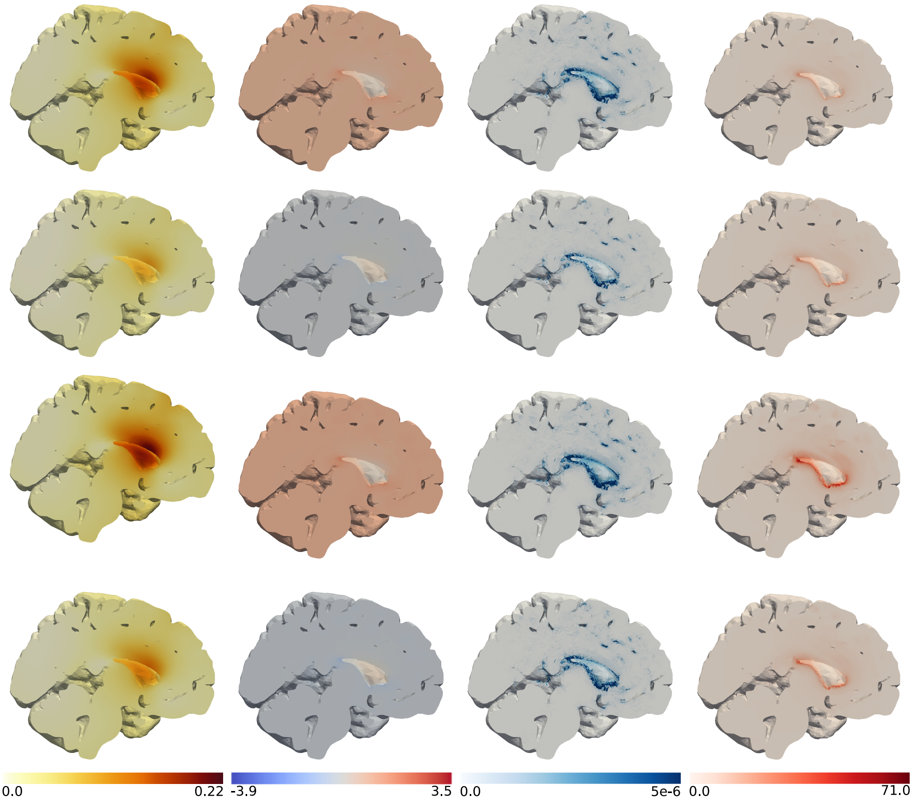

(a) (b) (c) (d)

Figure IV.5: Column (a) displacement magnitude (mm), (b) fluid pressure (Pa), (c) fluid velocity ($-K\,\nabla p$) magnitude (mm/s), and (d) von Mises stress (Pa) at different time points: $t = 0.2625$ s, 0.75s, 1.25s, 1.75s (from top to bottom).

respectively (Figure IV.5b). Again, the extreme values occur in the vicinity of the ventricles. The peak fluid pressure difference is thus lower than the prescribed stress. As the pressure is nearly uniform, the pressure gradient is small almost everywhere in the domain with average pressure gradient magnitude of less than $9.0 \cdot 10^{-3}$ Pa/mm. In localized regions, high pressure gradients are observed (of up to 16 Pa/mm).

With the pressure gradients reported above, the peak velocity magnitude is 0.26 μm/s and occurs at t = 2.725. The highest velocities occur near the ventricles where the extracellular fluid flows in the same direction as the movement of the ventricular surface induced by the applied pressure difference. In regions further away from the ventricles, fluid velocities are negligible and on the order of a few nm/s.

The solid part of the stress is visualized via the von Mises stress σ_M (Figure IV.5d). The von Mises stress is nearly zero (< 5Pa) everywhere in

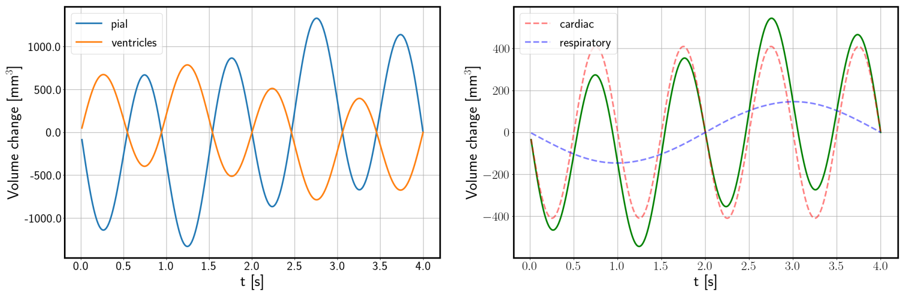

(a) (b)

Figure IV.6: Poroelastic model with impermeable pial membrane driven by cardiac and respiratory pulsatility: (a) volume change on pial (blue) and ventricular (orange) surfaces, (b) total volume change (green curve) and its cardiac component (red dashed curve) and respiratory component (blue dashed curve)

the parenchyma, except for in the ventricular area where it reaches its maximum of 134 Pa at 1.25 s. The peak value is only observed in a very limited set of nodes (less than 0.06% of total nodes) in the proximity of the ventricles. In Figure IV.6 we show the volume change computed at each time step on the pial and on the ventricular surfaces. The volume change for the ventricular and the pial surface are opposite in sign. The maximum volume change magnitudes are reached at 1.2125s and 2.775s and are 764 mm^3 for the ventricles and 1293 mm^3 for the pial surface. The total volume change (Fig. IV.6(b)) reaches its maximum of 529 mm^3 at 2.775s. From the decomposed signal, we find a cardiac induced stroke volume of 409.86 mm^3, and a respiratory induced stroke volume of 146.37 mm^3.

IV.3.5 Pial membrane permeability induces sharp ISF pressure boundary layer

With permeable pial and ventricular membranes ($\beta = \infty$, model E) the peak displacement magnitude is 0.22 mm at $t = 2.75$s in the ventricular area (data not shown). The characteristics of the displacement field do not change significantly from previous models. The volume change caused by the displacement field is also comparable to what observed with model D (data not shown).

For the pressure p (Fig. IV.7 top) we observe a mostly uniform field but a sharp boundary layer for the pial boundary. The applied pressure gradient and small hydraulic conductivity K do not allow for the pulsation to be transmitted inside the parenchymal tissue. We observe the same sharp boundary layer also for the fluid velocity magnitude (Fig. IV.7). Fig. IV.8 shows the fluid flux through the ventricular and pial surfaces. We observe that the majority of the flux happens through the pial surface, where it reaches the maximum value of

62.89mm^3/s, compared to only 0.11 mm^3/s for the ventricular surface.

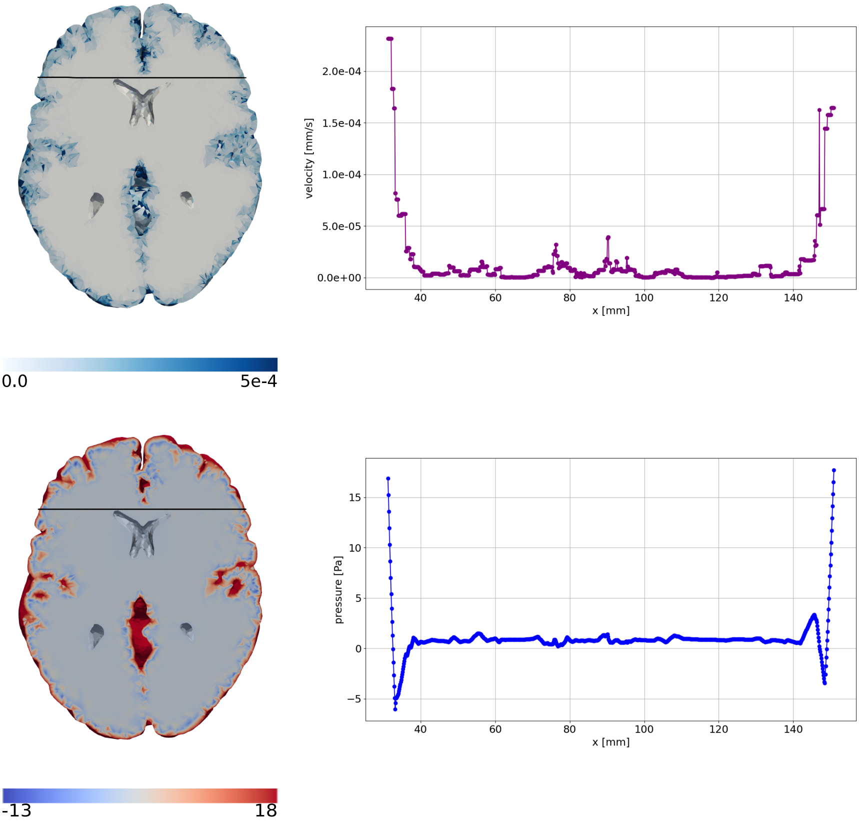

Figure IV.7: Poroelastic model with fully permeable pial membrane driven by cardiac and respiratory pulsatility: fluid velocity (top left) and fluid pressure (bottom left) in horizontal section. Fluid velocity magnitude (mm/s) over the black line on the horizontal section(top right), pressure (Pa) over the black line on the horizontal section(bottom right).

From the decomposed signal (Figure IV.8), we find an average cardiac peak volumetric flux of 54.79 mm^3/s for the pial and 0.09 mm^3/s for the ventricular surface. The corresponding peak respiratory fluxes are lower, 9.95 mm^3/s for the pial and 0.028 mm^3/s for the ventricular surface. Integrating the individual curves (Figure IV.8) gives a cardiac-induced volume change of 8.19 mm^3 for the pial and 0.015 mm^3 for the ventricular surface. The corresponding respiratory-induced volume changes are 6.335 mm^3 for the pial and 0.01 mm^3 for the ventricular surface.

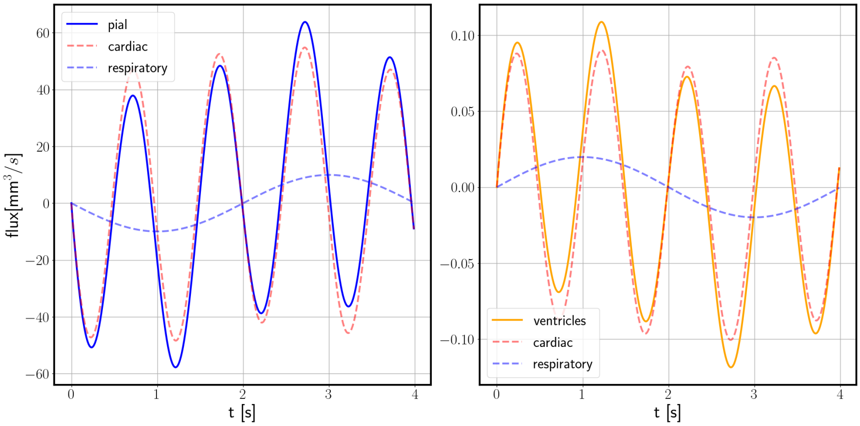

Figure IV.8: Poroelastic model with fully permeable pial membrane driven by cardiac and respiratory pulsatility: fluid flux on pial (blue solid curve) and ventricular (orange solid curve) surfaces. Red and blue dashed curves show the cardiac and respiratory components.

IV.4 Discussion

Summary of results The importance of cardiac versus respiratory pulsations on brain displacements are not yet fully understood. In this study, we have shown that in vivo measurements of pressure differences within the cranium [Eid08] induce pulsatile brain displacements with both cardiac and respiratory components. Even the more basic linear elastic model provides useful insights regarding the displacement of parenchyma. In fact, the difference between the displacement fields obtained with the linear elastic model (B) and the poroelastic models (D and E) are negligible. Furthermore, the cardiac pulsation alone is responsible for the largest part of the displacements occurring in the brain parenchyma. For the poroelastic models, the impermeable boundary condition (model D) results in a mostly uniform pressure field, and therefore almost zero, and mostly concentrated in the ventricular area, fluid velocity. The fully permeable boundary condition (model E), results in a sharp boundary layer both for the pressure and on the velocity field. The pulsation is not transmitted through the fluid in the parenchymal tissue but it remains on the domain boundary. This behaviour suggests that, with the given, physiological, material parameters, a systemic pressure gradient alone is not sufficient to drive fluid movement through the brain.

Comparison with literature The maximal displacement magnitude (with models D and E) is 0.22 mm, in excellent agreement with values for peak displacement reported by Pahlavian et al. and Sloots et al. [Pah+18; SBZ20]. Assuming that these displacements occur over a segment of approximately 6 cm, the maximal volumetric strain is 3.3×10^{-3}, which is exactly what was measured by Sloots et al.[SBZ20]. Pahlavian et al. [Pah+18] pointed to medial and inferior brain regions as regions with large motion, while our model predicts peak displacements in regions in close proximity to the ventricles (Figure IV.3). In addition, the experimental values reported in [Pah+18; SBZ20] only took into account motion induced by cardiac pulsations, while the respiratory influence was overlooked. In our model, the applied pressure pulsation induced by the cardiac cycle is 2-3 times larger than the respiratory pulsation, and a similar relationship is obtained for the displacements induced by the two cycles. The peak displacement induced solely by the cardiac pulsation reached 0.15 mm, comparable to values in [Pah+18]. It is worth noting that this linear relationship between pressure and movement will not necessarily hold for CSF flow in the SAS [Vin+19]. A higher value for the von Mises stresses near the ventricles in our simulations suggests that this region is most prone to shape distortion caused by the cardiac and respiratory cycles. As reported in preliminary work by Sincomb and colleagues [Sin+20; Sin+21], due to the viscoelastic nature of the brain, even a small transmantle pressure gradient can over time contribute to the enlargement of the ventricles. The viscoelastic nature of the brain may explain why some authors have assumed the brain to be relatively compressible when modeling long-term behaviour (e.g. hydrocephalus) [TV09; TV11; Var+16].

As brain and CSF movement is coupled, changes in brain volume, as computed by our models, will result in CSF flow in the SAS. It is reasonable to assume that flow and displacements on the ventricular surface is directly related to aqueductal flow, while flow and displacements on the pial surface may be related to flow in the foramen magnum. The total volume change peaks (models B, D, and E) and the respective stroke volumes associated with the cardiac component are comparable. We found a cardiac induced stroke volume of 429μL (model B), and 529μL (model D) compared to approximately 500μL at C2-C3 in [Bal14a] (Table 11.1 for healthy subjects). On the other hand, the volume change through the ventricles estimated from model B is 593μL, and is approximately one order of magnitude larger than the ventricular stroke volumes reported for healthy subjects 48μL [Bal14a] Table 11.1). Furthermore, the aqueductal stroke volume computed with all models (linear elasticity and poroelasticity) is closer to the reported values for idiopathic normal pressure hydrocephalus patients [Bal14a] Table 11.1). An observed delay in the reversal of flow in the cerebral aqueduct compared to the foramen magnum [Bal14b] was not predicted by volumetric changes in our model.

ISF flow within the human brain has not been measured experimentally, but several estimates have been made. From experimental data of tracer distribution and clearance in rats, Cserr and colleagues estimated a bulk flow velocity of around 0.1–0.25 μm/s [CCM77; Cse+81]. A directional bulk flow of this magnitude in addition to diffusion may explain tracer movement in humans [CVR19]. On the brain surface of mice, pulsatile CSF flow of magnitudes of around 20 μm/s have been observed on top of a static flow of similar magnitude [Bed+18; Mes+18]. Flow of ISF in our model occurred mainly close to the pial surface and a peak velocity of 0.5μm/s (model E) were observed. Fluid flow within the parenchyma was dominated by cardiac pulsations, contributing a factor 3 more than respiration to fluid flow velocities. The fluid exchange between ISF and CSF (stroke volume induced by fluid flow) for the pial was computed to be 8.19μL over the cardiac and 6.34μL over the respiratory cycle. The fluid exchange over the ventricles is negligible: 0.015μL for the cardiac component, and 0.013μL for the respiratory component. The amount of CSF/ISF-exchange was thus equally dominated by cardiac and respiratory pulsations as the respiratory pulsation spans over a longer time. Several other studies have pointed to respiration to be the main driver of displacement of fluid in the SAS [Dre+15; Dre+17; Vin+19]. However, relationships between fluid pressure and flow will differ between CSF and ISF, and it is not given that the pulsations within the parenchyma found in our model translates directly to the CSF in the SAS.

Limitations We considered homogeneous properties for the parenchyma tissue without distinguishing between gray and white matter and we modelled the parenchyma tissue as isotropic. Nevertheless, the estimated values for white and gray matter Young modulus are similar[Bud+15], and the average value can be used as a good approximation without affecting the results significantly. Moreover, Budday and colleagues [Bud+19] demonstrated that the brain tissue can be considered as an isotropic material from a mechanical point of view despite being anisotropic.

In this work, we considered a limited set of parameter values based on the literature currently available. The main goal of this paper was not to perform a parametric study but rather study the effect of a pulsatile pressure gradient on the brain parenchyma. Certainly, a parametric study, taking into account further parameter combinations, could be performed in later work.

The brain tissue is permeated by several fluid networks: ISF, capillary blood, venous blood and arterial blood[Mat+16]. In this work, we considered a one–network poroelastic model and we did not consider the exchange between the ISF and the other compartments. The interaction between ISF and other fluid compartments could be modelled with a multiple–network poroelastic model [TV11; Var+16] and it could be investigated in future work.

The CSF fluid dynamics in the ventricles and in subarachnoid space was not included in our models. In particular, the resistance to flow through the aqueduct, SAS or spinal canal is not explicitly modeled The resistance is probably much higher in aqueduct, which may explain why our models overestimate aqueductal flow (volume change through the ventricular surface), but not flow to the spinal flow (volume change through the pial surface).

Finally, we note that the pressure data was obtained from iNPH patients [Vin+19], which may serve as another source of error, particularly for aqueductal stroke volume [Bal14a]. However, to our knowledge, no such intracranial in-vivo pressure measurements exist from healthy volunteers.

Conclusion We have presented elastic and poroelastic models of the brain with pulsatile motion driven by pressure pulsations originating from the cardiac and respiratory cycle. The displacement fields and total volume change match well with values found in the literature, while the pressure applied on the boundary did not properly propagate through brain tissue, suggesting that pressure pulsations from blood vessels act not only on the surface but also within brain tissue. Further investigation of pressure pulse propagation within the brain parenchyma is needed to fully understand the mechanisms leading and connected to brain parenchyma pulsation and brain clearance.

References

[Aln+15] Alnæs, M. et al. “The FEniCS project version 1.5”. In: *Archive of Numerical Software* vol. 3, no. 100 (2015).

[Bal14a] Balédent, O. “Imaging of the Cerebrospinal Fluid Circulation”. In: *Adult Hydrocephalus*. Ed. by Rigamonti, D. Cambridge: Cambridge University Press, 2014, pp. 121–138.

[Bal14b] Balédent, O. “Imaging of the cerebrospinal fluid circulation”. In: *Adult hydrocephalus* vol. 256, no. 128to512 (2014), p. 121.

[Bed+18] Bedussi, B. et al. “Paravascular spaces at the brain surface: Low resistance pathways for cerebrospinal fluid flow”. In: *Journal of Cerebral Blood Flow & Metabolism* vol. 38, no. 4 (2018), pp. 719–726.

[BS07] Brenner, S. and Scott, R. *The mathematical theory of finite element methods*. Vol. 15. Springer Science & Business Media, 2007.

[Bud+15] Budday, S. et al. “Mechanical properties of gray and white matter brain tissue by indentation”. In: *Journal of the mechanical behavior of biomedical materials* vol. 46 (2015), pp. 318–330.

[Bud+19] Budday, S. et al. “Fifty shades of brain: a review on the mechanical testing and modeling of brain tissue”. In: *Archives of Computational Methods in Engineering* (2019), pp. 1–44.

[CCM77] Cserr, H. F., Cooper, D., and Milhorat, T. “Flow of cerebral interstitial fluid as indicated by the removal of extracellular markers from rat caudate nucleus”. In: *Experimental eye research* vol. 25 (1977), pp. 461–473.

[Cse+81] Cserr, H. et al. “Efflux of radiolabeled polyethylene glycols and albumin from rat brain”. In: *American Journal of Physiology-Renal Physiology* vol. 240, no. 4 (1981), F319–F328.

[CVR19] Croci, M., Vinje, V., and Rognes, M. E. “Uncertainty quantification of parenchymal tracer distribution using random diffusion and convective velocity fields”. In: *Fluids and Barriers of the CNS* vol. 16, no. 1 (2019), pp. 1–21.

[Dre+15] Dreha-Kulaczewski, S. et al. “Inspiration is the major regulator of human CSF flow”. In: *Journal of Neuroscience* vol. 35, no. 6 (2015), pp. 2485–2491.

[Dre+17] Dreha-Kulaczewski, S. et al. “Identification of the upward movement of human CSF in vivo and its relation to the brain venous system”. In: *Journal of Neuroscience* vol. 37, no. 9 (2017), pp. 2395–2402.

[Eid08] Eide, P. K. “Demonstration of uneven distribution of intracranial pulsatility in hydrocephalus patients”. In: *Journal of neurosurgery* vol. 109 (2008), pp. 912–917.

[ES10a] Eide, P. K. and Sæhle, T. “Is ventriculomegaly in idiopathic normal pressure hydrocephalus associated with a transmantle gradient in pulsatile intracranial pressure?” In: *Acta neurochirurgica* vol. 152, no. 6 (2010), pp. 989–995.

[ES10b] Eide, P. K. and Sorteberg, W. “Diagnostic Intracranial Pressure Monitoring and Surgical Management in Idiopathic Normal Pressure Hydrocephalus: A 6-Year Review of 214 Patients”. In: *Neurosurgery* vol. 66, no. 1 (2010), pp. 80–91.

[Fan10] Fang, Q. “Mesh-based Monte Carlo method using fast ray-tracing in Plücker coordinates”. In: *Biomedical optics express* vol. 1, no. 1 (2010), pp. 165–175.

[Guo+18] Guo, L. et al. “Subject-specific multi-poroelastic model for exploring the risk factors associated with the early stages of Alzheimer’s disease”. In: *Interface focus* vol. 8, no. 1 (2018), p. 20170019.

[Ili+13] Iliff, J. J. et al. “Cerebral arterial pulsation drives paravascular CSF–interstitial fluid exchange in the murine brain”. In: *Journal of Neuroscience* vol. 33, no. 46 (2013), pp. 18190–18199.

[Jes+15] Jessen, N. A. et al. “The glymphatic system: a beginner’s guide”. In: *Neurochemical research* vol. 40, no. 12 (2015), pp. 2583–2599.

[KMM15] Kuchta, M., Mardal, K.-A., and Mortensen, M. “Characterisation of the space of rigid motions in arbitrary domains”. In: *Proc. of 8th National Conference on Computational Mechanics. Barcelona, Spain: CIMNE.* 2015.

[Mat+16] Matsumae, M. et al. “Research into the physiology of cerebrospinal fluid reaches a new horizon: intimate exchange between cerebrospinal fluid and interstitial fluid may contribute to maintenance of homeostasis in the central nervous system”. In: *Neurologia medico-chirurgica* vol. 56, no. 7 (2016), pp. 416–441.

[Mes+18] Mestre, H. et al. “Flow of cerebrospinal fluid is driven by arterial pulsations and is reduced in hypertension”. In: *Nature communications* vol. 9, no. 1 (2018), pp. 1–9.

[Pah+18] Pahlavian, S. H. et al. “Regional quantification of brain tissue strain using displacement-encoding with stimulated echoes magnetic resonance imaging”. In: *Journal of Biomechanical Engineering* vol. 140, no. 8 (2018).

[Raj+21] Rajna, Z. et al. “Cardiovascular brain impulses in Alzheimer’s disease”. In: *Brain* vol. 144, no. 7 (2021), pp. 2214–2226.

[SBZ20] Sloots, J. J., Biessels, G. J., and Zwanenburg, J. J. “Cardiac and respiration-induced brain deformations in humans quantified with high-field MRI”. In: *Neuroimage* vol. 210 (2020), p. 116581.

[SCC11] Sakka, L., Coll, G., and Chazal, J. “Anatomy and physiology of cerebrospinal fluid”. In: *European annals of otorhinolaryngology, head and neck diseases* vol. 128, no. 6 (2011), pp. 309–316.

[SH07] Smith, J. H. and Humphrey, J. A. “Interstitial transport and transvascular fluid exchange during infusion into brain and tumor tissue”. In: *Microvascular research* vol. 73, no. 1 (2007), pp. 58–73.

[Sin+20] Sincomb, S. et al. “Strain accumulation visco-elastic ventriculomegaly hypothesis for the onset of idiopathic normal pressure hydrocephalus (iNPH)”. In: *Biophysical Journal* vol. 118, no. 3 (2020), 452a.

[Sin+21] Sincomb, S. et al. “Transmantle pressure computed from mr imaging measurements of aqueduct flow and dimensions”. In: *American Journal of Neuroradiology* vol. 42, no. 10 (2021), pp. 1815–1821.

[SSM05] Smillie, A., Sobey, I., and Molnar, Z. “A hydroelastic model of hydrocephalus”. In: *Journal of Fluid Mechanics* vol. 539 (2005), pp. 417–443.

[STW02] Stephensen, H., Tisell, M., and Wikkelsö, C. “There is no transmantle pressure gradient in communicating or noncommunicating hydrocephalus”. In: *Neurosurgery* vol. 50, no. 4 (2002), pp. 763–773.

[TH73] Taylor, C. and Hood, P. “A numerical solution of the Navier-Stokes equations using the finite element technique”. In: *Computers & Fluids* vol. 1, no. 1 (1973), pp. 73–100.

[TV09] Tully, B. and Ventikos, Y. “Coupling poroelasticity and CFD for cerebrospinal fluid hydrodynamics”. In: *Biomedical Engineering, IEEE Transactions on* vol. 56, no. 6 (2009), pp. 1644–1651.

[TV11] Tully, B. and Ventikos, Y. “Cerebral water transport using multiple-network poroelastic theory: application to normal pressure hydrocephalus”. In: *Journal of Fluid Mechanics* vol. 667 (2011), pp. 188–215.

[Var+16] Vardakis, J. C. et al. “Investigating cerebral oedema using poroelasticity”. In: *Medical engineering & physics* (2016).

[Vin+19] Vinje, V. et al. “Respiratory influence on cerebrospinal fluid flow–a computational study based on long-term intracranial pressure measurements”. In: *Scientific reports* vol. 9, no. 1 (2019), pp. 1–13.

[WEM11] Wagshul, M. E., Eide, P. K., and Madsen, J. R. “The pulsating brain: a review of experimental and clinical studies of intracranial pulsatility”. In: *Fluids and Barriers of the CNS* vol. 8, no. 1 (2011), p. 5.

[Wil16] Wilson, M. H. “Monro-Kellie 2.0: The dynamic vascular and venous pathophysiological components of intracranial pressure”. In: *Journal of Cerebral Blood Flow & Metabolism* vol. 36, no. 8 (2016), pp. 1338–1350.